University of Southampton

DISPERSION OF MATERIAL BY WIND AND TIDE IN SHALLOW SEAS

By

William Alexander Michael NIMMO SMITH

DOCTOR OF PHILOSOPHY
SCHOOL OF OCEAN AND EARTH SCIENCE
FACULTY OF SCIENCE
SEPTEMBER 2000

UNIVERSITY OF SOUTHAMPTON

ABSTRACT

FACULTY OF SCIENCE

SCHOOL OF OCEAN AND EARTH SCIENCE

Doctor of Philosophy

DISPERSION OF MATERIAL BY WIND AND TIDE IN SHALLOW SEAS

by William Alexander Michael NIMMO SMITH

Mixing processes in shallow seas are of particular importance in the dispersion of pollution (e.g. oil slicks) as well as in the distribution of sediment and biological material (e.g. phytoplankton and fish larvae). This study aims to further investigate the processes of wind-driven Langmuir circulation and bottom-generated turbulence and to quantify the effects they have on the dispersion of buoyant material.

A numerical and analytical study is made of the dispersion of a plume of floating particles under the combined action of Langmuir circulation and a mean current. The numerical simulations show the general patterns the plume will form, with initial meanders leading to the formation of distinct windrows. The analytical model shows that the lateral diffusivity, the rate of across-current dispersion of the particles, is greatest when the angle between the direction of the wind and current is between 30^o and 120^o, and when the wind speed is large in comparison to the current speed. Further, it is found that the effects of Langmuir circulation will dominate the dispersion process when the wind speed is greater than about 10 times the current speed.

Acoustic and visual observations of the surface effects of bottom-generated turbulence in a tidally-influenced and well-mixed region of the North Sea are presented. Although the sea bed in the area is flat, it is found that at any one time 20-30% of the water surface is affected by boils – circular regions of local upwelling – of diameter 0.9 ± 0.2 times the water depth. The signature of individual boils persists for at least 7 minutes and, in accordance with laboratory and numerical studies, shows the appearance of eddies. Again, analytical and numerical models are constructed to estimate the effects of the boils on the dispersion of floating particles. The numerical simulations provide good qualitative agreement with the patterns observed in visual images of the dispersion of oil. Further, the horizontal diffusivities calculated by both them and the analytical methods show that the presence of boils can account for the dispersion measured by experimental methods in shallow tidal seas.

In summarising and discussing the main findings of this work, particular emphasis is placed on the need for further observations of these two processes, in particular the boils and eddies and their interaction with the Langmuir circulation, to further improve the estimates of dispersion.

Contents

List of Figures

Acknowledgements

I am indebted to my supervisor, Prof S.A. Thorpe for his guidance, advice and support throughout the duration of this work. Dr A. Graham provided invaluable assistance and guidance both in the analysis of the sonar data and in the development of many ideas. I am grateful to Dr K. Richards for being the third member of my thesis panel.

I am very grateful to Prof. I. Robinson and Dr. R. Lewis, AstraZeneca, UK, for their careful review of this work and their helpful, constructive comments on it.

Funding for this studentship was supplied by the Natural Environment Research Council. Mr A. Hall, George Deacon Division, Southampton Oceanography Centre, provided assistance with the sonar data, which was collected during an EC MAST funded project. The CASI images were kindly supplied by the Environment Agency, UK, and were interpreted with the assistance of Dr V. Byfield, University of Southampton. I am grateful to Dr T. Lunnel of AEA Technology, UK, for providing the aerial video of the surface plume and the environmental data for the CASI images. Discussions with Dr G. Lane-Serf and Dr J. Sharples assisted greatly in the progress of some of this work.

As ever, this work would not have been possible without the continued support of my parents, sister and friends.

Chapter 1

Overview

1.1 Introduction

In recent years there have been many accidental releases of oil into the marine environment. Among these, the oil spilt during the wrecking of the tankers *Braer* (January 1993, 25.0 million gallons of oil), *Sea Empress* (February 1996, 21.3 million gallons of oil) and *Exxon Valdez* (March 1989, 11.0 million gallons of oil) received particularly intense media coverage and generated public concern. All of these spills were in shallow waters, in close proximity to land, and so their effects were more immediately obvious and of greater concern because of their impact on the economy and wildlife of the coastal areas. In comparison, other releases such as from the tankers *Thanassis A.* (October 1994, 10.9 million gallons of oil) and *ABT Summer* (May 1991, 15.1 million gallons of oil) received much less attention because they occurred in the deep ocean, away from major concentrations of sea life and human population.

While oil spills are by no means the only form of pollution in shallow coastal seas, they serve as a useful focus for this present study because of their obvious impacts and public attention. Also any knowledge gained in the dispersion of oil will be of direct relevance to the dispersion of other buoyant material, and an increase in the understanding of the processes which control this dispersion will be of assistance over

many fields, air-sea gas exchange and sediment transport among others.

This study will focus on dispersion at small time scales (of order 1 hr) and over short length scales (of order $10 - 100$ m). It is these scales which determine the local concentration of material, which may in fact be of greater importance, for example in the combating of the spill by mechanical and chemical processes and in the toxic impact it may have on wildlife, than the large scale advection of these smaller scale patterns. Also, it is these small scales which are most difficult to include in present large scale models for the prediction of the dispersion of an accidental release, and so obtaining a reliable parameterisation of them is of particular importance.

1.2 Objectives

The aim of this work is to investigate further small-scale, near-surface processes in shallow seas and to quantify the effects they have on dispersion of floating material so as to provide a basis for improved prediction. In particular, it focuses on processes which can be seen not only to disperse buoyant material but also to accumulate it into coherent patterns at the surface. These are wind-driven Langmuir circulation, which leads to the formation of windrows, and turbulent structures generated by a current flow over the sea bed. Models will be constructed to parameterise the dispersion produced by these two processes, allowing comparisons to be made with experimental measurements of dispersion in the environment. The relative importance of each of the processes will be estimated.

1.3 Outline

Chapter 2 gives an introduction to the literature available on coherent circulation patterns generated by the wind and tidal flow over the sea bed and also to previous measurements of dispersion both in the laboratory and in the sea. Chapter 3 presents a numerical and analytical study of the dispersion of floating material from a fixed

source by a combination of Langmuir circulation and a mean current. An estimate of the relative importance of the Langmuir circulation and the tidal flow in the dispersion is also made. Novel observations of structures at the sea surface, "boils" and eddies, generated by tidal flow over a flat sea bed and with length scales equivalent to the water depth, are presented in Chapter 4. Chapter 5 describes simple models which give estimates of the dispersion of floating material by the tidally generated boils. Chapter 6 summarises the conclusions of this study and discusses possible avenues for further work.

Chapter 2

Review of mixing processes and dispersion

2.1 Langmuir circulation

The pattern of near-surface circulation now called Langmuir circulation is named after the distinguished American physicist. It was he, Langmuir, who first studied the causes of the parallel bands, or windrows (for example see Figure 2.1), of floating *Sargassum* weed he had observed during an Atlantic crossing from New York to England in 1927. The larger bands, containing 'vast' quantities of weed, with typical spacings of between $100 - 200\ m$, were closely aligned to the wind direction, with smaller, less distinct bands in-between. The bands realigned within 20 *min* of an abrupt, 90^o shift in the wind direction.

Langmuir hypothesised that it was not cohesion between the masses of weed that held them together in the bands but rather transverse converging surface currents. In the years after his return to the United States, Langmuir carried out a series of experiments on an inland lake to test his hypothesis using a wide variety of ingenious tracers, from autumnal leaves and olive oil to fluorescein dye and specially constructed drifters, to follow the near-surface currents. He found that on reaching the bands, the

Figure 2.1: Photograph of windrows in Southampton Water. The wind is directly into the camera at about 7.5 $m\ s^{-1}$. The mean windrow spacing is about 5 m. The flotsam collecting in the windrows consists of biological material produced by a phytoplankton bloom which occur in this region during periods of consistently weak tidal currents. Stable, long lasting windrows can be seen in the far right of the image (arrow). These are situated in deep water ($> 10\ m$) while the less stable windrows seen in the foreground are situated in shallow water ($< 5\ m$) where they have been carried by the tidal current.

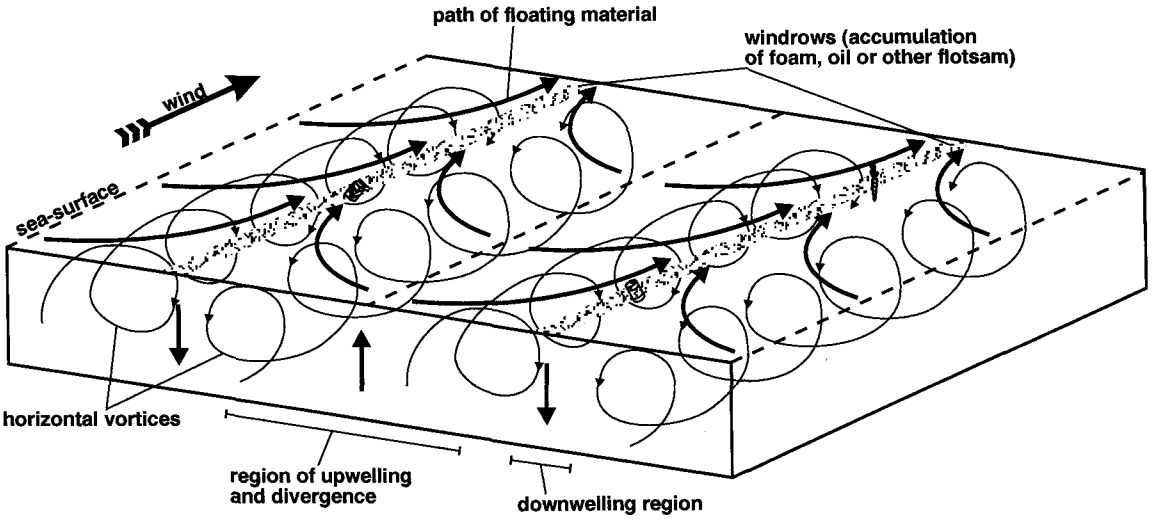

Figure 2.2: Schematic diagram of Langmuir circulation and its effect on floating material [from Nimmo Smith and Thorpe, 1999].

converging water within the currents descends. Between the bands, rising currents, on reaching the surface, flow out laterally towards the bands. The action of the wind on the water sets up longitudinal surface currents in the direction of the wind which are greatest along the lines of convergence. Thus, the net result is an array of subsurface linear vortices of alternating signs with axes directed close to the wind. Floating material, foam, oil or other flotsam, is swept towards these lines of convergence, and, unable to sink and follow the water motion, becomes trapped leading to the formation of windrows. A schematic diagram of these component vortices and their effect on floating material is shown in Figure 2.2.

Subsequent observations of Langmuir circulation have been made and reported on numerous occasions and these have been comprehensively reviewed by Pollard [1977] and Leibovich [1983]. Of particular importance to the study of Langmuir circulation has been the development of novel acoustic methods. Upward-looking sidescan sonars have been used to detect the movement and distribution of near-surface tracers, principally clouds of bubbles produced by wind-waves as they break [for example Thorpe and Hall, 1983, Zedel and Farmer, 1991], while Acoustic-Doppler instruments have

provided direct measurements of the current field [for example Pleuddemann et al., 1996, Smith, 1992]. By whatever method of study, the most commonly reported observations are wind speed, the depth of the water column or of the thermocline and the measures of the Langmuir circulation: the spacing, orientation, formation times and persistence of the surface windrows, and the surface and subsurface current structure.

The spacing between adjacent windrows, L, generally increases with increasing wind speed [for example Faller and Woodcock, 1964, Graham and Hall, 1997, Thorpe et al., 1994, Zedel and Farmer, 1991]. In the open ocean, Faller and Woodcock [1964] found that there was a significant correlation between the mean crosswind separation of the windrows and the wind speed, W, taking it to be $L = (4.8\ s) \times W$, while Graham and Hall [1997] found the relation to be $L = (0.68\ s) \times W + 1.2\ m$, using measurements taken in a shallow tidal sea. In comparison, measurements made by Kenney [1977] showed that in a shallow lake, L is approximately equal to the water depth and independent of wind speed. Smaller bands are observed to form between and be carried into the larger, more persistent bands in the open ocean [for example Assaf et al., 1971, Katz et al., 1965, Langmuir, 1938] and in lakes [for example Kenney, 1977, Langmuir, 1938], suggesting a dynamical cascade from small scales up to some dominant large scale.

More recent observations in the open ocean [Smith, 1992] and in the laboratory [Melville et al., 1998] record the growth of Langmuir cells, a cell being a pair of the adjacent vortices of opposite sign. Smith [1992] reports that after a sudden increase in wind speed from 8 $m\ s^{-1}$ to 13 $m\ s^{-1}$, prior to which there were no visible signs of Langmuir circulation, streaks with about 16 m spacing, about two thirds of the dominant wind-wavelength, were observed to form, increasing at 40 m/h for the next hour. Melville et al. [1998] report observations of small-scale streaks formed at the surface of a laboratory tank with the wind speed steadily increasing from zero. The near-surface circulations forming the streaks are observed to closely follow the initial growth of the surface wind waves. However, contrary to the open water observations, the scale of the streaks is seen to decrease with increasing wind speed, possibly indicating that the streaks in this case are formed as the result of coherent

structures within the air flow and not by Langmuir circulation (see Section 2.2.1 and discussed further in Section 6.1).

Observations of Langmuir circulation in the North Sea by Graham and Hall [1997] show the ratio of windrow spacing to the water depth to be between 0.3 and 0.5. These values are typical of fetch limited, shallow seas where cells may not be fully developed, so the values for the ratio are less than those reported by Leibovich [1983] of between 0.66 and 1.66 (windrow spacing to the depth of the thermocline) in the open ocean, but similar to that given by Smith [1992] of 0.5, where the cells were still developing.

The duration, or persistence, of individual windrows also appears to vary with environmental conditions. Windrows have been found to be most persistent in the open ocean, where they have been observed to exist for periods in excess of 2 hr [Smith et al., 1987], with separations of about 100 m and down-wind lengths of 1 km. In shallow lakes Kenney [1977] reports windrows of about 300 m length in water of 3 m depth were observed to exist for periods of about 1 hr in steady wind conditions. Thorpe et al. [1994] observed typical windrow lifetimes of $15 - 30$ min in a deep, stratified lake. In comparison, observations from a shallow, tidally-mixed sea, show the durations to be much less: $2 - 5$ min in water of 45 m depth [Thorpe et al., 1994] and about 1.5 min in water of 18 m depth [Graham and Hall, 1997]. In general, the persistence of the windrows, the time between formation and destruction either by amalgamation with neighbouring windrows or break-up of the underlying circulation, was observed to increase with wind-speed.

The currents within the cells, the converging, down and up-welling and enhanced down-wind flow within the windrows, are also found to increase in strength with increasing wind speed. Langmuir [1938] observed drifters to converge upon the windrows at speeds in excess of 3 $cm\ s^{-1}$ and that the downwelling water, confined within a narrow 'jet' beneath the windrow, has a similar velocity. He also observed that the upwelling water, between the surface convergences, occurs over a broader region, with lower velocities of $1 - 1.5$ $cm\ s^{-1}$. Weller and Price [1988] and D'Asaro and Dairiki [1997] found similar patterns of velocity structure, ranging from 1 to 15 $cm\ s^{-1}$. The enhanced down-wind flow within the windrows has been observed

to fall within the same velocity range [Leibovich, 1983], or to be roughly twice the down-wind flow between the windrows. Filatov et al. [1981] found that the convergence currents, u, within the Langmuir cells were typically 3% of the windspeed.

Various forcing mechanisms have been proposed for the formation of Langmuir circulation. A full review of these is given by Leibovich [1983]. The most generally accepted theory is that first suggested by Craik [1977] and further developed by Leibovich [1977] and later termed the CL2 mechanism by Faller and Caponi [1978]. A sketch of the CL2 mechanism is shown in Figure 2.3. It is supposed that an infinitesimal spanwise anomaly occurs in an otherwise regular horizontal current, resulting in the generation of vertical vorticity. This vorticity is then rotated and stretched by the Stokes' drift associated with the surface gravity waves. Thus, water at the surface is accelerated downstream and towards a convergence, where, by continuity, it sinks, leading to an amplification of the initial anomaly and the formation of a circulation pattern.

On reaching the windrows the buoyant material remains trapped until such a time as the local circulation breaks up, perhaps when adjacent cells merge together. Studies by Csanady [1973], Faller and Auer [1988] and Thorpe [1992] have focused on this mechanism for the dispersion of material relative to the wind direction. Csanady [1973] identified the time, T_*, that Langmuir cells exist before breaking down as being critical in determining the across-wind diffusivity. This across-wind diffusivity was simply defined as $K = L^2/T_*$ on dimensional grounds (material being spread a distance L after the break-up of the cell). Faller and Auer [1988] produced a more complex model which included the effects of the windrows meandering, finding that $K = 0.5(u/k^3T_c)^{1/2}$, where T_c is the characteristic timescale for the Langmuir circulation, estimated as $L/0.03$ m s^{-1}, u is the speed of convergent motion, and k is the wavenumber of the cells, $k = 2\pi/L$. Based on an analytical model of cell interaction and break-up, Thorpe [1992] predicted that $T_* = cL/u$ where c is a constant. Observed values of T_* are about 10 - 30 min.

Thorpe et al. [1994] approximated the lateral diffusivity, relative to the mean tracer flow, using a numerical simulation of the motion of particles released into a

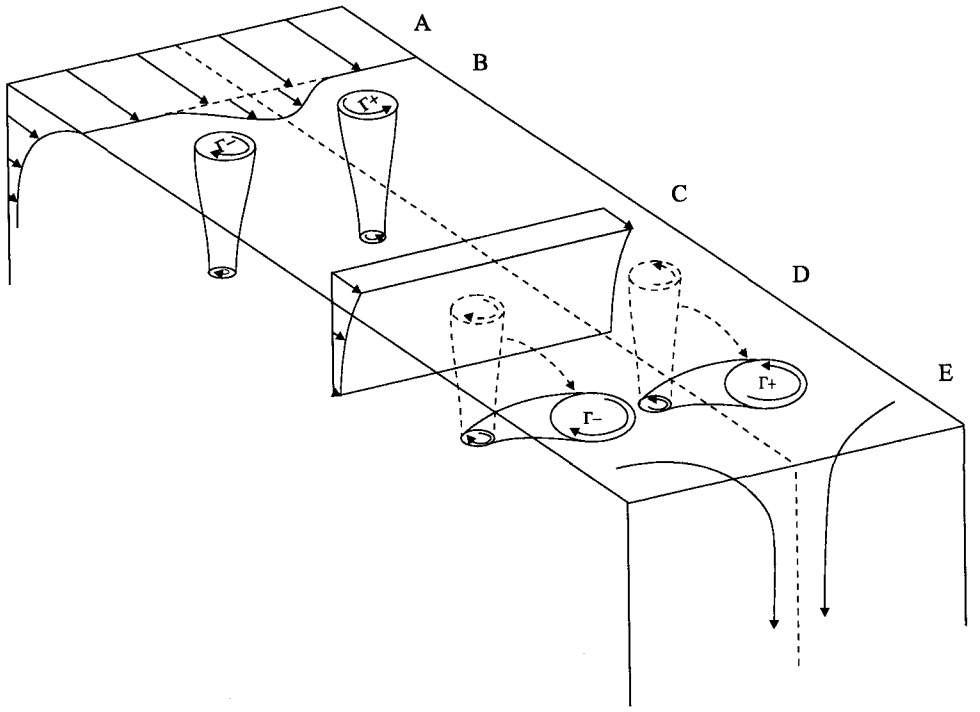

Figure 2.3: Formation of Langmuir circulation by CL2 mechanism [adapted from Leibovich, 1983]. A spanwise irregularity occurs in the surface shear current (A), which generates associated vertical vorticity (B). The Stokes-drift (C), which is horizontal but decreases with depth, rotates and stretches the vertical vorticity (D). Water at the surface is accelerated downstream and towards a convergence, where, by continuity, it sinks, leading to an amplification of the initial anomaly and the formation of a circulation pattern (E).

"frozen field" of windrows defined by side-scan sonar data taken in the southern North Sea. Diffusivities ranged from 5×10^{-3} to 0.5 m^2s^{-1} in winds of 5 to 10 m s^{-1}. Using representative values for wind speed and observed values for L, T_*, and u, Csanady's model gave values for the diffusivity from 0.4 to 0.5 m^2s^{-1}, while Faller and Auer's model produced values ranging from 1.7×10^{-2} to $2.6 \times 10^{-2} m^2s^{-1}$.

2.2 Coherent boundary layer structures

The first carefully controlled and documented observations of structure within turbulent boundary-layer flows were made by Kline et al. [1967] using hydrogen bubble and dye visualisation near the bottom boundary. They observed that the tracers would form into long streaks, roughly aligned with the flow direction, migrating across the flow from regions of relatively high-speed flow to relatively low speed regions, accumulating into the streaks. These streaks have been observed to form over both smooth and rough surfaces [Grass, 1971], to have a spacing of about 100 wall units (a wall unit is a length-scale non-dimensionalised using the kinematic viscosity of the fluid and the shear velocity, $u_\star = \sqrt{(\tau_w/\rho)}$, where τ_w is the bed shear stress and ρ is the water density) and along-stream lengths of 600 to 1000 wall units. Further from the boundary, more irregular streak-like patterns have been observed with cross-stream spacing scaling with the distance from the boundary [Smith and Metzler, 1983]. These streaks have been observed even at Reynolds numbers, Re, as high as 1.5×10^6 [Klewicki et al., 1995]. At a distance of about 50 wall units, the regular, streaked pattern breaks down to a pattern which appears to be produced by a more complex tangle of vortices, whose scales increase with increasing distance from the wall [Smith, 1996].

For most of the time the boundary layer consists of these two regions, an inner near-wall layer displaying the persistent streaky structure and an outer layer, dominated by vortex motions of varying strengths. However, there are brief intermittent periods in which the two regions interact very strongly, referred to as 'bursting' by Kline et al. [1967]. During a 'burst', a near-wall low-speed streak breaks up and

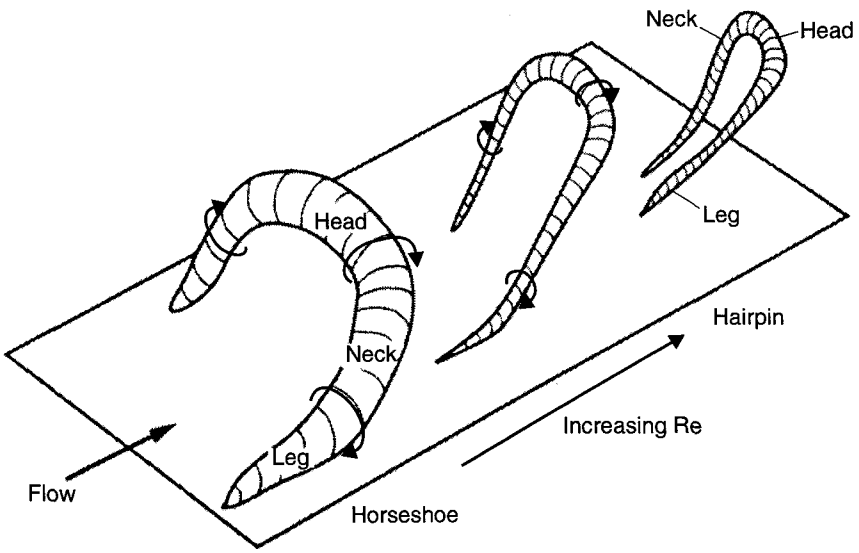

Figure 2.4: Sketch of horseshoe and hairpin vortices [after Robinson, 1991]. Sense of vorticity indicated by arrows.

erupts, leading to the ejection of near-wall fluid away from the wall into the outer region of the boundary layer. Subsequently, high speed, outer region fluid appears to move toward and penetrate the wall layer, 'sweeping' away the remnant chaotic motion resulting from the 'burst' [Corino and Brodkey, 1969]. The wall layer streaks then reform until the bursting process reoccurs. Experiments in a wind tunnel by Rao et al. [1971] showed that the mean time between bursts, $\overline{T}$, scales with the outer region variables of boundary layer thickness, δ, (or flow depth in depth-limited flows) and free-stream velocity, U. From their observations at Re between 10^3 and 10^4 they proposed the relation, $\overline{T} = a\delta/U$, where $a \simeq 5$. Jackson [1976] reports other laboratory observations and finds that a ranges from 3 to 7.

Experimental and numerical studies have shown that the dominant form of the vortices in the outer layer is that of a 'horseshoe' at low Reynolds numbers or, at higher Reynolds numbers, of a 'hairpin'. The form of these is sketched in Figure 2.4. The 'heads' of the structures are inclined downstream of the trailing 'legs'. A mechanism for the production of these 'hairpins' (since we are considering high Reynolds number

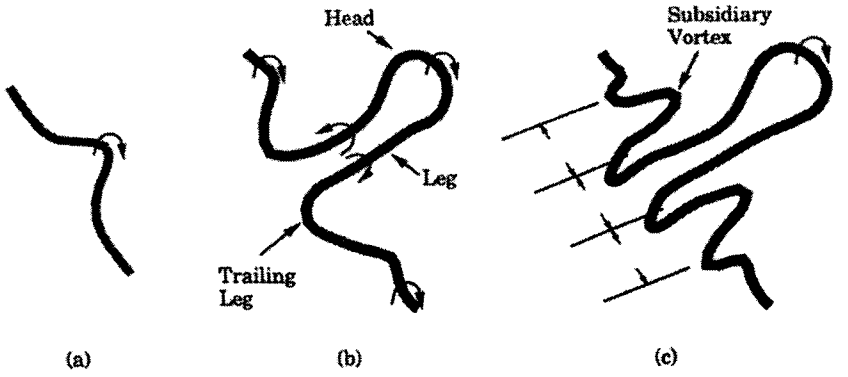

Figure 2.5: Formation and evolution of a hairpin vortex in a shear flow [from Smith, 1996]. The vortex is advected from left to right and the sense of vorticity is shown by the arrows.

geophysical flows) is shown in Figure 2.5. A small initial three-dimensional distortion in a two-dimensional line vortex which is aligned transverse to a sheared flow, will grow rapidly. A 'head' forms and moves up away from the boundary, while at the same time, 'legs' form and move down towards it. The head is stretched out from the legs in the along-stream direction by the sheared flow, and so the vorticity intensifies. The characteristic spacing of the legs mainly depends upon the strength of the background shear [Smith et al., 1991], with higher shear or a lower vortex strength relative to the shear producing a smaller between-leg spacing. Asymmetrical vortex structures are also formed depending upon the initial shape of the distortion via the same process of vortex stretching. Large structures in the outer region of the boundary layer are probably created by the amalgamation of the relatively small-scale hairpin vortices generated close to the boundary [Smith et al., 1991].

It has also been shown that the low-speed streaks, observed in the inner region of the boundary layer, are produced by the passage of the trailing legs of the hairpin vortices. These streaks, produced by the vortices closest to the boundary or by the legs of vortices which manage to penetrate down through the flow, will have a cross-stream scale which is equivalent to the spacing of the legs of the vortices themselves [Haidari and Smith, 1994]. Similarly, the along-stream extent of the streaks will be limited by the period for which the vortices are in close proximity to the boundary,

before either dissipating through viscous action or mutual induction of the vortices away from the boundary. The production of the near-boundary streaks is discussed further by, among others, Robinson [1991] and Smith [1996].

Bursting, the process which indicates the abrupt termination of a near-boundary streak, is also produced by the proximity of the vortices as they pass over the boundary. Simplistically, a region of adverse pressure is setup in the streamwise direction as a vortex is advected along the boundary. This acts against the inertia of the flow, so compressing it. If the fluid is incompressible, the volume of the compressed region must be conserved, leading to a rapid and substantial vertical elongation of the region (i.e. near-boundary fluid is ejected away from the boundary). Thus, the net result is the ejection of regions of high vorticity into the outer region of the boundary layer, which in turn create the strong shear layers which subsequently roll-up into new hair-pin like vortices. A detailed review of this process is given by Smith [1996].

2.2.1 Experimental and numerical observations of the formation of boils and eddies at the free surface

During laboratory experiments on the coherent structures within a turbulent boundary layer, Grass [1971] observed 'the presence of boils of fluid on the free surface'. He proposed that the boils, regions of locally upwelling water, were 'lumps' of low momentum fluid ejected during bursts from near to the boundary, reaching and interacting with the free surface. More recent experiments by Komori et al. [1989] showed that the decelerated fluid that is ejected upwards from the boundary during the busting process would almost always reach the free surface and renew it, and that mass transfer across the free surface is dominated by these large-scale surface renewal motions.

In a series of experiments in a smooth-bottomed laboratory channel, Kumar et al. [1998] have elucidated the relationship between the coherent structures within the boundary layer and the boils and eddies observed at the free surface. Figure 2.6 shows an example of the evolution of a large scale coherent structure, as viewed from

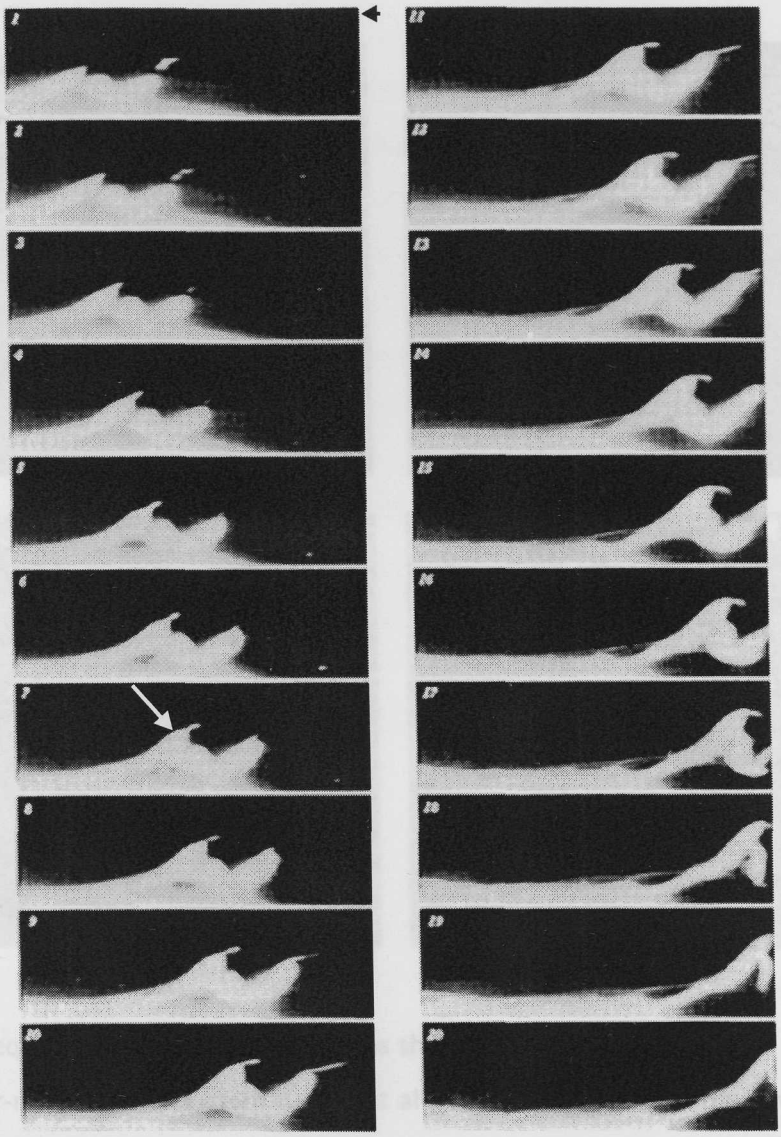

Figure 2.6: Sequence of images showing the formation and evolution of a large scale coherent structure [from Kumar et al., 1998]. Each image is a thin vertical section of a laboratory channel, separated by $1/30$ s. The depth of the flow is 2.5 cm and $Re = 2800$ and the flow is from left to right. Light coloured fluorescein dye is injected into the flow at the channel bed (at the bottom of the images) and is transported towards the water surface (indicated by the arrow in the first image) in a large scale structure.

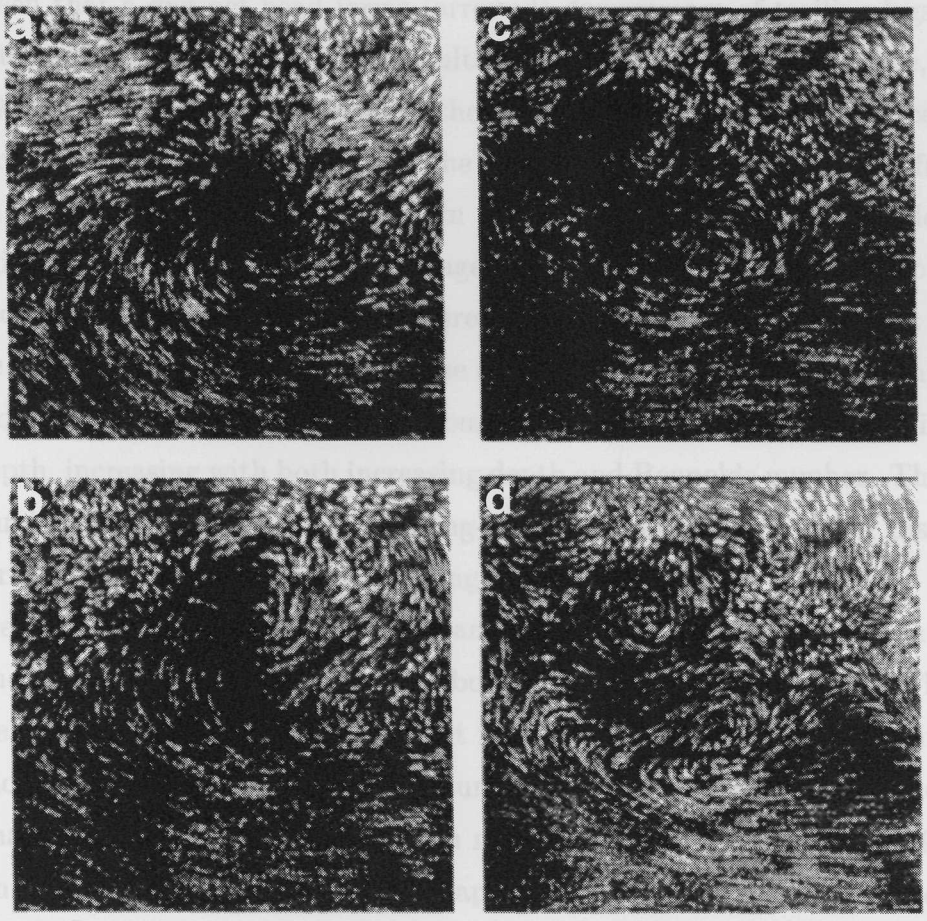

Figure 2.7: Sequence of time exposure images showing the formation of a boil and subsequent pair of counter-rotating eddies [from Kumar et al., 1998]. The depth of the flow is 2.5 cm and $Re = 2800$. Each image is approximately 5 cm square. The images are taken moving with the same velocity as the mean flow, looking vertically down on the surface of the channel with the flow from left to right. The light streaks are microballoons floating on the surface, so that dark regions indicate regions of surface upwelling and divergence. The interval between images is about 0.4 s. The boil in **a** is generated by a structure similar to that seen in Figure 2.6 as it approaches the surface, and would first become visible when the structure was at the approximate vertical position shown in the image at the top of the second column of Figure 2.6.

the side, from its origin in the strongly sheared region near the bed of the channel. It can be seen that a distinct head forms (arrowed) downstream of trailing legs, which rises up towards the free surface. By simultaneously viewing the free surface, Kumar et al. [1998] showed that as the head of the structure approaches the surface, a boil is formed. An example of the boil and the subsequent evolution of the surface flow is shown in the sequence of images shown in Figure 2.7. The boil is visible as the dark region in the centre of the first image, the upwelling water leading to surface divergence, sweeping away the light coloured floating tracers. In subsequent images, it can be seen that the boil increases in size and that a pair of counter-rotating eddies is formed. The size of these eddies was found to be roughly four to seven times the water depth, increasing with both increasing depth and Reynolds number. The eddies were found to be persistent for large along-stream distances until either dissipating slowly or being engulfed in a new upwelling boil.

Numerical simulations by Pan and Banerjee [1995] show the same relation between the subsurface structures and the boils and eddies at the surface. They also show that the eddies most probably result from surface parallel vorticity within the subsurface structures reattaching to the surface. This reattachment of vorticity and the formation of the eddies is also seen in numerical simulations by Tsai [1998] and shown in Figure 2.8. Here a horseshoe shaped vortex approaches the surface, where the head breaks and the two legs reattach to the surface, forming a pair of counter rotating eddies.

2.2.2 Observations in rivers and estuaries

Boils and eddies are commonly observed in rivers [for example Coleman, 1969, Jackson, 1976, Kostaschuk and Church, 1993, Matthes, 1947], estuaries [for example Rood and Hickin, 1989] and narrow tidal straits [for example Longuet-Higgins, 1996]. Most of these studies report only observations of turbulence generated by flow over large-scale dunes (with heights typically 20% of the water depth). However, Jackson [1976] reports some observations of boils in a river with a flat bed consisting of coarse grain

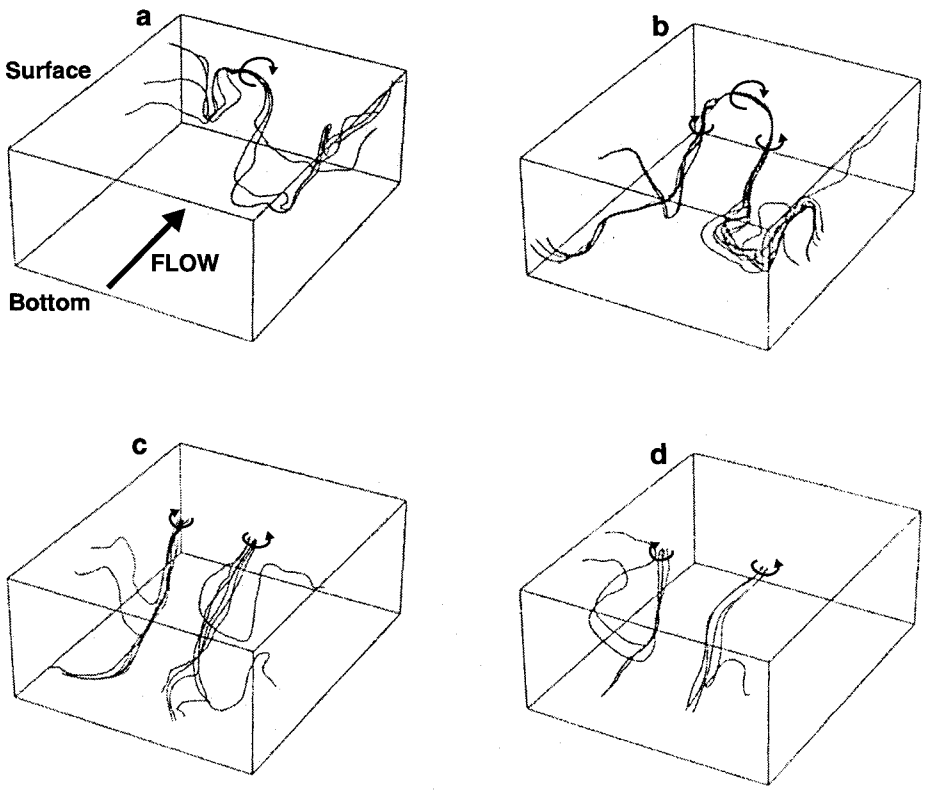

Figure 2.8: Direct numerical simulation of turbulent flow below a free surface [after Tsai, 1996] shown by bundles of vortex filaments ($Re = 1000$). The sense of vorticity and the direction of the flow are shown by arrows. The evolution of a horseshoe vortex as it approaches the free surface is seen (**a** and **b**), and the subsequent reattachment of the legs to the surface leading to the formation of a pair of eddies (**c** and **d**).

material (about 2 mm grain size). It was noted that these boils were less vigorous than their counterparts in equal depths over strongly rippled beds, although their frequency of appearance was not noticeably different. In a period of 20 min, 75 boils were observed in water 3.7 m deep, flowing at 1.31 $m\ s^{-1}$ ($Re = 4 \times 10^6$), with a mean boil periodicity at a point on the water surface of 16 s and standard deviation of 15 s. This mean periodicity of the boils corresponds well to the mean periodicity of the bursts observed in laboratory experiments, with the scaling factor $a = 5.7$ falling within the range (3-7) of the other experiments.

The boils are visible at the water surface because they exhibit higher sediment concentrations (with larger particle sizes) than the surrounding water [for example Kostaschuk and Church, 1993, Rood and Hickin, 1989], because the stream-wise fluid velocity within them is significantly less (perhaps by $10-30\%$) than the mean ambient flow [Jackson, 1976], and because of the steepened capillary waves found around their perimeter [Longuet-Higgins, 1996]. The sediment originates at the bed, scoured up and transported to the surface in coherent vortical structures termed as 'kolks' by river engineers [Matthes, 1947].

These boils, and the kolks that produce them, closely resemble the structures observed at much lower Reynolds numbers in the laboratory channels and numerical simulations described in the previous section.

2.2.3 Turbulence measurements at sea

The first observations of turbulent motions in tidal flows in the open sea specifically attributed to the bursting process were made by Heathershaw [1974]. Intermittent fluctuations in the near-bed velocity record revealed events consisting of fluid with relatively low horizontal velocity (as little as 50% of the mean flow) and high upward vertical velocity (up to 25% of the mean horizontal velocity) corresponding to bursts. Similarly, sweeps consisting of inrushing, relatively high horizontal velocity fluid were also identified. Similar observations of busting and sweeping motions were reported by Gordon [1974] within the flow in a tidal estuary.

Observations by Bowden and Howe [1963] show that the turbulent fluctuations are greatest during the early decelerating parts of the tidal cycle, so that there is a lag between the maximum velocity and turbulent motions. This lag, or hysteresis has also been recorded in velocity measurements in estuaries [French and Clifford, 1992, Kawanisi and Yokosi, 1994, Schroder and Siedler, 1989], in numerical simulations [Baumert and Radach, 1992], in measurements of suspended sediment concentration in a shallow tidal sea [Jago and Jones, 1998], and in observations of boils, high in suspended sediment, visible at the water surface in an estuary [Rood and Hickin, 1989]. It is also consistent with the laboratory observations of Kline et al. [1967] that the intensity and frequency of bursting increase under adverse pressure gradients. Jago and Jones [1998] observed that the time lag of the peak concentration of suspended sediment increased with increasing height above the sea bed, showing that it also takes some time for the turbulent fluctuations to rise up through the water column.

2.3 Past measurements of dispersion

In the absence of wind and significant bottom roughness, and when the Reynolds number, $Re = UH/\nu$, is very large, dispersion at the surface of unstratified waters is characterised by a dimensionally correct combination of two dimensional quantities, the tidal current U and water depth H, and is independent of kinematic viscosity, ν. Bowden [1965] parameterised the horizontal diffusion coefficient in the presence of tidal currents by using the expression

$$K_T = \beta UH \tag{2.1}$$

where β is a constant. More recent studies [for example Fischer, 1973] have parameterised the horizontal diffusion coefficient using the expression

$$K_T = \alpha u_\star H \tag{2.2}$$

where now α is a constant and $u_\star$ is the shear velocity. While the former parameterisation (Equation 2.1) is more 'simplistic', it does contain an implicit drag coefficient,

C_D, through the equation

$$U = u_\star / C_D^{1/2}. \tag{2.3}$$

However here (Equation 2.3), the drag coefficient appears only as a square root and the formula thus has reduced sensitivity to its value. Therefore this simpler version (Equation 2.1) will be adopted to allow easy comparison between estimates made within this present study and those of previous works outlined in the following sections.

2.3.1 Laboratory measurements

There are few laboratory measurements of the lateral dispersion of floating particles in flow over a flat channel bed. Fischer [1973] reviews laboratory experiments on the lateral dispersion of buoyant particles (shown in Table 2.1), from which a mean value of $\beta = 1.03 \times 10^{-2} \pm 4.4 \times 10^{-3}$ ($\pm$ implies an error estimate of one standard deviation) is found. These measurements were however taken at only moderate Reynolds numbers ($Re = 1.6 \times 10^4$ to 6.0×10^4). Figure 2.9 shows that there is no obvious scaling of β with Reynolds number. Fischer et al. [1979] note that, in experimental channels, the width of the channel also appears to play a role in the lateral dispersion and, although the precise nature of this is unclear, they suggest approximate error limits of 50% for the values described above.

2.3.2 Measurements at sea

Possibly the earliest field experiments carried out into small-scale dispersion in the sea were by Richardson and Stommel [1948]. They measured the change in separation of pairs of floating drifters (pieces of parsnip, "because it is easily visible, and because it is almost completely immersed so as not to catch the wind") over a short period of time (30 s) in water about 2 m deep. Their result, that the rate of dispersion of the pairs of floats followed the same power law observed in atmospheric experiments, is flawed both for the reasons acknowledged by the authors, that the supporting legs

Source	U $(cm\ s^{-1})$	H (cm)	Re $(\times 10^4)$	K_y $(cm^2 s^{-1})$	β $(\times 10^{-3})$
Engelund [1969]	30.0	5.5	1.65	4.0	24.2
	30.6	17.3	5.29	6.5	12.3
Prych [1970]	43.3	4.1	1.77	1.52	8.6
	42.4	4.1	1.74	1.63	9.4
	42.5	4.1	1.74	1.69	9.7
	42.6	4.1	1.75	2.00	11.5
	42.0	4.1	1.72	1.33	7.7
	54.3	6.6	3.58	3.32	9.3
	53.2	6.6	3.51	3.14	8.9
	53.7	6.6	3.54	2.97	8.4
	54.5	11.1	6.05	4.78	7.9
	53.7	11.1	5.96	4.49	7.5
	53.5	11.1	5.94	4.70	7.9
				Mean	10.3
				StDev	4.4

Table 2.1: Results from laboratory experiments for the lateral dispersion of floating particles.

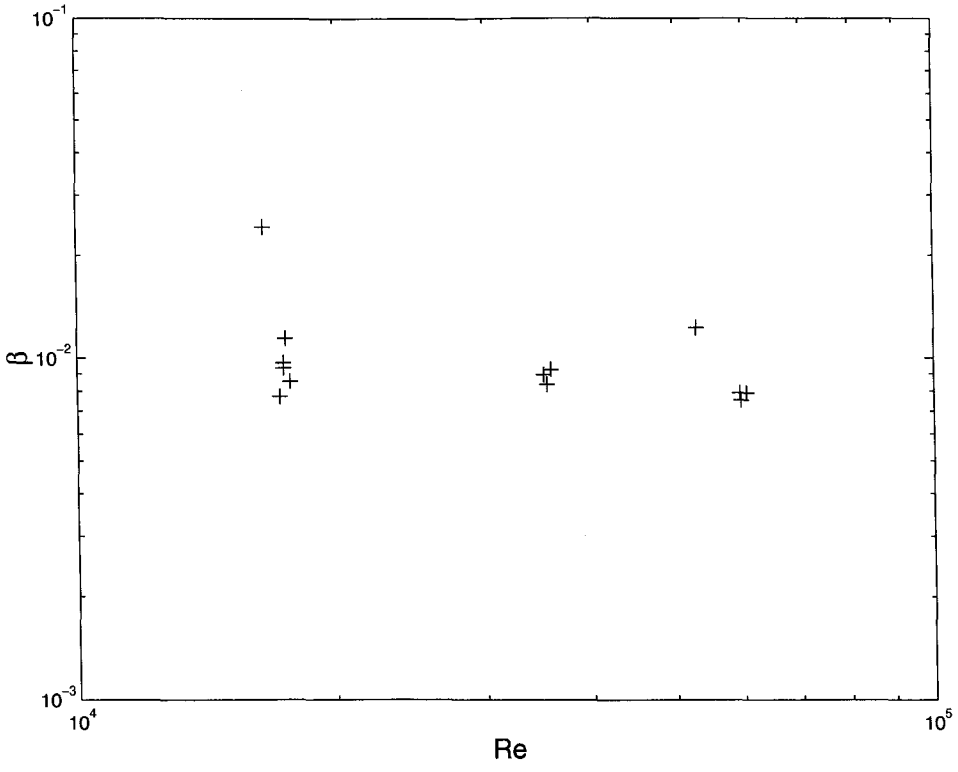

Figure 2.9: β plotted against Re from the experimental data shown in Table 2.1.

of the pier that they were making their measurements from may have interfered with the flow of the water, and that they condensed their results down to two points, to which it is possible to fit any power law!

Subsequently, there have been innumerable studies of the horizontal and vertical dispersion of material, mostly neutrally buoyant dye, at both short and long time scales and over both small and large spatial scales (for example Bowden et al. [1974], Bowden and Lewis [1973], Elliott et al. [1997], Elliott and Hurford [1989], Okubo [1971]). However, there have been few in which the conditions have been suitable to allow for the clear separation of the effects of individual processes on dispersion. Studies investigating the role of Langmuir circulation on dispersion have been reviewed in Section 2.1.

Bowles et al. [1958] report results from a series of dispersion experiments in the English Channel, carried out to asses the suitability of a region of the Dorset coast for the disposal of radioactive material. In conjunction with dye releases, they also released a group of floating particles (plastic envelopes) and measured their dispersion by the tidal current during a period of near-calm wind speeds. At $Re = 1.4 \times 10^7$, they report values of β ranging from 3.9×10^{-3} to 1.15×10^{-2}. These are very close to those found in the laboratory experiments reviewed in the previous section.

More recently, a series of experiments were carried out in the southern North Sea, designed specifically to investigate dispersion processes at and near to the sea surface. Morales et al. [1997] report the results from measurements made of dye released from a fixed, continuous source at the sea surface into a tidal flow, and these are summarised in Table 2.2. The lateral diffusivity was calculated from transects of dye concentration made across the width of the plume at different down-stream distances from the source, the down-stream distance being converted to a dispersion time using the mean current speed. The authors note the large scatter of the measurements from within each plume showing that for similar dispersion times, the dye could either be spread over a large across-stream distance, or confined in a relatively small region. It can be seen that the values of β cover the range 0.37×10^{-3} to 2.97×10^{-3} with a mean of $1.16 \pm 0.67 \times 10^{-3}$. However, Morales et al. [1997] were still able to produce

empirical relations between the diffusivity and the wind and current speed.

It should be noted that measures of horizontal diffusivity from neutrally-buoyant dye releases are not exactly comparable to those from the release of buoyant material. This is because the dispersion of the dye will also be controlled by other mixing processes, principally shear dispersion [see Bowden, 1965], which will act to increase the diffusivity. These additional processes are outwith the scope of this present study, whose aim is to investigate processes which directly affect buoyant material at the water surface. However, in the absence of more directly applicable data, it is still very useful to make comparisons with these measurements. Further, the processes expanded upon in the following chapters will, without doubt, also affect the patterns of dispersion of neutrally buoyant material (for example Kenney [1977]), giving insight into the scatter in measurements within individual plumes noted by Morales et al. [1997] among others.

Number	$W(m\ s^{-1})$	$K_y(\times 10^{-4} m^2 s^{-1})$	$H(m)$	$U(ms^{-1})$	$\beta(\times 10^{-3})$
1	5.33	188	45	0.33	1.27
2	4.54	198	45	0.60	0.73
3	4.80	258	45	0.38	1.51
4	6.65	169	45	0.69	0.54
5	6.48	338	45	0.98	0.77
6	8.39	438	45	0.59	1.65
7	1.61	194	45	0.62	0.70
8	4.75	273	45	0.78	0.78
9	3.33	161	45	0.41	0.87
10	5.11	133	45	0.80	0.37
11	10.35	199	45	0.17	2.60
12	1.52	187	45	0.14	2.97
13	4.96	514	45	0.70	1.63
14	6.47	318	45	0.81	0.87
15	5.77	613	45	0.92	1.48
16	7.89	38	45	0.96	0.88
17	2.50	183	45	0.69	0.59
18	2.17	227	45	0.59	0.86
19	5.43	268	45	0.56	1.06
20	7.55	298	45	0.61	1.09

Table 2.2: Diffusivity measurements from the southern North Sea (data from Morales et al. [1997]). U and W are the 'representative' current (at 15 m depth) and wind speed respectively during each experiment.

Chapter 3

Estimation of dispersion by Langmuir circulation

As reviewed in Section 2.1, previous estimates of the dispersion produced by Langmuir circulation have been calculated relative to the axis of the cells - or the wind direction. In this chapter numerical and analytical models are developed which describe the dispersion of a plume of buoyant particles under the combined action of an array of Langmuir cells and a steady current; analogous to a plume of oil being released from a fixed source into a steady flow.

Thorpe [1995b] devised a simple analytical model of the spread of floating material from a source fixed at the sea surface in the presence of steady Langmuir cells and a mean tidal current. The patterns of dispersion produced by this model, in which the convergent and enhanced downwind flows within the Langmuir circulation are described by sinusoidal functions, is explored further using a numerical adaptation in Section 3.1. Whilst this gives insight into the diffusion mechanisms, and diffusion can be estimated for specific input parameters, it proved to be computationally expensive. An analytical model developed by Nimmo Smith and Thorpe [1999] (see also Appendix B) is shown in Section 3.2 and gives results in a more compact form.

3.1 Numerical

3.1.1 The model

A steady and regular array of Langmuir cells is advected by a steady current, U (in the X direction - see Figure 3.1) past a fixed reference point from which floating particles are released at a constant rate, r_p. The cells induce a steady pattern of flow at the surface which is represented by x and y components $u_c = u \sin kx$ (convergence) and $v_c = v/2 - v/2 \cos kx$ (increased downwind advection in windrows) respectively, with the x direction aligned normal to the axis of the circulation which is in turn aligned with the wind direction, and k is the wavenumber of the circulation pattern such that $L = 2\pi/k$ is the separation of neighbouring windrows. The frame of reference (x, y) is advected with the steady current so that the position $x = 0$ lies midway between windrows, on the line of surface divergence. Components u and v are the maximum convergence speeds and the maximum downwind speeds in the windrows respectively. A fixed frame of reference (X, Y) is adopted which is aligned with the direction of the current and at an angle, α, to the right of the direction in which the wind is blowing. Floating particles released at the reference point $(X = Y = 0)$ into this regime are free to move with their motion given by

$$\frac{dX}{dt} = U + u \sin kx \sin \alpha + (v/2 - v/2 \cos kx) \cos \alpha \tag{3.1}$$

$$\frac{dY}{dt} = (v/2 - v/2 \cos kx) \sin \alpha - u \sin kx \cos \alpha \tag{3.2}$$

where now $x = (X - Ut) \sin \alpha - Y \cos \alpha$ and t it the time since release began, when it is assumed that a line of divergence $(x = 0)$ passed through the origin of the frame of reference $(X = Y = 0)$.

3.1.2 Assumptions

The following assumptions have been made in order to simplify the model and decrease the number of variables:

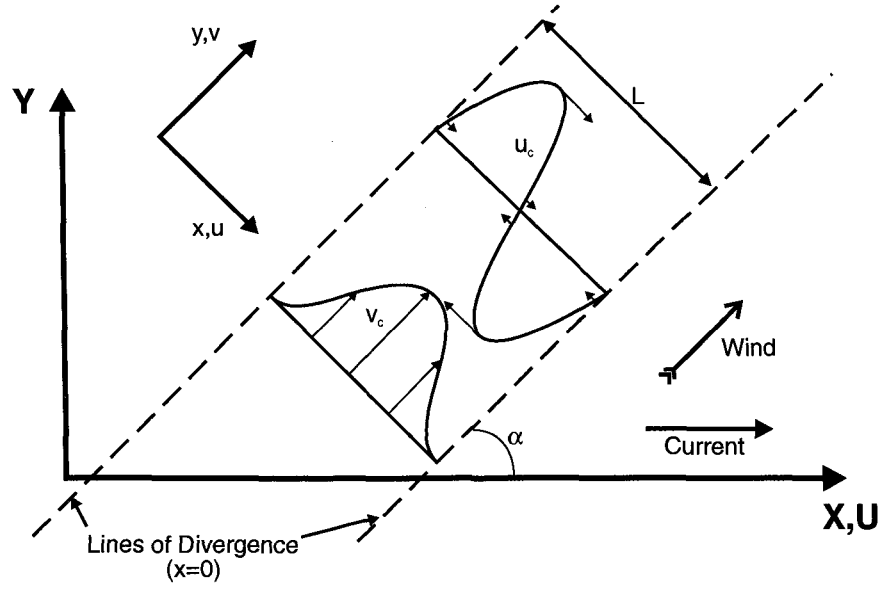

Figure 3.1: Components of the numerical model of dispersion by Langmuir circulation and a mean current.

- Any background wind-drift is neglected (i.e. $v_c = 0$ at $x = 0$).
- The cells remain steady, without breaking down.
- The array of cells is totally regular, with no variation of scales.
- The current advecting the cells is steady throughout the period of study.

3.1.3 Results

Examples of the patterns produced as the plumes of particles are dispersed by the Langmuir circulation with different values of α, L and u/v are shown in Figures 3.2, 3.3 and 3.4 respectively. Throughout, it can be seen that close to the release point the plumes initially meander, while further down-current from the source, the particles are carried into and trapped within windrows.

Figure 3.2 shows the early stages of dispersion of the particles for different alignments between the windrows and current. In each case the spacing between windrows,

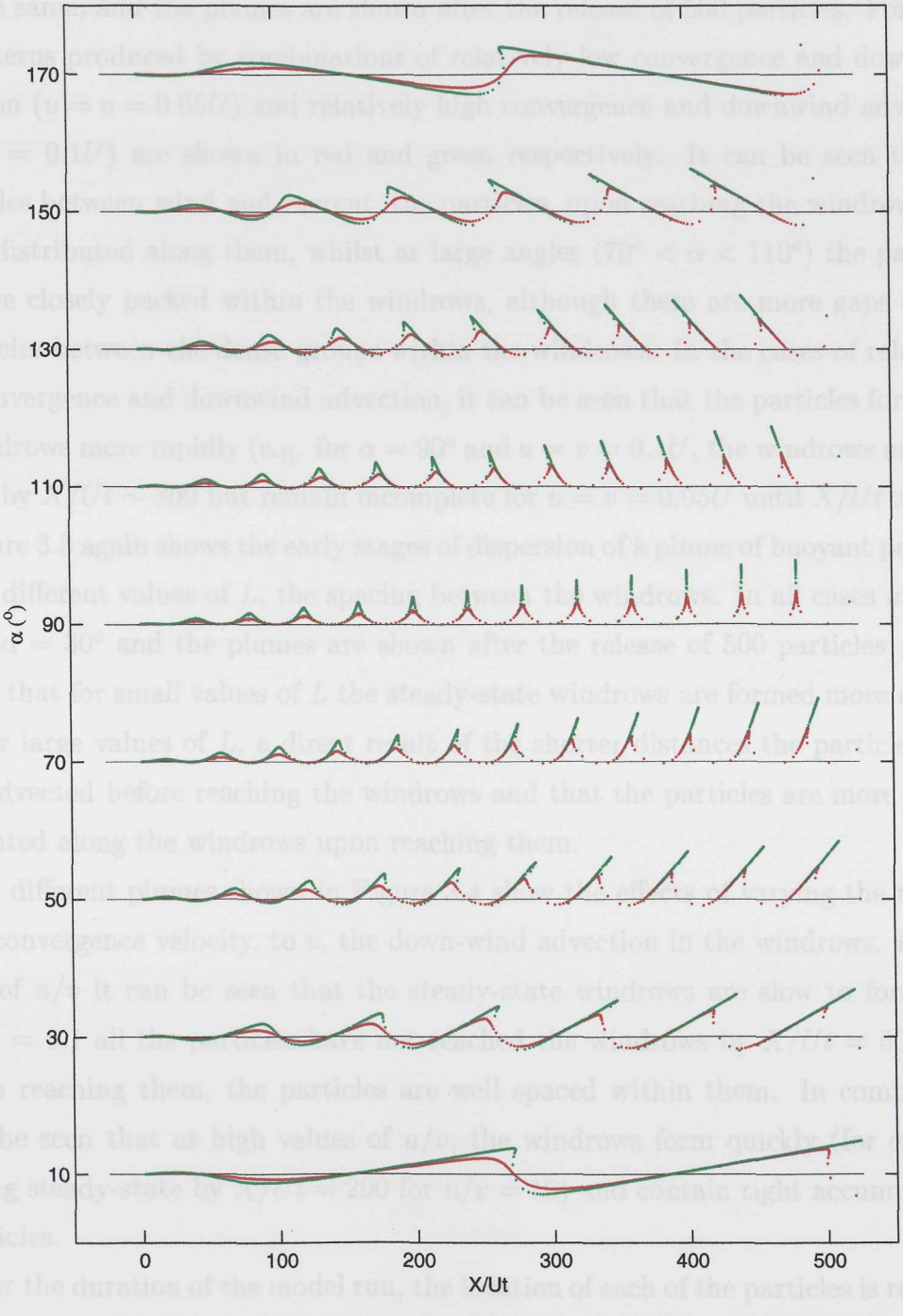

Figure 3.2: Dispersion of buoyant particles by Langmuir circulation with different orientations between wind and current, α. All the runs shown are after the release of 500 particles ($t = 500/r_p$). The x-axis shows the downstream distance non-dimensionalised by the current, U and dispersion time, t, and the y-axis is to the same scale. The numbering on the y-axis refers to the value of α used for each model run and the spacing of the cells is given by $L = 0.08Ut$. The runs in red are for $u = v = 0.05U$, the runs in green for $u = v = 0.1U$.

L, is the same, and the plumes are shown after the release of 500 particles. For each, the patterns produced by combinations of relatively low convergence and downwind advection ($u = v = 0.05U$) and relatively high convergence and downwind advection ($u = v = 0.1U$) are shown in red and green respectively. It can be seen that at low angles between wind and current, the particles, upon reaching the windrows, are widely distributed along them, whilst at large angles ($70^o < \alpha < 110^o$) the particles are more closely packed within the windrows, although there are more gaps devoid of particles between the dense groups within the windrows. In the cases of relatively high convergence and downwind advection, it can be seen that the particles form into the windrows more rapidly (e.g. for $\alpha = 90^o$ and $u = v = 0.1U$, the windrows are fully formed by $X/Ut \sim 300$ but remain incomplete for $u = v = 0.05U$ until $X/Ut > 500$).

Figure 3.3 again shows the early stages of dispersion of a plume of buoyant particles but for different values of L, the spacing between the windrows. In all cases $u = v = 0.05U$, $\alpha = 30^o$ and the plumes are shown after the release of 500 particles. It can be seen that for small values of L the steady-state windrows are formed more quickly than for large values of L, a direct result of the shorter distances the particles have to be advected before reaching the windrows and that the particles are more closely distributed along the windrows upon reaching them.

The different plumes shown in Figure 3.4 show the effects of varying the ratio of u, the convergence velocity, to v, the down-wind advection in the windrows. For low values of u/v it can be seen that the steady-state windrows are slow to form (e.g. for $u/v = 0.1$ all the particles have not reached the windrows by $X/Ut = 500$) and that on reaching them, the particles are well spaced within them. In comparison, it can be seen that at high values of u/v, the windrows form quickly (for example reaching steady-state by $X/Ut = 200$ for $u/v = 10$) and contain tight accumulations of particles.

Over the duration of the model run, the location of each of the particles is recorded at regular intervals, along with the time for which each particle has been dispersing to reach that location. From this it is then possible to calculate the variance, σ_y^2, of the mean position of all the particles normal to the current at each different dispersion

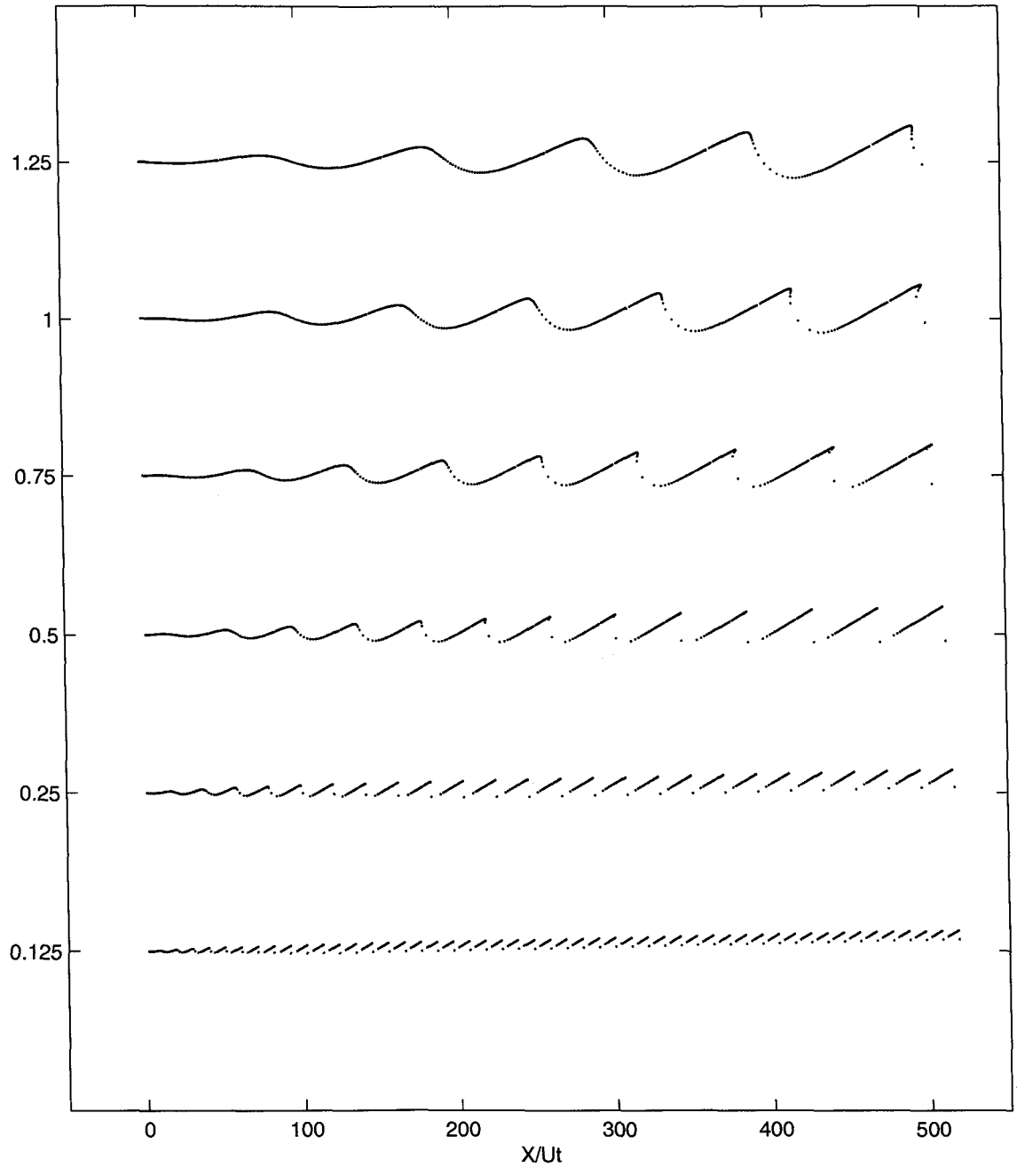

Figure 3.3: Dispersion of buoyant particles by Langmuir circulation, with varying cell spacings. All the runs shown are after the release of 500 particles ($t = 500/r_p$) and $\alpha = 30^o$. The x-axis shows the downstream distance, X, non-dimensionalised by the current, U, and dispersion time, t, and the y-axis is to the same scale. The numbering on the y-axis refers to the value of L, relative to that used in Figure 3.2. Throughout, $u = v = 0.05U$.

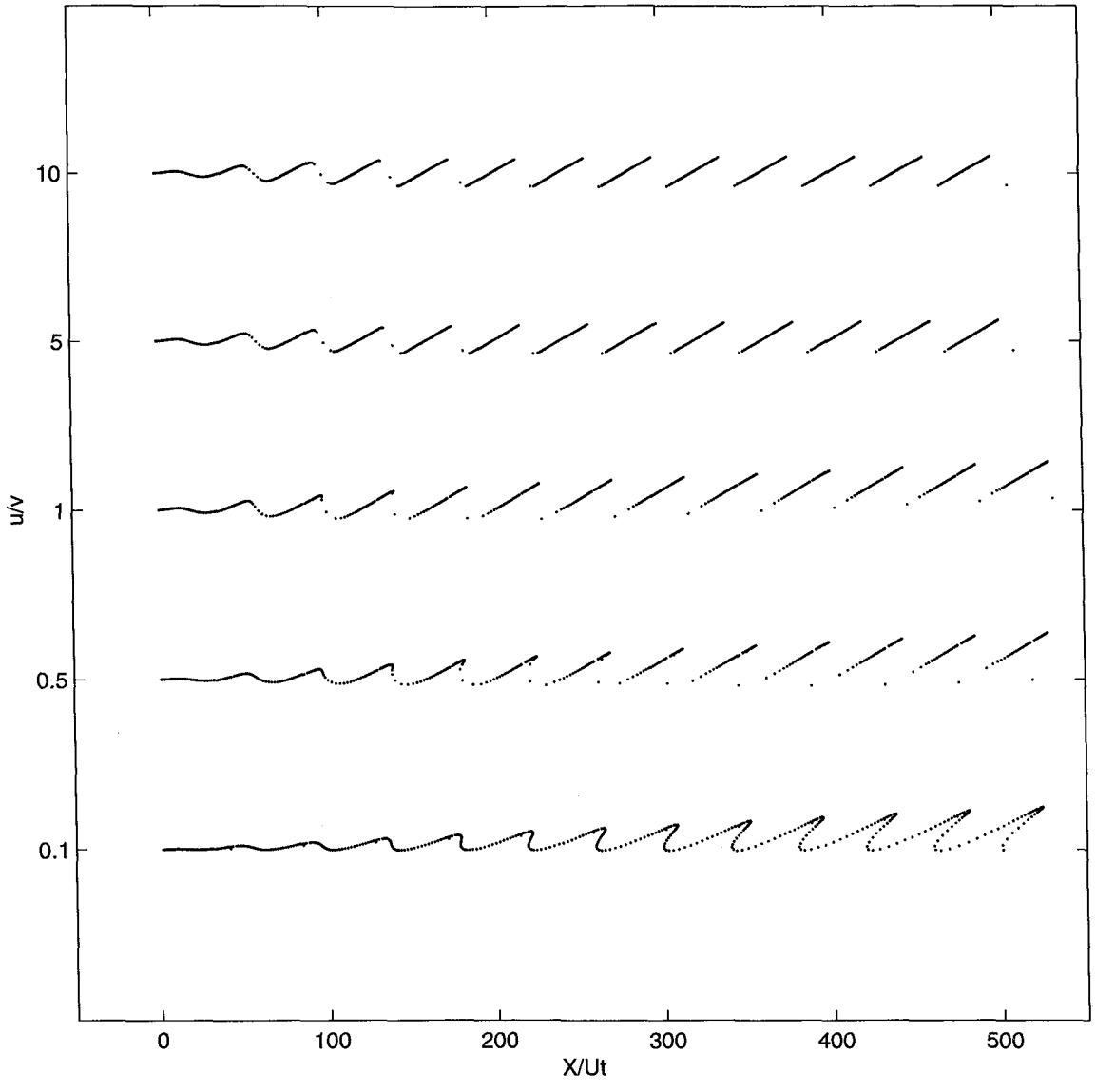

Figure 3.4: Dispersion of buoyant particles by Langmuir circulation, varying u/v. The x-axis shows the downstream distance non-dimensionalised by the current, U and dispersion time, t, and the y-axis is to the same scale. The numbering on the y-axis refers to the value of u/v used for each model run and the spacing of the cells is given by $Lr_p/U = 20$. All the runs shown are after the release of 500 particles ($t = 500/r_p$) and $\alpha = 30^o$.

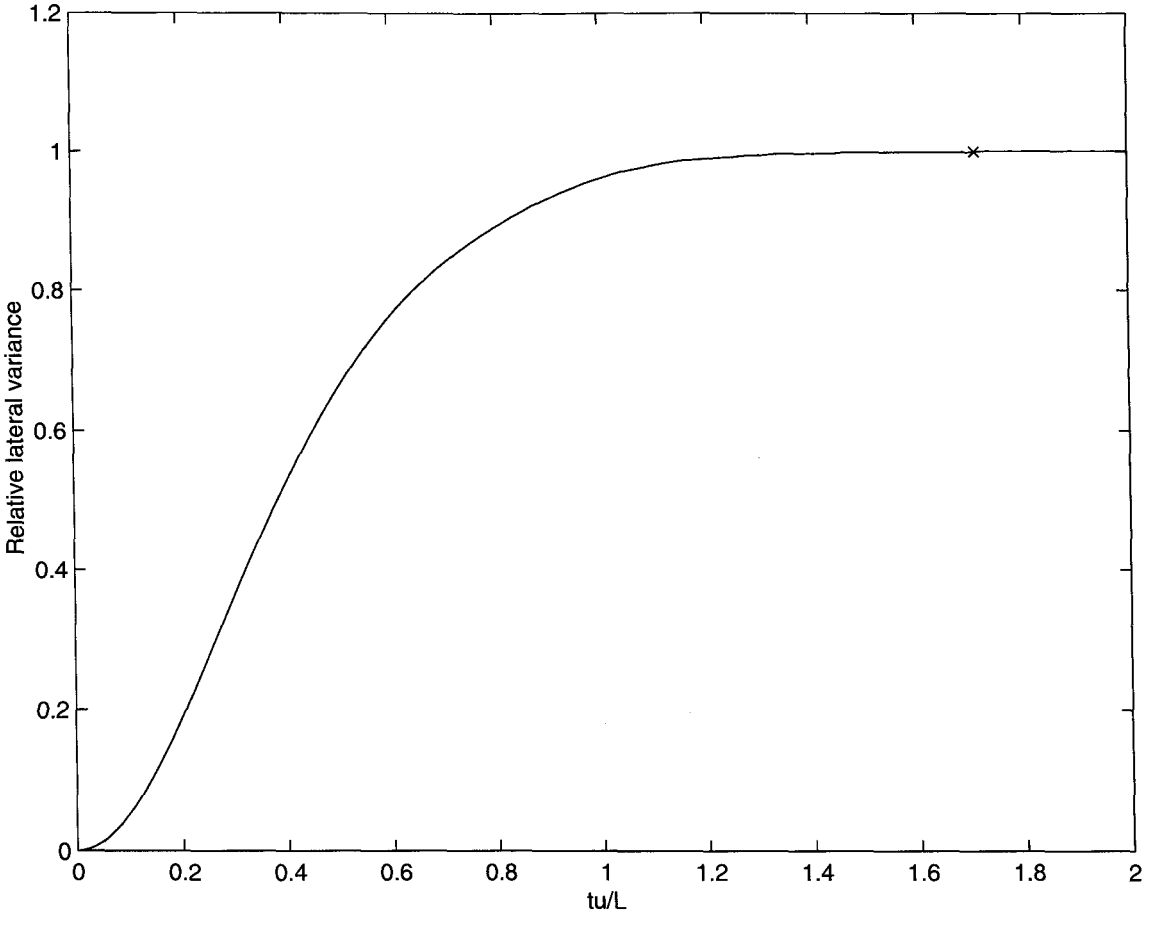

Figure 3.5: Example of the evolution of the lateral variance, σ_y^2 with dispersion time, t (non-dimensionalised by the characteristic timescale of the Langmuir circulation, L/u). The location 'x' indicates the position where the value of σ_y^2 first becomes less than 0.1% different to the mean of the subsequent 100 data points, an arbitrary measure of the pattern of particles reaching 'steady-state'.

time. Figure 3.5 shows how the lateral variance, σ_y^2, changes with dispersion time t (non-dimensionalised by the characteristic timescale of the Langmuir circulation, L/u). It can be seen that the lateral diffusivity initially increases slowly during the period, $t \lesssim 0.1L/u$, in which the particles are first being drawn into the windrows - the period equivalent to the time of formation of the small meanders seen in the figures showing the patterns formed by the particles during the early stages of dispersion (for example Figure 3.2, $\alpha = 30^o$, $X/Ut \lesssim 100$). Next, the lateral variance increases rapidly for the period in which the particles are progressively reaching the windrows and being advected along them, leading to the increased dispersion of the particles. The rate of increase of the lateral variance decreases from $t \gtrsim 0.5L/u$, the time when the majority of the particles released into any one Langmuir cell have reached the windrows. When $t \gtrsim 1.2L/u$, the lateral variance shows very little change, corresponding to the period in which all the particles have reached the windrows and so are in fixed positions relative to each other.

To allow comparison with previous studies, a single for the lateral diffusivity, K_y, can now be calculated according to $K_y = \sigma_y^2/2T_D$, where T_D is the dispersion time at which the variance becomes constant (the time when all the particles have reached the windrows, and their distribution has become constant). T_D is calculated numerically from the model output using an arbitrary threshold to find the dispersion time at which the value of σ_y^2 is within 0.1% of the mean of the subsequent 100 points, the location of this point is shown in Figure 3.5 at x. The effect of varying each of L, u/v and α on the diffusivity is shown in Figures 3.6, 3.7 and 3.8 respectively.

It can be seen in Figure 3.6 that the lateral diffusivity increases almost linearly with increasing windrow spacing. This is because for larger windrow spacings, more particles are released into each cell and on reaching the windrows form longer accumulations within them, as can be seen in Figure 3.3. At large windrow spacings, the observed decrease of the diffusivity away from the linear relationship can be explained by the bias introduced by using a finite number of particles, with the release of the particles stopping before the whole of the last Langmuir cell has been carried past the release point. This leads to the final windrow containing only a relatively small

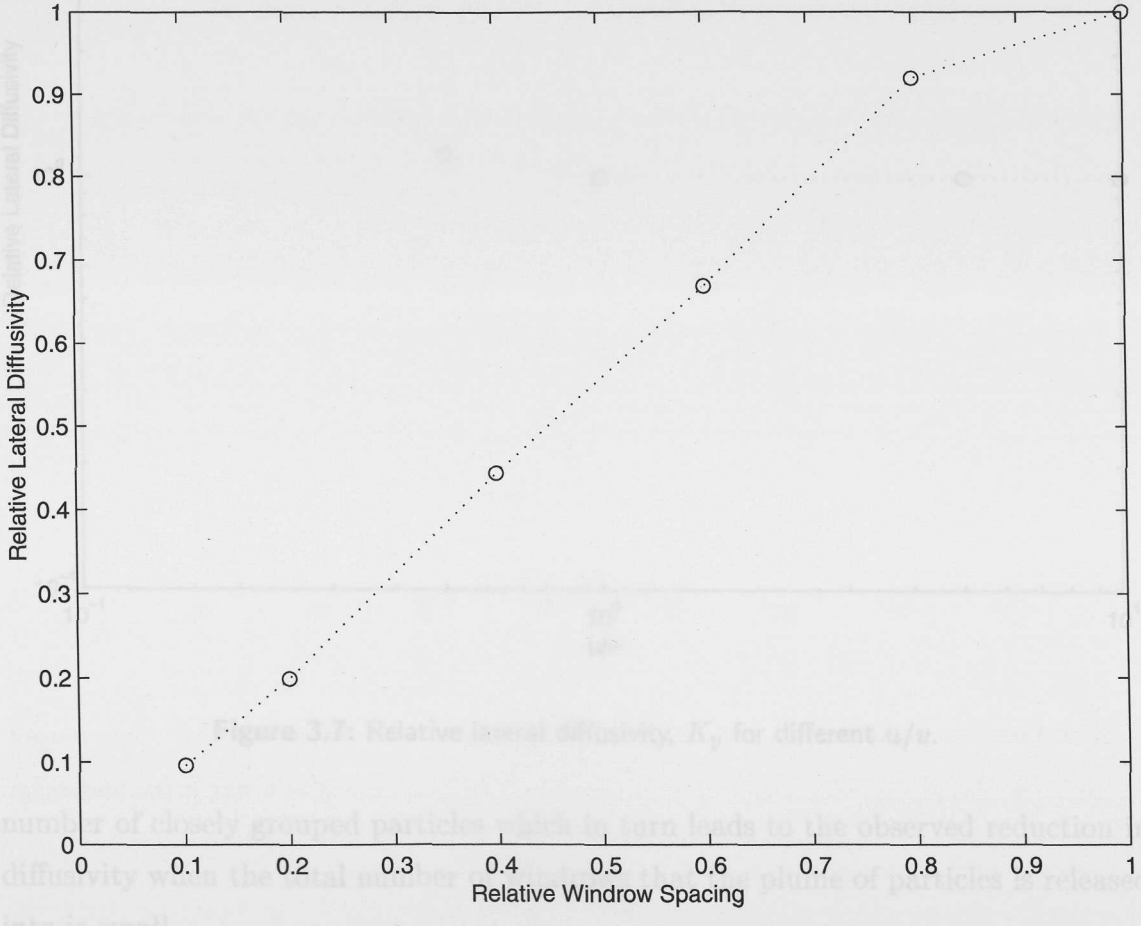

Figure 3.6: Relative lateral diffusivity, K_y, for different windrow spacings, L. K_y and L have been normalised by their maximum values and $u = v$.

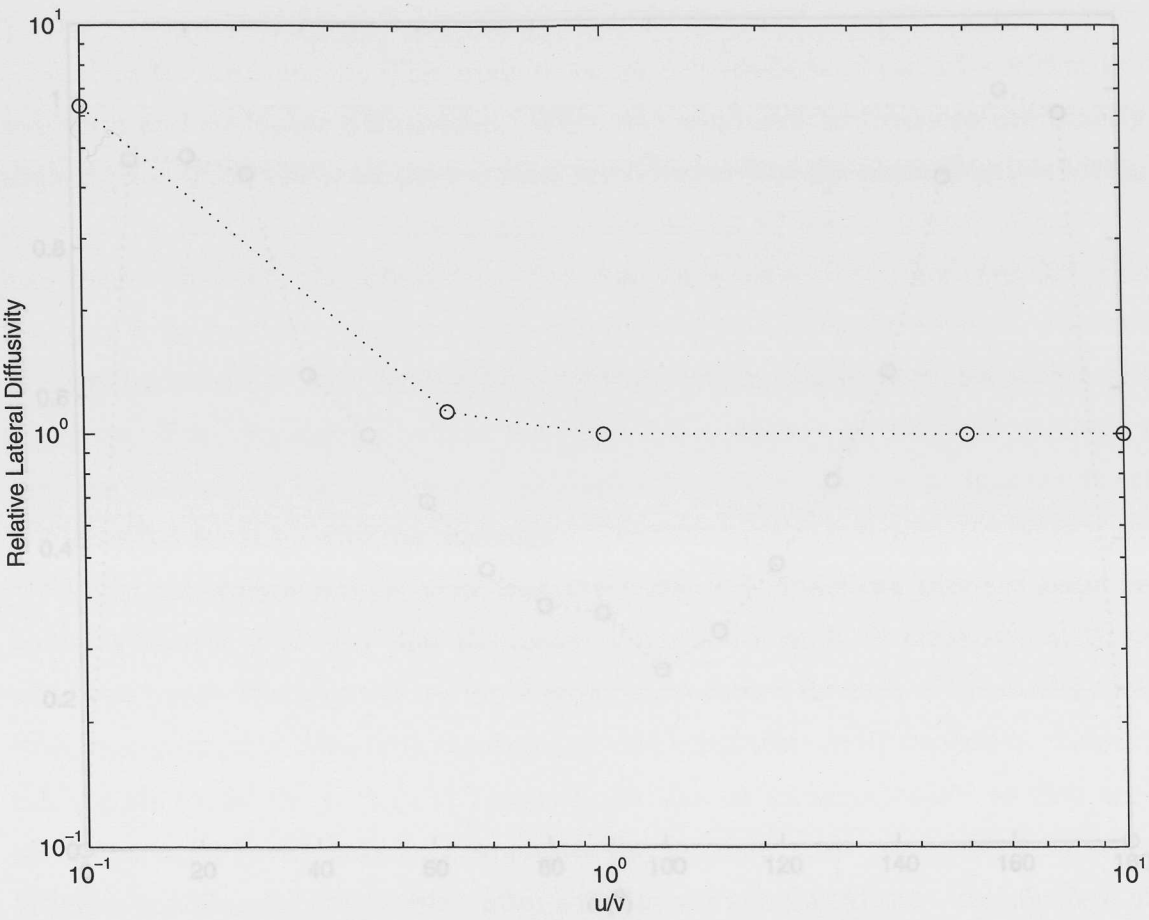

Figure 3.7: Relative lateral diffusivity, K_y for different u/v.

number of closely grouped particles which in turn leads to the observed reduction in diffusivity when the total number of windrows that the plume of particles is released into is small.

Figure 3.7 shows that the lateral diffusivity generally decreases with increasing u/v. This is because when $u/v < 1$ the particles are only being advected relatively slowly into the windrows, whilst the enhanced down-wind flow within the windrows is relatively large, leading to a widely distributed pattern of particles within the windrows. When $u/v > 1$, the particles are carried relatively quickly into the windrows, at which point their positions become stationary relative to one another.

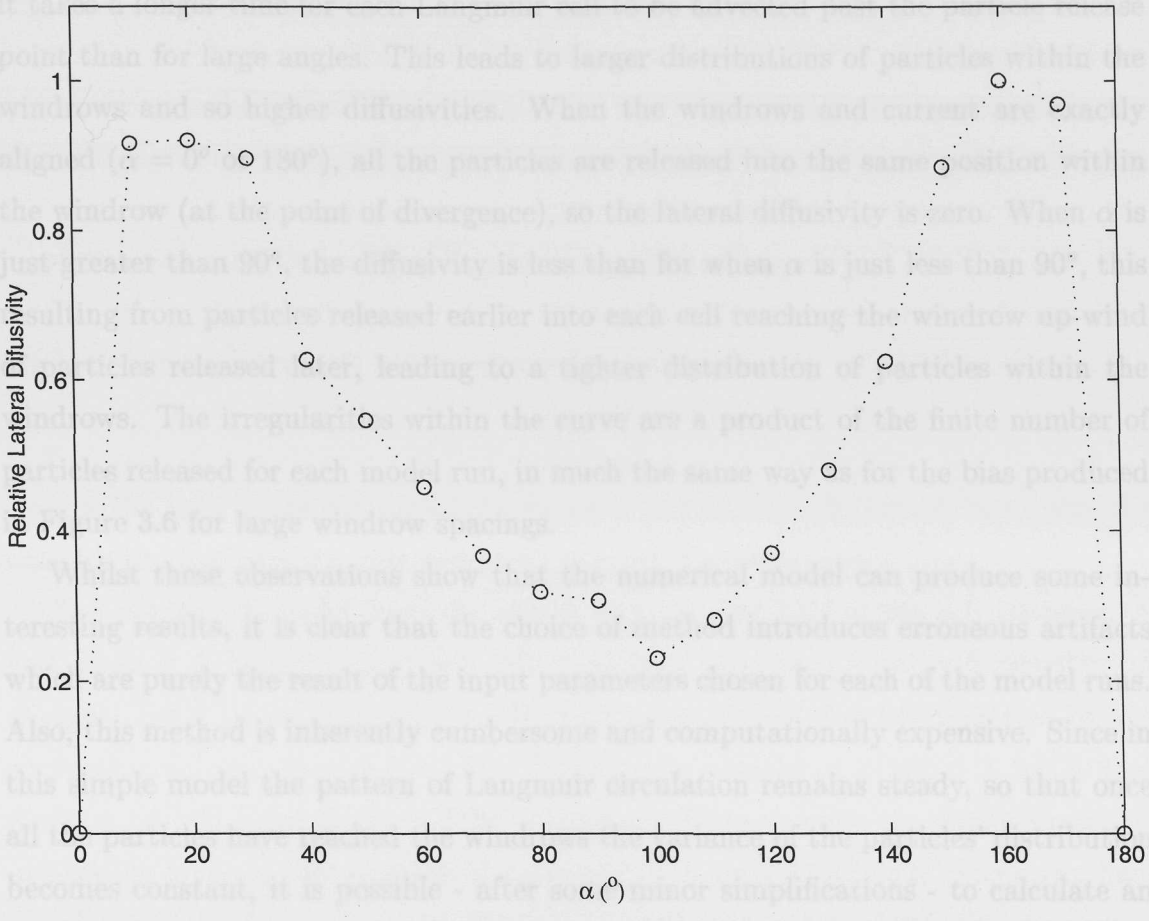

Figure 3.8: Relative lateral diffusivity, K_y, for different α. K_y has been normalised by its maximum value and $u = v$.

The more rapid the convergence of the particles into the windrows, the tighter the final distribution of particles within them. This can also be seen in the model runs shown in Figure 3.4.

Figure 3.8 shows how the lateral diffusivity varies with the angle between the wind (or the orientation of the windrows) and the steady current, U. It can be seen that the highest diffusivities occur when the windrow orientation is within 30° of the current (i.e. $\alpha \approx 30^o$ or $\alpha \approx 150^o$). The lateral diffusivity generally decreases for values of α close to 90°. For small angles between the wind and the mean current,

it takes a longer time for each Langmuir cell to be advected past the particle release point than for large angles. This leads to larger distributions of particles within the windrows and so higher diffusivities. When the windrows and current are exactly aligned ($\alpha = 0^o$ or 180^o), all the particles are released into the same position within the windrow (at the point of divergence), so the lateral diffusivity is zero. When α is just greater than 90^o, the diffusivity is less than for when α is just less than 90^o, this resulting from particles released earlier into each cell reaching the windrow up-wind of particles released later, leading to a tighter distribution of particles within the windrows. The irregularities within the curve are a product of the finite number of particles released for each model run, in much the same way as for the bias produced in Figure 3.6 for large windrow spacings.

Whilst these observations show that the numerical model can produce some interesting results, it is clear that the choice of method introduces erroneous artifacts which are purely the result of the input parameters chosen for each of the model runs. Also, this method is inherently cumbersome and computationally expensive. Since in this simple model the pattern of Langmuir circulation remains steady, so that once all the particles have reached the windrows the variance of the particles' distribution becomes constant, it is possible - after some minor simplifications - to calculate an analytical solution to the problem. This new method is both more elegant and efficient, allowing the lateral diffusivity to be calculated over a much wider range of input conditions. This analytical model and the results from it are discussed in the following section.

3.2 Analytical

The objective is to develop an analytical model to quantify and describe how Langmuir circulation produces dispersion in a steady tidal current, U. Components of the model are shown in Figure 3.9. Buoyant particles are released continuously from a fixed source into a Langmuir cell as it is advected past by a mean current. The Langmuir cell of width L, here defined as the region between two neighbouring divergent

regions, is aligned with the wind, W, at an angle, α, to the direction of the current. In a frame of reference moving with the mean current, the source of buoyant particles moves through the cell with a speed U. The first particle to be released is at A, the last at C, and that released directly into the convergence line, DD, is at B. On release the particles are supposed to converge towards DD at speed u, perpendicular to the wind direction, and on reaching it move downwind at a speed v.

The time, T_D, for all the particles released from the source between A and C to reach convergence line DD as it is advected past, is given by

$$T_D = \frac{L(2u + U\sin\alpha)}{2uU\sin\alpha}. \tag{3.3}$$

This is the time taken for the source to move across the cell from A to C plus the time for the last particle (released at C) to reach the convergence line.

The particles released from the source into the first half of the cell (between A and B) as it is advected past will, after reaching DD, have a uniform distribution along it. Let x be the distance from B of particles on DD after being carried by the converging currents for the time T_D. The particle released at position A has a final position on DD equal to $x_A = L(2v + U\cos\alpha)/2U\sin\alpha$, while the particle released at position B has a final position of $x_B = vL(u + U\sin\alpha)/2uU\sin\alpha$. The mean final position on DD of the group of particles released between A and B is $(x_A + x_B)/2$ or

$$\overline{x}_{AB} = \frac{L}{4}\left(\frac{3uv + vU\sin\alpha + uU\cos\alpha}{uU\sin\alpha}\right) \tag{3.4}$$

and its variance is

$$\sigma^2_{AB} = \frac{1}{12}(x_A - x_B)^2 = \frac{L^2}{48}\left(\frac{vu + uU\cos\alpha - vU\sin\alpha}{uU\sin\alpha}\right)^2 \tag{3.5}$$

Similarly the mean final position on DD of the particles released as the second half of the cell (BC) passes the source is

$$\overline{x}_{BC} = \frac{L}{4}\left(\frac{uv + vU\sin\alpha - uU\cos\alpha}{uU\sin\alpha}\right), \tag{3.6}$$

and its variance is

$$\sigma^2_{BC} = \frac{L^2}{48}\left(\frac{uv + vU\sin\alpha + uU\cos\alpha}{uU\sin\alpha}\right)^2. \tag{3.7}$$

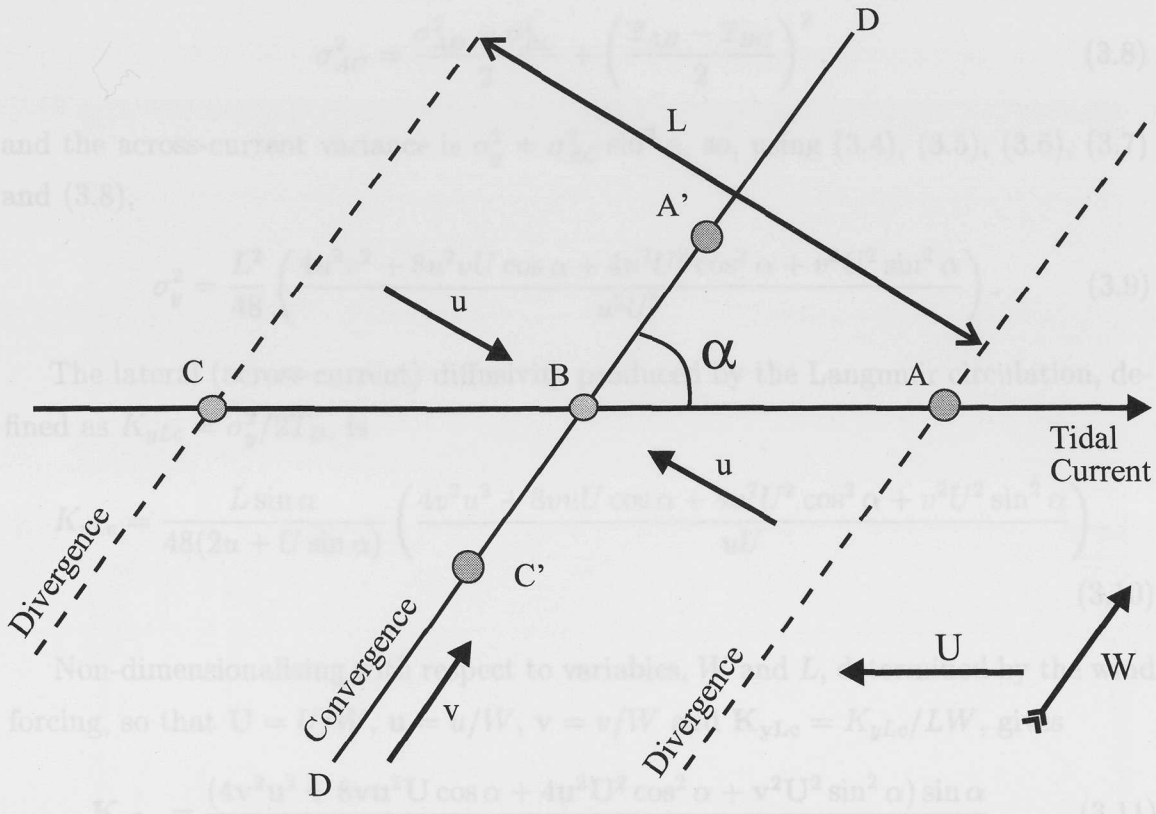

Figure 3.9: Components of the simple model of a windrow. The longitudinal axis of the Langmuir cell, the region between two neighbouring divergences, is aligned parallel to the wind, W, which is at an angle, α, to the left of the mean current. This mean current advects a stable Langmuir cell, of width L, past a fixed continuous source of buoyant particles. Adopting a frame of reference which moves with the Langmuir cell, the fixed source passes through the cell with a speed U, with the first particle released at position A, and the last at position C. Position B marks the location of the particle released directly into the line of convergence DD. On release, the particles are carried towards DD by the converging current, u, and on reaching it are carried in a down-wind direction, v. The converging current, u, acts perpendicular to the wind direction, so that the particles released at A and C initially reach DD at A' and C' respectively.

The variance of the total distribution of particles in the windrow is

$$\sigma_{AC}^2 = \frac{\sigma_{AB}^2 + \sigma_{BC}^2}{2} + \left(\frac{\overline{x}_{AB} - \overline{x}_{BC}}{2}\right)^2, \tag{3.8}$$

and the across-current variance is $\sigma_y^2 = \sigma_{AC}^2 \sin^2\alpha$, so, using (3.4), (3.5), (3.6), (3.7) and (3.8),

$$\sigma_y^2 = \frac{L^2}{48}\left(\frac{4u^2v^2 + 8u^2vU\cos\alpha + 4u^2U^2\cos^2\alpha + v^2U^2\sin^2\alpha}{u^2U^2}\right). \tag{3.9}$$

The lateral (across-current) diffusivity produced by the Langmuir circulation, defined as $K_{yLc} = \sigma_y^2/2T_D$, is

$$K_{yLc} = \frac{L\sin\alpha}{48(2u + U\sin\alpha)}\left(\frac{4v^2u^2 + 8vuU\cos\alpha + 4u^2U^2\cos^2\alpha + v^2U^2\sin^2\alpha}{uU}\right). \tag{3.10}$$

Non-dimensionalising with respect to variables, W and L, determined by the wind forcing, so that $\mathbf{U} = U/W$, $\mathbf{u} = u/W$, $\mathbf{v} = v/W$ and $\mathbf{K_{yLc}} = K_{yLc}/LW$, gives

$$\mathbf{K_{yLc}} = \frac{(4\mathbf{v}^2\mathbf{u}^2 + 8\mathbf{v}\mathbf{u}^2\mathbf{U}\cos\alpha + 4\mathbf{u}^2\mathbf{U}^2\cos^2\alpha + \mathbf{v}^2\mathbf{U}^2\sin^2\alpha)\sin\alpha}{48\mathbf{u}\mathbf{U}(2\mathbf{u} + \mathbf{U}\sin\alpha)}. \tag{3.11}$$

If $\mathbf{u}$ and $\mathbf{v}$ are constants (i.e. u and v are constant fractions of the wind speed, W) then it follows that $\mathbf{K_{yLc}}$ =f($\mathbf{U}, \alpha$).

This model of the dispersion is valid only when all the particles released into the Langmuir cell have sufficient time to reach DD before it breaks up or when $T_D \leq T_*$, where T_* is the typical lifetime of the Langmuir cell. L scales with W [$L = (4.8\text{ s}) \times W$, Faller and Woodcock, 1964] and $\mathbf{u} = \mathbf{v} = 0.03$ [Filatov et al., 1981]. Values of c are selected so that T_* falls within the range reported by Thorpe [1992] from observations (see Section 2.1) so that $T_* = 10$ min, $c = 3.75$ to $T_* = 30$ min, $c = 11.25$. Contours of $\mathbf{K_{yLc}}$ plotted against $\mathbf{U}^{-1} = W/U$ and α are shown in Figure 3.10, along with lines of $T_D = T_*$ for three different values of c.

The region of validity of Figure 3.10 ranges from $1 \leq W/U \leq 100$ (e.g. from $W = U = 1$ ms^{-1}, or $\mathbf{U} = 1$, to $W = 10$ ms^{-1}, $U = 0.1$ ms^{-1}, $\mathbf{U} = 0.01$). When

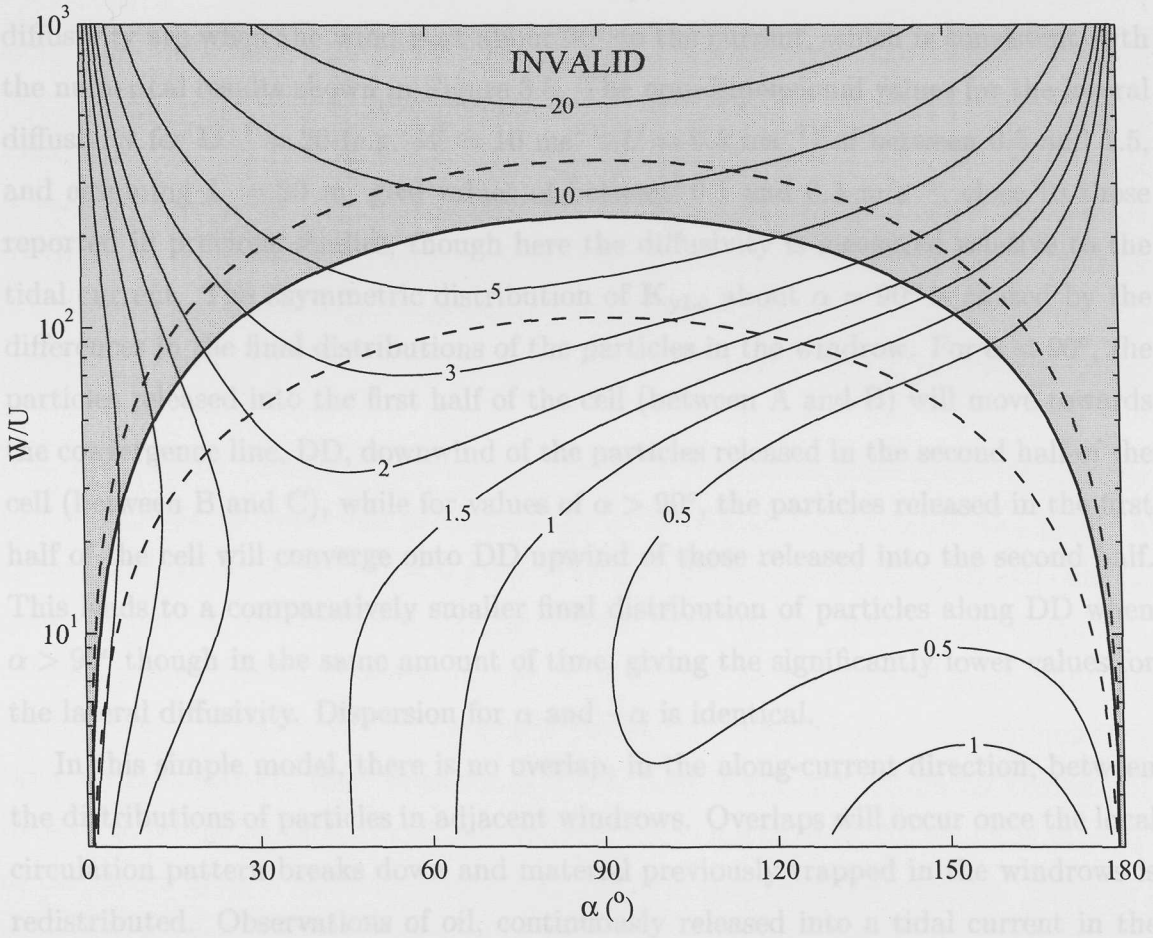

Figure 3.10: Contours of $\mathbf{K_{yLc}}(\times 10^{-3})$ - see Equation 3.11 - plotted against $\mathbf{U}^{-1} = W/U$ and α. The thick solid line and the two dashed lines indicate the maximum values of W/U for which the model is valid ($T_D = T_*$). The value of $c = 7.5$ ($T_* = 20$ min) has been used for the solid line, which gives the lower bound to the invalid shaded region, while the lower and upper dashed lines use values of $c = 3.75$ and $c = 11.25$ respectively, to provide a measure of uncertainty.

the wind is very strong relative to the tidal current, $\mathbf{U}^{-1} \gg 1$, the highest lateral diffusivities are when the wind and current are close to perpendicular. However, when the ratio of wind to tide is close to unity, the maximum values for the lateral diffusivity are when the wind is at about 30^o to the current, which is consistent with the numerical results shown in Figure 3.8. The non-dimensional values for the lateral diffusivity for $\mathbf{U}^{-1} = 20$ (e.g. $W = 10$ ms^{-1}, $U = 0.5$ ms^{-1}) of between 0.5 and 1.5, and assuming $L = 20$ m, give values of between 0.1 and 0.3 m^{2}s^{-1}, close to those reported in previous studies, though here the diffusivity is measured relative to the tidal current. The asymmetric distribution of $\mathbf{K_{yLc}}$ about $\alpha = 90^o$ is caused by the differences in the final distributions of the particles in the windrow. For $\alpha < 90^o$, the particles released into the first half of the cell (between A and B) will move towards the convergence line, DD, downwind of the particles released in the second half of the cell (between B and C), while for values of $\alpha > 90^o$, the particles released in the first half of the cell will converge onto DD upwind of those released into the second half. This leads to a comparatively smaller final distribution of particles along DD when $\alpha > 90^o$ though in the same amount of time, giving the significantly lower values for the lateral diffusivity. Dispersion for α and $-\alpha$ is identical.

In this simple model, there is no overlap, in the along-current direction, between the distributions of particles in adjacent windrows. Overlaps will occur once the local circulation pattern breaks down and material previously trapped in the windrows is redistributed. Observations of oil, continuously released into a tidal current in the presence of Langmuir circulation [e.g. Figure 4, Thorpe, 1995b] are consistent with this; there is little overlapping in the distributions of material in adjacent windrows, at least in the early stages of dispersion.

It is assumed here that the cells are stable and steady (i.e. with uniform current components). The region of invalidity is that for which particles do not reach the convergence line before the cells break-up. Instability of the cells may lead however to even greater rates of lateral dispersion as buoyant material is passed between neighbouring cells, particularly at values of α near 0^o or 180^o.

3.3 Relative importance of Langmuir circulation and tidal current

Adopting the parameterisation for the horizontal diffusion coefficient of Bowden [1965] (see Section 2.3), the ratio of the lateral dispersion caused by Langmuir circulation to that produced by the tidal current alone is given by $K_{yLc}/K_{yT} = (LW/\beta UH)\mathbf{K_{yLc}}$. A value of 0.4 is taken for L/H, the middle of the range taken from the observations by Graham and Hall [1997], while a value of 0.025 is used for β [Fischer, 1973]. Figure 3.11 shows contours of K_{yLc}/K_{yT} plotted against $\mathbf{U}^{-1}$ and α.

Figure 3.11 shows the importance of Langmuir circulation in the lateral dispersion of buoyant material relative to that caused by a tidal current alone. When $\mathbf{U}^{-1} > 40$ (e.g. $W = 10\ \mathrm{ms}^{-1}$ and $U = 0.25\ \mathrm{ms}^{-1}$), Langmuir circulation plays a more than equal role in the lateral dispersion of buoyant material. As $\mathbf{U}^{-1}$ approaches and passes a value of 10^2 ($W = 10\ \mathrm{ms}^{-1}$, $U = 0.1\ \mathrm{ms}^{-1}$) and at angles between the wind and current greater than 30^o, the effects of Langmuir circulation become increasingly dominant, exceeding the dispersion caused by the tidal current by an order of magnitude. In reality, the dominance of the Langmuir circulation may be yet more pronounced since a conservatively large estimate of β was used in the calculation for the lateral dispersion produced by the tide. The value of c selected to limit the region of validity of the model gives a realistic value for T_* and is in line with observations. However, even if T_* is less than this (indicated by the lower of the two dashed lines and below), the effect of Langmuir circulation on the lateral diffusivity will still be very important.

3.4 Conclusions

The numerical simulations have shown the patterns of dispersion of a plume of buoyant particles under the combined influence of a steady array of Langmuir cells and a mean current. The plume of material initially meanders, and then forms distinct windrows. The time for this to happen depends upon the angle between the wind

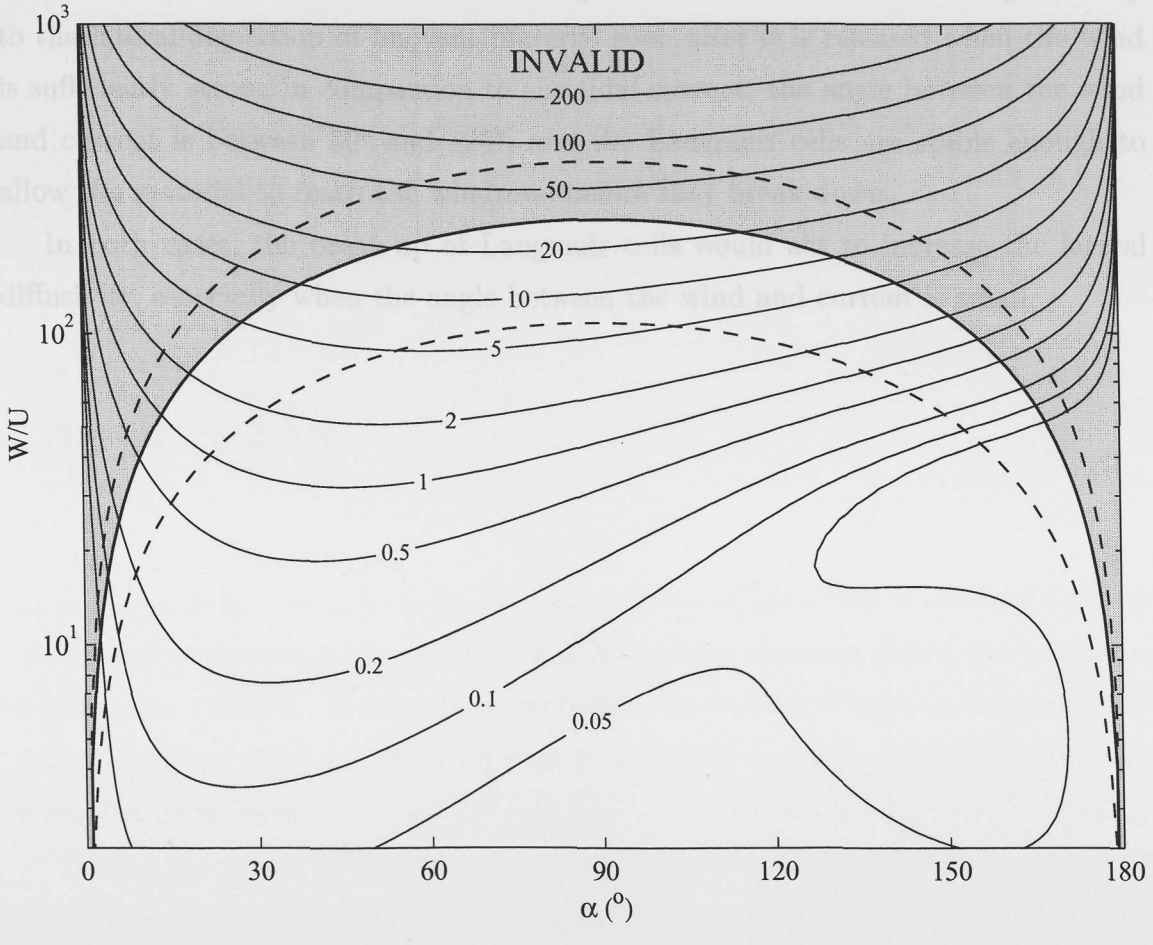

Figure 3.11: Contours of K_{yLc}/K_{yT} plotted against $\mathbf{U}^{-1} = W/U$ and α. The thick solid line and the two dashed lines are as for Figure 3.10.

and the current, the spacing between the windrows and the strength of the converging currents. The lateral diffusivity is found to be greatest for large windrow spacings, at angles between the wind and current of about 30^o, and when the enhanced down-wind flow within the windrows in large relative to the converging currents.

The analytical method shows that Langmuir circulation contributes significantly to the lateral dispersion of buoyant material soon after it is released when the wind is sufficiently strong in comparison to the tidal current, the angle between the wind and current is between 30^o and 120^o, and the Langmuir cells are stable enough to allow the material to reach the windrows before they break down.

In both cases, the break-up of Langmuir cells would act to increase the lateral diffusivity, especially when the angle between the wind and current is small.

Chapter 4

Observations of the surface structure of bottom-generated turbulence

As reviewed in Section 2.2, 'boils' - circular regions of upwelling at the water surface - are a well documented feature of flows in laboratory channels, rivers and in narrow, tidal straits. However, there were no reported observations of boils in the open, well-mixed sea until those of Nimmo Smith et al. [1999] (see Appendix C). These are expanded upon below.

During the spring and summer months of 1991 and 1992, a series of experiments were carried out in a tidally well-mixed, and consequently unstratified, region of the southern North Sea [Simpson, 1981], designed to investigate mixing processes at the sea surface. The experimental site was about 56 km off the English coast (Figure 4.1), with a water depth of about 45 m, in a region where the sea bed is flat, with no dunes or other notable bed forms. Here the tides are mainly semi-diurnal and strongly rectilinear [Elliott, 1986, and shown in Figure 4.2], and the maximum currents exceed 1 $m\ s^{-1}$. Tidal currents were measured using two vector averaging current meters deployed on a mooring at approximately 1/3 and 2/3 depth. For some deployments,

the current meter measurements were augmented by the addition of an electromagnetic vector averaging current meter deployed 1 m below the surface and an acoustic doppler current profiler (ADCP), capable of measuring current profiles down to 25 m depth. Winds were measured from the support vessel by a masthead anemometer and wind vane, while waves were monitored by a waverider buoy. A diagram showing the equipment deployed is displayed in Figure 4.3. The principal components of the experiments were the release of rhodamine dye and diesel oil in continuous plumes from a moored source at the sea surface, to measure horizontal and vertical diffusivities, and the deployment of a side-scan sonar rig, to visualise the small-scale near-surface mixing processes. The results from the dye releases have been reported by Morales et al. [1997] and are reviewed in Section 2.3.2. The side-scan sonar images (sonographs) reveal periods where wind-generated processes, such as Langmuir circulation (see Section 2.1), dominate and other periods where tidally generated turbulence becomes predominant. It is these latter periods which are presented in the subsequent section, while aerial video images of the diesel plume and surrounding water surface from a co-incidental period as well as Compact Airborne Spectrographic Imager (CASI) images from a more recent experiment, are given in Section 4.2. Observations from the ADCP and current meters are described in Section 4.3, while Section 4.4 is a discussion on the intermittency and scaling of the observed features.

4.1 Side-scan sonar

A pulsed, two-beam side-scan sonar system was mounted on a frame set on the sea bed. The sonars operate at 80 kHz and 90 kHz, are set 90^o apart in the horizontal, and produce vertical fan-like beams with axes aligned upwards, 20^o from the horizontal. The rig was aligned such that on deployment the 80 kHz sonar was directed as closely as possible into the tidal current, with the 90 kHz sonar directed across the flow (see Figure 4.3). A more detailed description of the sonar rig used is given by Graham and Hall [1997].

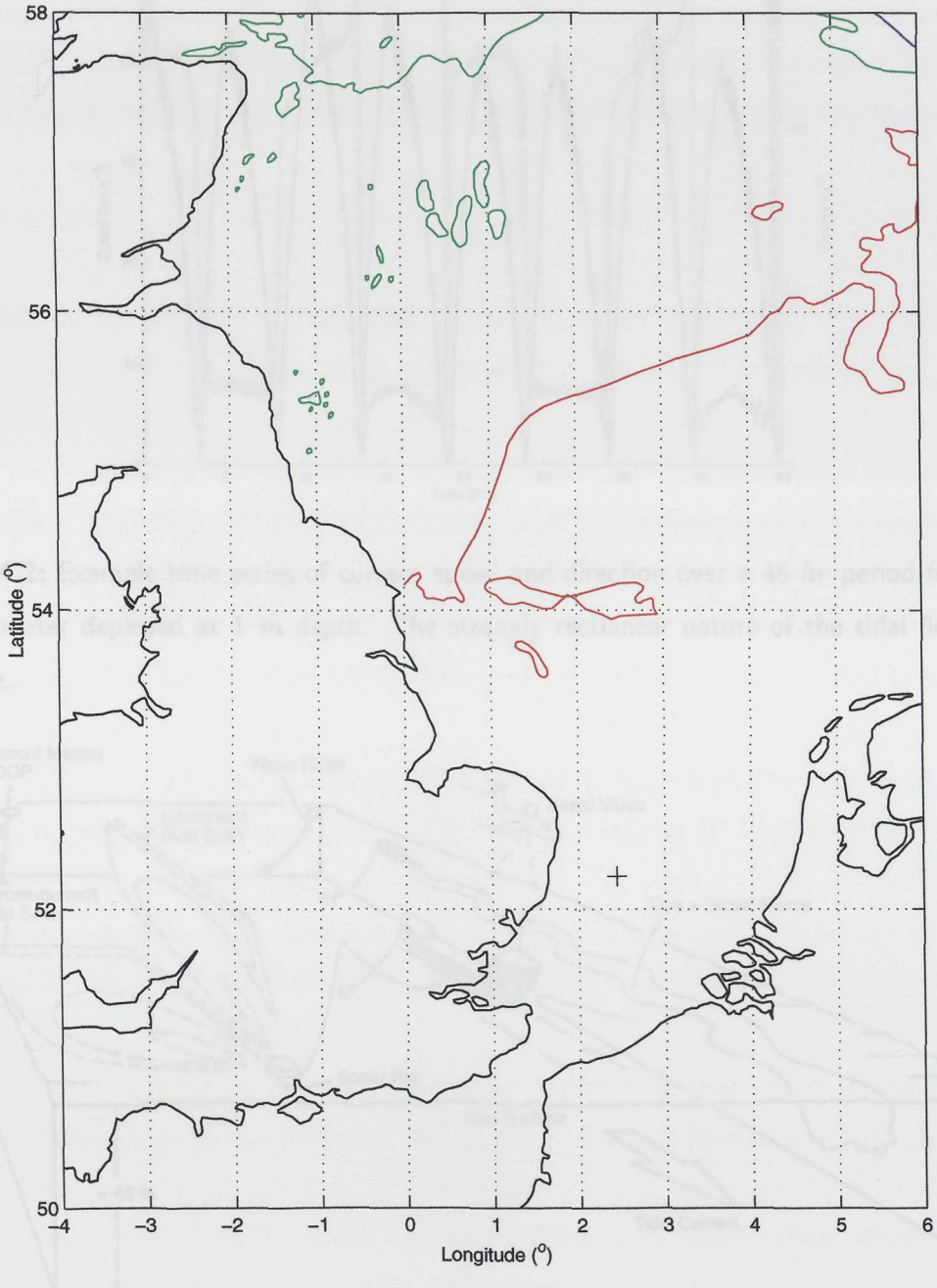

Figure 4.1: Location of the North Sea Experiments (+). The 50 m and 100 m depth contours are shown in red and green respectively.

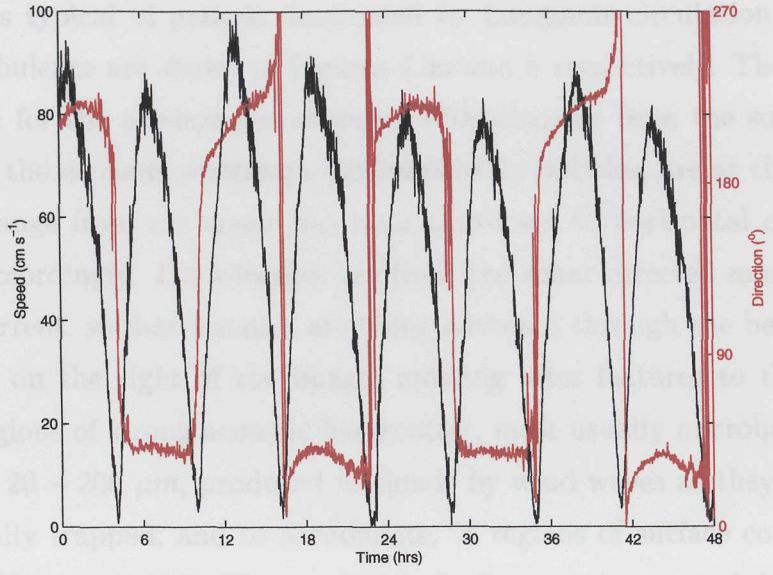

Figure 4.2: Example time series of current speed and direction over a 48 hr period from the current meter deployed at 1 m depth. The strongly rectilinear nature of the tidal flow is in evidence.

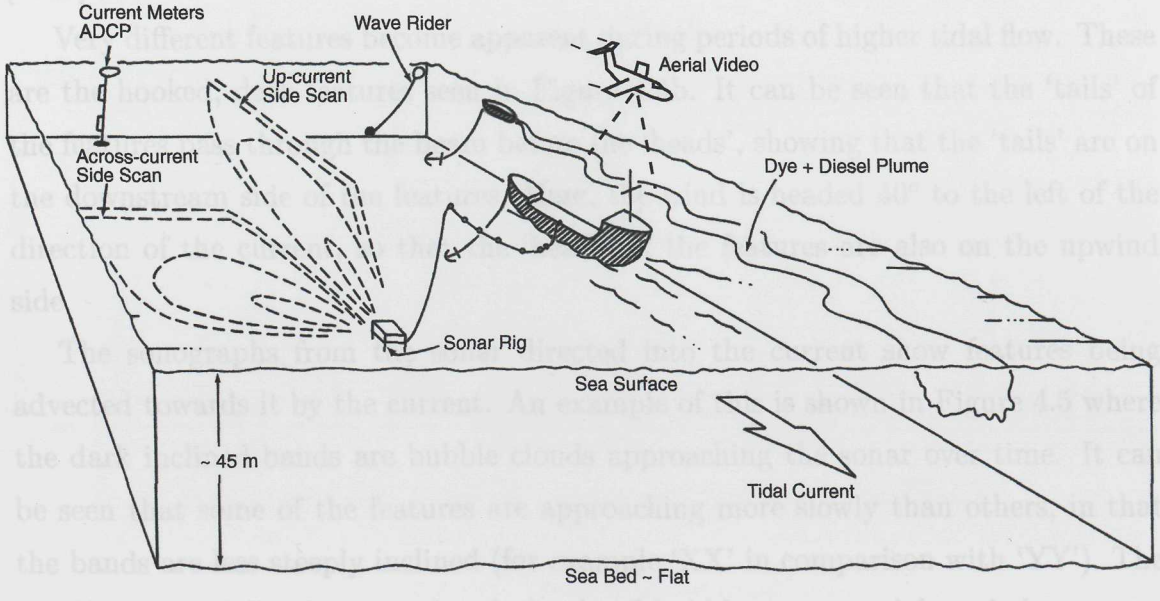

Figure 4.3: Diagram showing the equipment deployed during the North Sea Experiments [adapted from Thorpe et al., 1996].

Sonographs typical of periods dominated by Langmuir circulation and bottom-generated turbulence are shown in Figures 4.4a and b respectively. The images have been adjusted for the attenuation of sound with distance from the sonar, and it is assumed that the acoustic scatterers, predominantly bubbles, are at the sea surface, so that the range from the sonar has been converted to horizontal distance along the surface accordingly. Both images are from the sonar directed more or less normal to the current, so that features are being advected through the beam over time, with features on the right of the images crossing after features to the left. Dark shades are regions of strong acoustic backscatter, most usually microbubbles, of typical diameter $20 - 200\ \mu m$, produced in clouds by wind waves as they break. These can be partially trapped, and so accumulate, in regions of surface convergence and downwelling [Stommel, 1949, Thorpe, 1984]. Such convergences and downwelling are found between alternate neighbouring Langmuir cells, leading to the formation of the fine, regular bands seen in Figure 4.4a and previously documented by, among others, Farmer and Li [1995], Thorpe [1984], Thorpe and Hall [1983] and Graham and Hall [1997].

Very different features become apparent during periods of higher tidal flow. These are the hooked, dark features seen in Figure 4.4b. It can be seen that the 'tails' of the features pass through the beam before the 'heads', showing that the 'tails' are on the downstream side of the features. Here, the wind is headed 40^o to the left of the direction of the current, so that the 'heads' of the features are also on the upwind side.

The sonographs from the sonar directed into the current show features being advected towards it by the current. An example of this is shown in Figure 4.5 where the dark inclined bands are bubble clouds approaching the sonar over time. It can be seen that some of the features are approaching more slowly than others, in that the bands are less steeply inclined (for example 'XX' in comparison with 'YY'). The steeply inclined bands are isolated clouds of bubbles generated by wind waves as they break, moving with the wind drift and tidal current in the upper 1 m of the water column [Thorpe, 1982, Thorpe and Hall, 1983, Thorpe et al., 1998]. Over

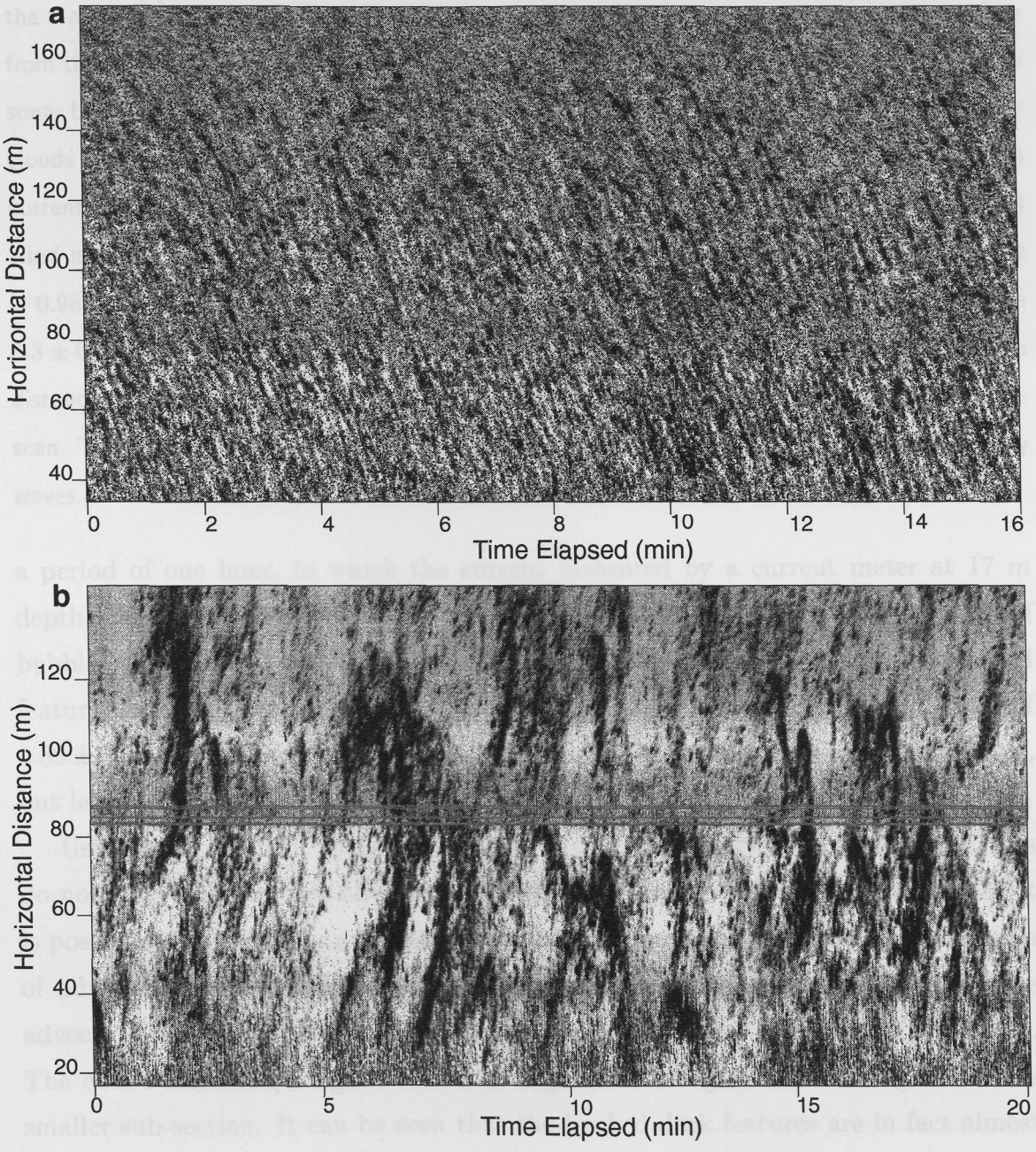
a
160
140
120
100
80
60
40
Horizontal Distance (m)
0
2
4
6
8
10
12
14
16
Time Elapsed (min)
b
120
100
80
60
40
20
Horizontal Distance (m)
0
5
10
15
20
Time Elapsed (min)

Figure 4.4: (previous page) Side-scan sonar images from the across-current sonar, characteristic of periods dominated by **a** Langmuir circulation and **b** tidally generated boils. In both images, the x-axes are elapsed time in minutes and the y-axes are horizontal distance along the surface from the sonar rig in metres. This means that the images show features being carried across the sonar beam by the current. Dark shades are areas of high acoustic backscatter, most commonly clouds of bubbles trapped in regions of surface convergence and downwelling. **a** The (1 m) current is 0.80 ± 0.16 $m\ s^{-1}$ headed 84 ± 3^o to the left of the sonar beam and the (10 m) wind is 6.4 ± 0.8 $m\ s^{-1}$ headed 13 ± 8^o to the right of the current. **b** The (17 m) current is 0.98 ± 0.03 $m\ s^{-1}$ headed 74 ± 1^o to the left of the sonar beam and the (10 m) wind is 6.3 ± 0.5 $m\ s^{-1}$ headed 43 ± 7^o to the left of the current. The bands of noise at about 85 m distance are caused by interference from a sonar operating at 8 Hz, twice the rate of this side-scan. The fine vertical bands at the lower edge of the image are reflections from surface gravity waves.

a period of one hour, in which the current measured by a current meter at 17 m depth changed by less than 0.1 $m\ s^{-1}$, the mean speed of these isolated clouds of bubbles is 1.29 ± 0.08 $m\ s^{-1}$. The slower moving bands are most probably the hooked features seen in Figure 4.4b. Over the same period, they have a mean speed of 0.89 ± 0.09 $m\ s^{-1}$, greater than that of the tidal current at 33 m (0.75 ± 0.02 $m\ s^{-1}$), but less than that at 17 m (0.98 ± 0.03 $m\ s^{-1}$) and of the isolated clouds.

Using a 'frozen field' approximation, by making the assumption that the features do not evolve as they are advected through the beam (although see Section 4.4), it is possible to correct the sonograph shown in Figure 4.4b for the speed and direction of advection of the features through the sonar beam by multiplying time by the advection speed of the features as measured in the sonar directed into the current. The entire corrected image is shown in Figure 4.6 along with an enlargement of a smaller sub-section. It can be seen that the hooked dark features are in fact almost semi-circular arcs (for example at 'W'), with a well-defined upstream edge. They have a mean diameter of 42 ± 10 m or $(0.93 \pm 0.22)H$, where H is the water depth. The

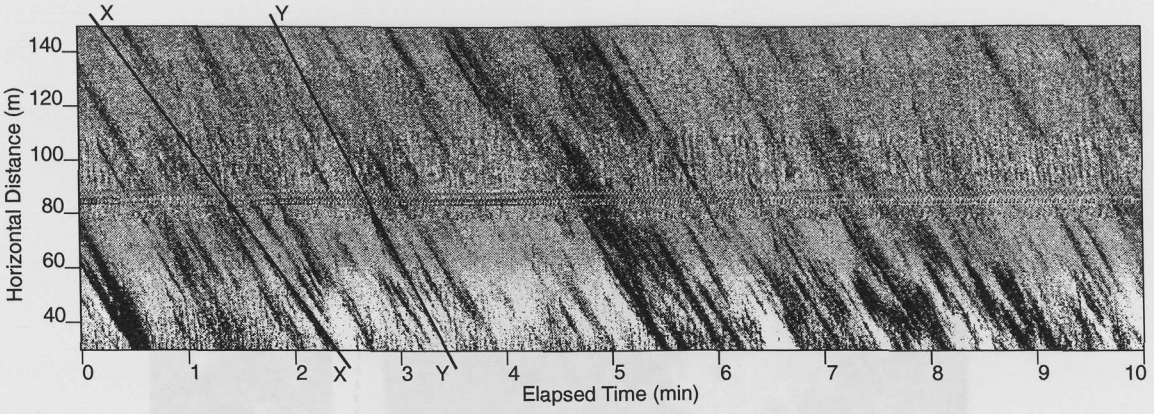

Figure 4.5: Sonograph from the sonar directed into the current for a period close to that shown in Figure 4.4b. The x and y axes are elapsed time in minutes and horizontal distance from the rig respectively. Dark shades are regions of high acoustic backscatter. It can be seen that these are approaching the sonar over time. Some of the features, for example 'XX', are being advected towards the sonar slower than others, for instance 'YY'. Again, the horizontal bands at 85 m are interference from another sonar.

mean number of features with centres passing through unit length of the sonar beam in unit time is $N = (9.4 \pm 3.3) \times 10^{-5}\ m^{-1}\ s^{-1}$. Fine-scale wind-aligned filaments can be seen within the radius of the arcs (for example at 'Z'), these possibly formed by small scale Langmuir cells, evolving within the region of surface disturbance.

Sonographs from periods of different relative orientation between the wind and tidal current are shown in Figure 4.7. In about 90% of cases, the strongest acoustic scattering is greatest on the side from which the relative wind-drift comes. Figure 4.7c shows this most clearly, as here the direction of the near-surface (1 m) current is also shown. It is this relative drift between the features and the surrounding surface waters that leads to the surface convergence and downwelling along the up-wind-drift edge, resulting in the local accumulation of bubbles and wave steepening [Longuet-Higgins, 1996] or even augmented breaking with bubble production, making the features detectable by the sonars. Again, the fine-scale wind-aligned bands are visible with the radius of the features.

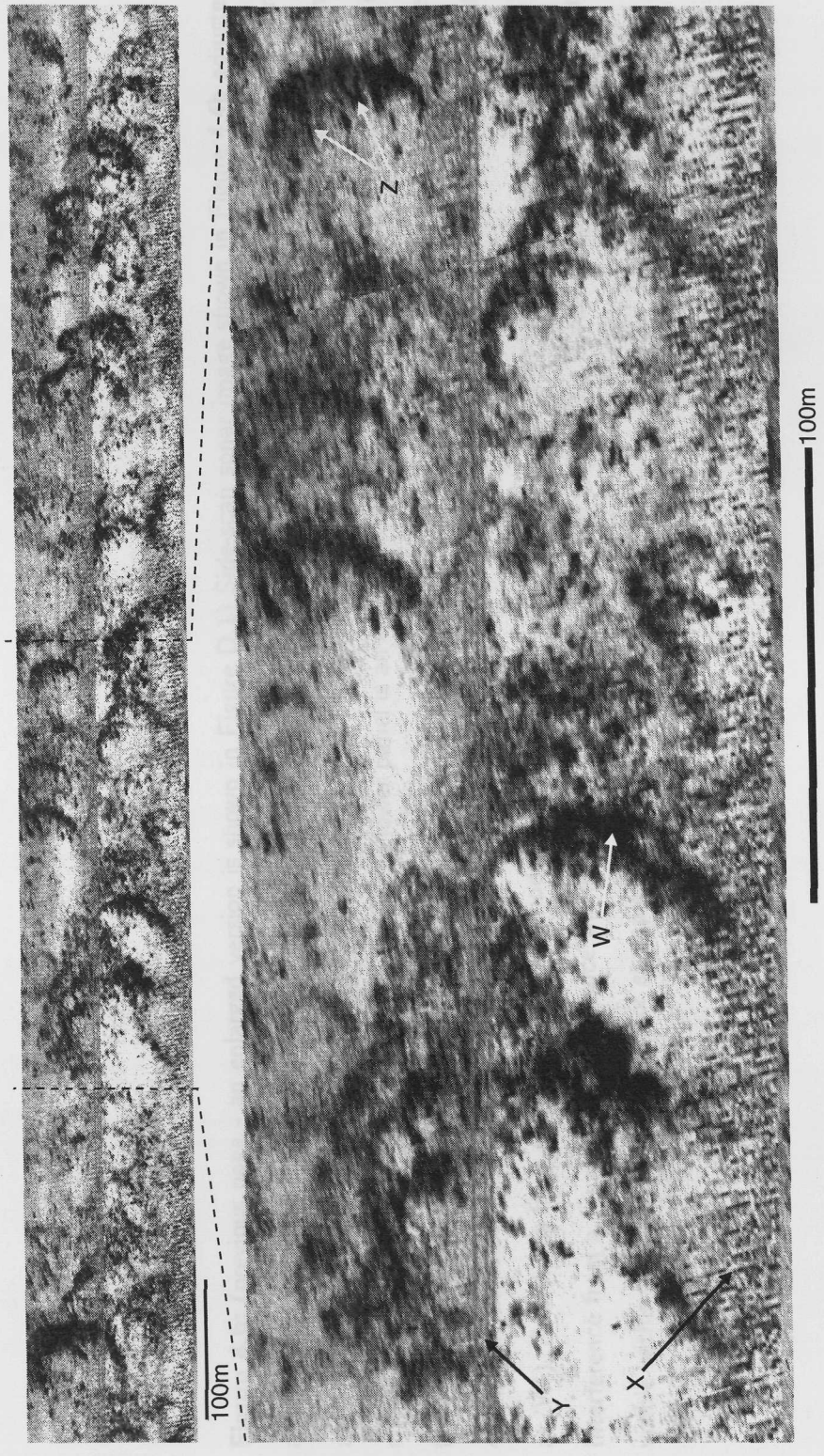
Z
W
X
Y
100m
100m

Figure 4.6: (previous page - an enlarged version is shown in Figure D.1) Side-scan sonar image shown in Figure 4.4b adjusted according to the advection speed and direction of the dark hooked features, $0.89\ m\ s^{-1}$ at 74^o to the left of the sonar beam, as measured by the sonar directed into the current and a current meter at $17\ m$ depth respectively. The upper panel shows the entire $20\ min$ period shown in Figure 4.4b, while the lower panel is an enlarged view of a $6\ min$ sub-section. The tidal current is from right to left, flowing at $0.98 \pm 0.03\ m\ s^{-1}$ at $17\ m$ and $0.75 \pm 0.02\ m\ s^{-1}$ at $33\ m$. The wind at $10\ m$ is $6.3\ m\ s^{-1}$, headed 43^o left of the current. It can be seen that after the correction, the dark hooked features take the form of arcs (for example at 'W'). Reflections from surface waves, of period $3.4\ s$ and height $0.4\ m$, are visible along the lower edge of the images ('X'). Interference from a sonar sampling at twice the frequency produces the horizontal bands, 'Y'. Wind-aligned fine-scale bands are visible within the radius of the arcs (for example at 'Z').

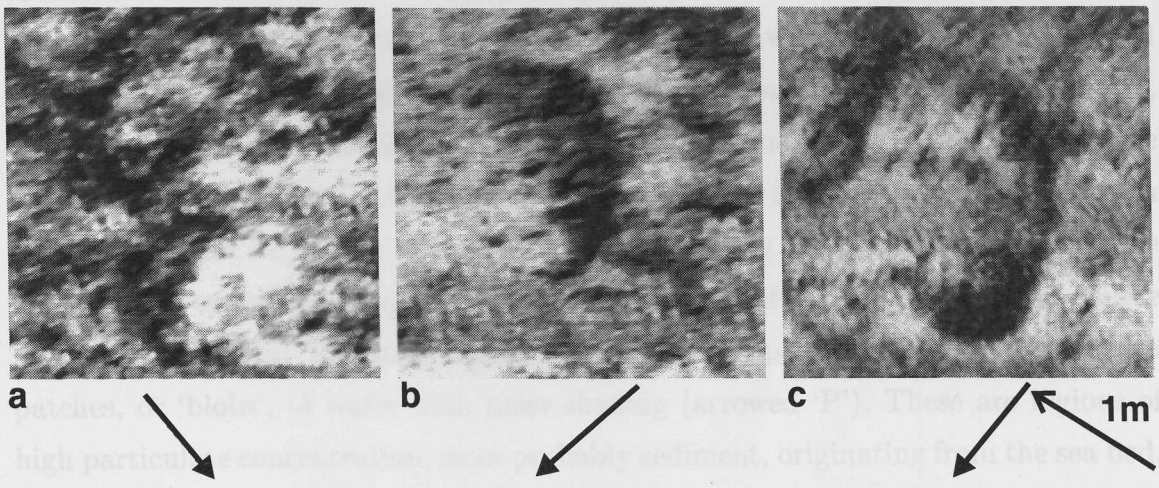

Figure 4.7: Sonograph images of strongly-scattering features (dark) in winds of different directions. The features are represented using the same frozen-field technique used in the preparation of Figure 4.6. In each image the tidal current is from right to left and the wind direction is shown by an arrow. Each image shows an area 60 m square. The mean current and (10 m) wind speed are, respectively, **a**, 0.60 $m\ s^{-1}$ (at 19 m depth), 3.0 $m\ s^{-1}$ **b**, 0.98 $m\ s^{-1}$ (at 17 m depth), 6.3 $m\ s^{-1}$, **c**, 0.80 $m\ s^{-1}$ (at 15 m depth), 7.1 $m\ s^{-1}$. In **c**, the open-headed arrow shows the direction of the 1 m current (1.04 $m\ s^{-1}$).

4.2 Aerial video and CASI

One hour prior to when the sonograph shown in Figure 4.4b was obtained, an aircraft equipped with a vertically downward looking video camera overflew the plume of diesel oil being continuously released onto the sea surface. The aircraft followed the length of the plume up to a distance of about 2 km downstream of the moored source, it then circled back to retrace the plume at about 5 min intervals for a total of five overflights. Frames were 'grabbed' in black and white from the video, scaled according to the aircraft's altitude and the size of a 12 m sampling boat within view, contrast-stretched to enhance the definition and then matched together to form the continuous composite images shown in Figure 4.8. The moored source is arrowed in each. The diesel oil, which appears as the pale, mostly continuous filament for the length of the composite images, forms a plume as it is advected away from the source by the tidal current. The surrounding water surface appears dark, interspersed with patches, or 'blobs', of water with paler shading (arrowed 'P'). These are regions of high particulate concentration, most probably sediment, originating from the sea bed. It can be seen that the diesel oil plume interacts with these blobs, being disrupted and displaced by them. Time sequences of these interactions are shown in detail in Figures 4.9 and 4.10, while the evolution an isolated sediment patch is shown in Figure 4.11. Full descriptions of the evolution of the features are given in the extended figure captions which accompany the images.

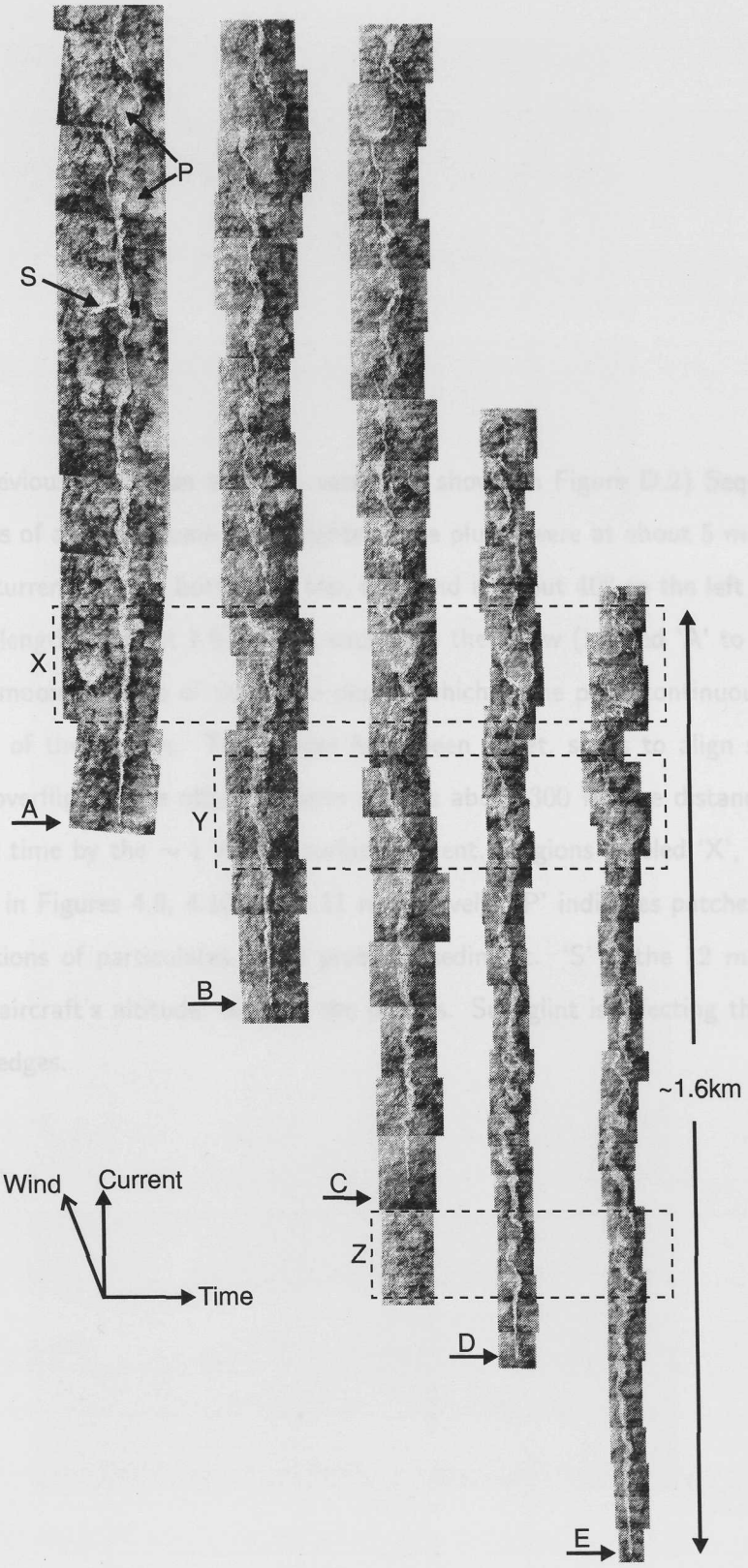
P
S
X
A
Y
B
~1.6km
Wind
Current
Time
C
Z
D
E

Figure 4.8: (previous page - an enlarged version is shown in Figure D.2) Sequence of aerial video composites of a diesel plume. Overflights of the plume were at about 5 min intervals. In each, the tidal current is from bottom to top, the wind is about 40^o to the left of the current, and the overall length is about 1.6 km. In each case the arrow (labeled 'A' to 'E') marks the location of the moored source of the diesel plume, which is the pale, continuous streak which runs the length of the images. The images have been offset, so as to align similar features in consecutive overflights; the offset between each is about 300 m, the distance the plume is advected in the time by the $\sim 1\ m\ s^{-1}$ surface current. Regions labeled 'X', 'Y' and 'Z' are shown in detail in Figures 4.9, 4.10 and 4.11 respectively. 'P' indicates patches of water with high concentrations of particulates, most probably sediment. 'S' is the 12 m sampling boat used, with the aircraft's altitude, to scale the images. Sun glint is affecting the images along their left-hand edges.

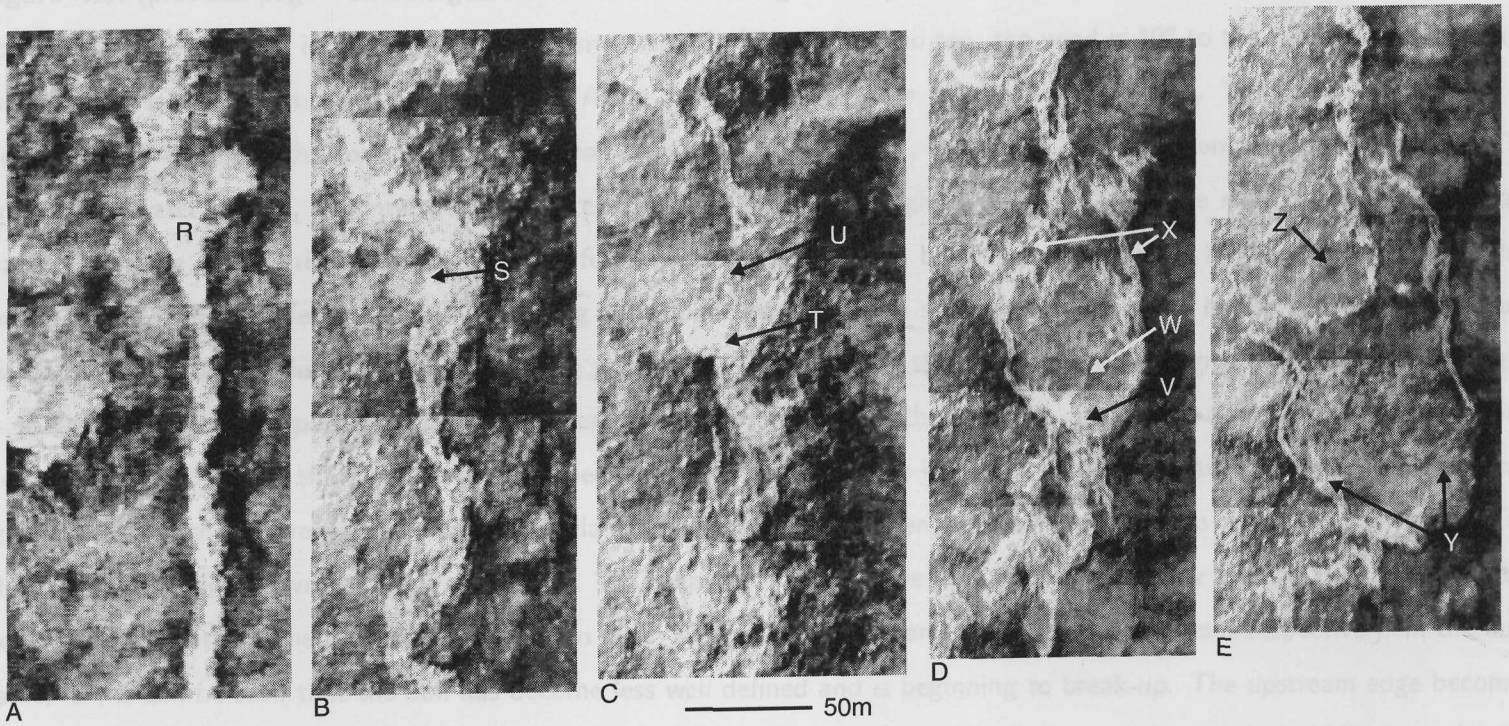
R
S
U
T
X
W
V
Z
Y
A
B
C
D
E
50m

Figure 4.9: (previous page - an enlarged version is shown in Figure D.3) Aerial video composites showing the evolution of a boil; region labeled as 'X' in Figure 4.8. The mean current is from bottom to top, the wind is 40^o to the left of the current and the images are about 5 min apart. The letters 'A' to 'E' correspond to the lettering in Figure 4.8. The undisturbed plume of diesel oil can be seen as the continuous light streak labeled 'R' in frame 'A', about $150 - 200$ m from the moored source. The surrounding water is dark, but interspersed with patches, or 'blobs', with lighter shading - these are regions high in particulate matter. In frame 'B' (5 min later and ~ 300 m further downstream) it can be seen that meanders have started to form within the oil plume. A boil, paler than the surrounding water because of its high sediment content, can be seen to be erupting just within the width of the plume at 'S'. A further 5 min later, it can be seen that the boil, 'U', has grown in alongstream length to ~ 25 m. Oil from the plume accumulates around the upstream edge of the boil, 'T', and begins to flow in filaments around the perimeter. Frame 'D' shows the fully developed boil, ~ 10 min after its initial appearance. A large accumulation of oil can again be seen at the upstream edge, 'V', a fine filament of which can be seen entering the upstream edge of the boil, 'W'. The oil passes in filaments down the sides of the boil, 'X', because of the relative drift between the slow moving boil and the faster moving surface waters. The boil measures ~ 50 m by ~ 75 m in the across and along-stream directions respectively. In the final frame, 'E', is can be seen that the boil has become less well defined and is beginning to break-up. The upstream edge becomes fragmented, 'Y', and the sediment within the boil settles out. A new, well-defined boil can be seen erupting within the perimeter of the old at 'Z'.

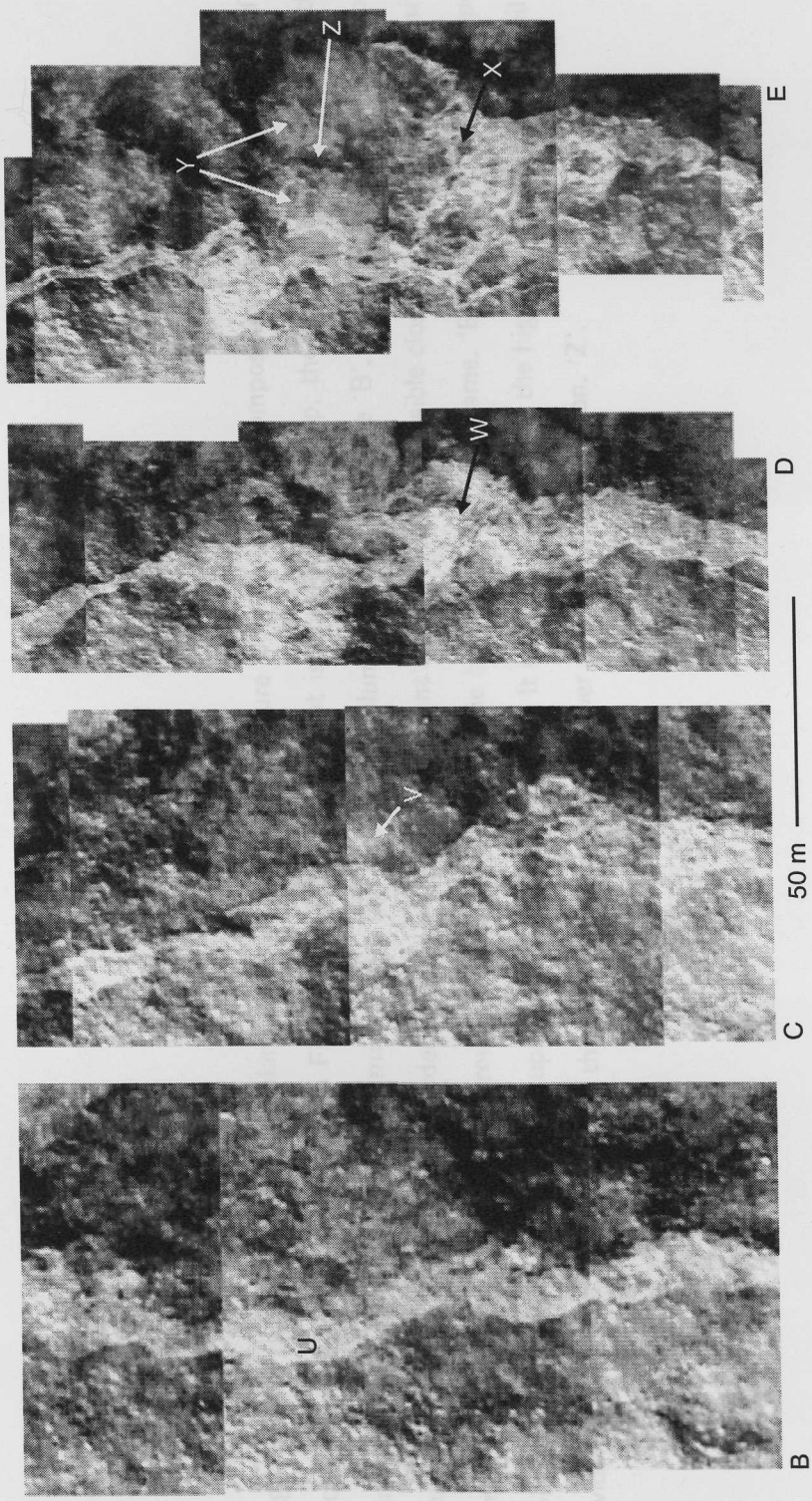
B
U
C
Y
50 m
D
W
E
Z
Y
X

Figure 4.10: (previous page - an enlarged version is shown in Figure D.4) Aerial video composites showing the evolution of a second boil; region labeled as 'Y' in Figure 4.8. The mean current is from bottom to top, the wind is 40^o to the left of the current and the images are about $5\ min$ apart. The undisturbed plume is shown in Frame 'B', labeled 'U'. Again, after about $5\ min$, the oil plume begins to meander, and a high sediment content boil, 'V', becomes visible close by. After a further $5\ min$, the oil can be seen to accumulate around the upstream edge of the boil, 'W'. The final frame, 'E', shows the fully developed boil. The accumulation of oil at the upstream edge is visible at 'X'. It can also be seen that the high sediment within the boil is divided into two, 'Y', separated by a thin filament of water with lower sediment concentration, 'Z'.

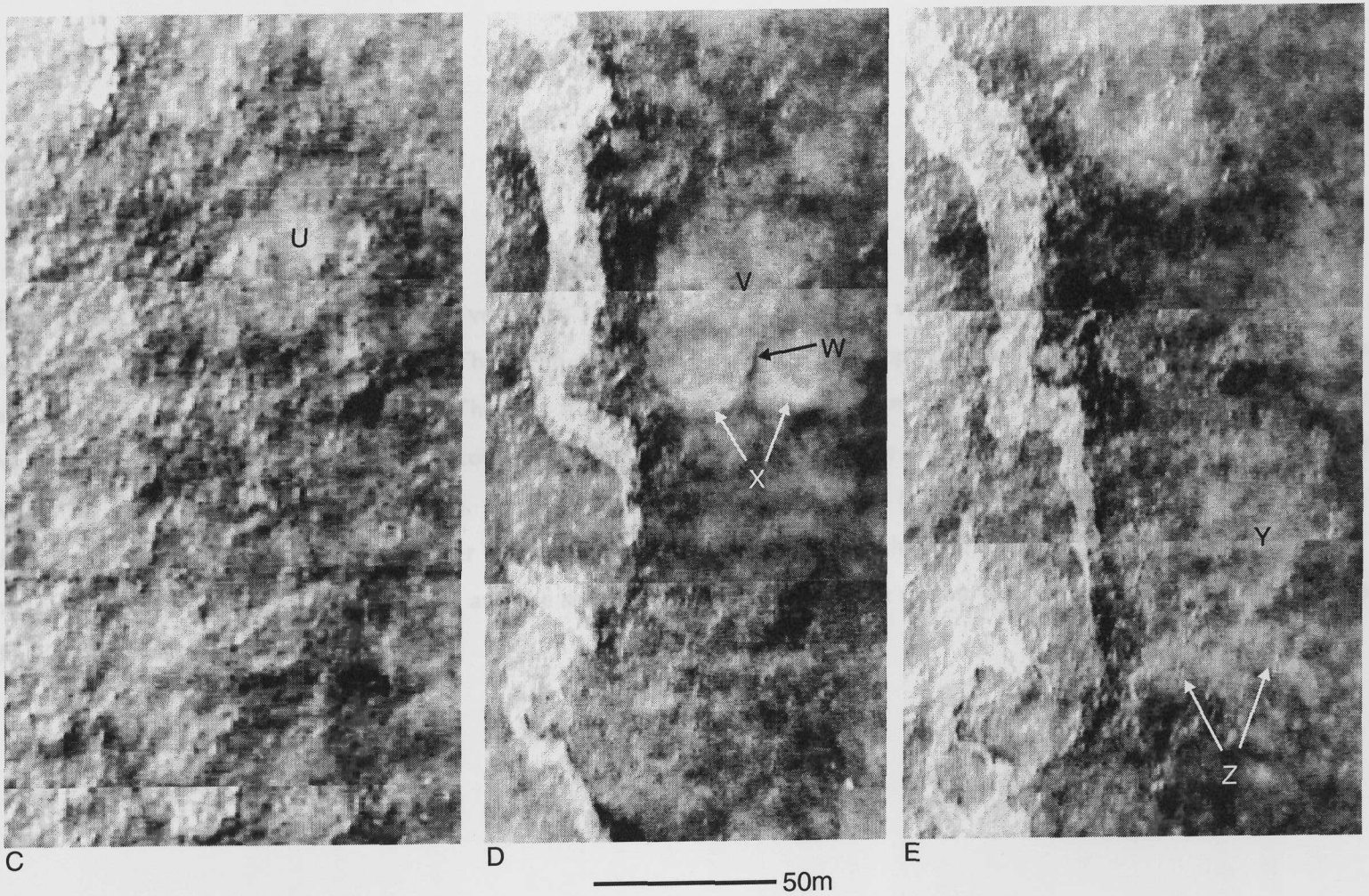
U
V
W
X
Y
Z
C
D
E
50m

Figure 4.11: (previous page - an enlarged version is shown in Figure D.5) Aerial video composites showing the evolution of a boil; region labeled as 'Z' in Figure 4.8. The mean current is from bottom to top, the wind is 40^o to the left of the current and the images are about $5\ min$ apart. The first frame, 'C', shows the initial emergence of a sediment patch, 'U', within a region of darker water with lower sediment concentration upstream of the oil release point. $5\ min$ later (Frame 'D') the structure within the sediment patch, 'V', can be seen. The patch is divided into two regions by a filament of clearer water, 'W', with well defined upstream edges, 'X'. After a further $5\ min$, it can be seen in Frame 'E' that the patch, although still in evidence, 'Y', has become diffuse as the coherence is lost and the sediment begins to settle back out. It is still just possible to distinguish the double structure to the upstream edge, 'Z'.

The mean diameter of the regions in which the oil plume is disrupted is $47 \pm 14\ m$ or $(1.04 \pm 0.31)H$, covering a proportion, $p \approx 0.2$, of the water surface within the images. Features in the oil plume tracked through the sequence of overflights decay, or are engulfed in new, but similar features in a time $\tau = 410 \pm 140\ s$, a lower bound because of the limited time-span of the images. The patches of water with paler shading than their surroundings have a mean diameter of $65 \pm 15\ m$ or $(1.44 \pm 0.33)H$, and they cover $p \approx 0.3$ of the water surface. The number of such features per unit area is therefore $0.3/[(\pi/4)65^2] = 9.0 \times 10^{-5}\ m^{-2}$.

The evolution of these features is also seen in the Compact Airborne Spectrographic Imager (CASI) images of the break-up of an oil patch (Figure 4.12). These images are from a later experiment in the same location investigating the weathering characteristics of various grades of crude oil. Here 33,190 litres of Alaska North Slope crude oil were released into a patch and then allowed to disperse naturally before being sprayed with chemical dispersants. These images, taken over 48 *hrs* after the release of the oil (or after about 4 tidal cycles) and just prior to the spraying of the chemical dispersants, show the formation of thick filaments, consisting of a viscous emulsion of oil and water, surrounded by areas of thin oil sheen. The filaments, possibly originally formed by Langmuir circulation, are now being broken up by the emergence of boils as shown by the emergence of feature 'A' in the short time (5 *min*) between the two images.

The presence of the filaments which divide the boils into two, indicates the evolution of a pair of eddies after the eruption of the boil, similar to the laboratory observations reviewed in Section 2.2.1. The filaments (as seen in Figures 4.10E and 4.11D) were observed in about 44% of the sediment patches recorded in the video images (covering $\sim 0.5\ km^2$). They are $8.6 \pm 2.4\ m$ in width and roughly aligned with the current.

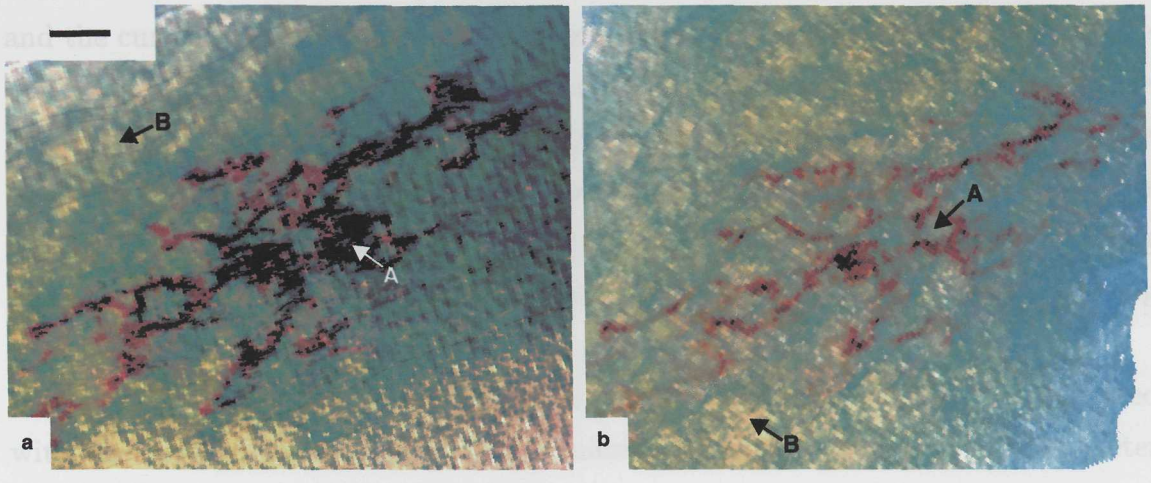

Figure 4.12: CASI false colour images of an oil patch (in red). The two images are of the same area of sea surface; **a** was taken 5 min before **b**. Scale bar, 100 m in both images. The oil has dispersed from a patch in the southern North Sea over a period of 4 tides (2 days) in an area of uniform depth, 45 m. The colour scale is different between the images, and **a** has been affected by cloud shadow. Oil thicker than 250 μm is imaged as red to black, while yellow and green result from ambient seawater and oil thinner than 5 μm. A roughly circular pale blob, of diameter 50 m, is formed within feature 'A' in the oil in the time between the two images. The yellow blobs (for example, at 'B') are clouds of particulates (see also Figures 4.8 ('P') and 4.11). North is to the top. The wind speed 10 m above the sea is 6.3 m s^{-1} from 340^o, and the current at 5 m depth is 0.99 m s^{-1} heading to 189^o.

4.3 ADCP and current meter signatures

The ADCP and current meter records provide additional information to that given in the sonar and aerial images. The instruments were set to record the data averaged over 1 *min*, 5 *min* or 15 *min* periods for the near-surface current meter, the ADCP and the current meters at one-third and two-third depths respectively because of the limited data storage capacity of the instruments. This means that it is not possible to resolve individual boils, or the sub-surface structures that lead to their surface manifestation, since these would be advected past a fixed point in under the periods over which the instruments were averaging (for example a boil of 45 m diameter being advected at 0.8 $m\ s^{-1}$ would pass a moored instrument in at most 56 s, assuming that the centre of the boil passes directly over the mooring).

However, it is still possible to pick out certain features which may be associated with the presence of the boils. Unfortunately, the ADCP and 1 m current meter were not available for the period in which the boils were most obvious in the sonar record (for the periods around that shown in Figure 4.6). However, extensive data are available from earlier and later deployments, a sample of which is shown in Figure 4.13. The period shown is about 6 *hrs* in duration, the time between two successive slack waters, in which the (10 m) wind remained nearly constant at 5 $m\ s^{-1}$. The sonar record for the tidal cycle shows that boils are present at the surface for the period between the two arrows ('X'). It can be seen that the current reaches a peak speed of over 70 $cm\ s^{-1}$, with the maximum values found near the surface. The relative backscatter - the strength of the returning acoustic signal corrected for the attenuation of sound with distance from source and normalised - gives a measure of the amount of suspended particles in the water [Holdaway et al., 1999]. It can be seen that the strongest relative backscatter is found at greater depth within the water column, indicating that the particles are sediment carried off the sea bed. The maximum near-surface backscatter occurs about 1.5 *hrs* after the first high values are recorded at 25 m depth and about $20 - 40$ *min* after boils are first seen at the surface in the sonar record, suggesting that the coherent structures which form the boils at the

surface also transport sediment from the sea bed up into the water column.

Other noteworthy features of both the current speed and relative backscatter records are the apparent 'pulsing', with about 15 *min* periodicity, and diagonal banding (shown by line *Y* in Figure 4.13b). The 'pulsing' can be seen most clearly around the 15 *hr* time where the current speed over the entire water column fluctuates by about 15 $cm\ s^{-1}$ and the relative backscatter alternates between weak and strong. It is possible that this pulsing is produced as one or more of the coherent structures, which produce the boils at the surface, are advected past the ADCP. It has been shown that the boils have a relatively high sediment concentration, giving short periods of relatively high backscatter, and that they travel more slowly than the surrounding waters, giving short periods of relatively slow current speeds. The short pulses of high backscatter qualitatively appear to coincide with the pulses of relatively slow current speed, although though there is no significant statistical correlation between the two.

The second feature, the diagonal banding, is highlighted by the line 'Y' drawn on the relative backscatter record, but is also faintly visible in the current speed. The features can be traced for at least 15 *min* (equivalent to an alongstream length of $\sim 540\ m$), changing about 5 *m* in depth over this period. It could be expected that coherent structures similar to those seen in the laboratory experiments reviewed in Section 2.2.1 would produce these features, with the 'head' of the structures downstream and higher in the water column than the trailing 'legs'. The upward movement of the coherent structures as they pass the ADCP would account for the relatively small vertical extent of these diagonal features.

Little extra information can be drawn from the 15 *m* and 30 *m* current meter records (Figure 4.13c) because of the long periods over which they were averaging their readings. However, the record from the 1 *m* current meter, which was averaging over periods of 1 *min* only, shows a signature which can be attributed to the presence of the boils. During the period in which the tidal current is accelerating from slack water to the time of maximum flow it can be seen that the record is smooth, with fluctuations of very low amplitude. However, about 30 *min* before the peak tidal

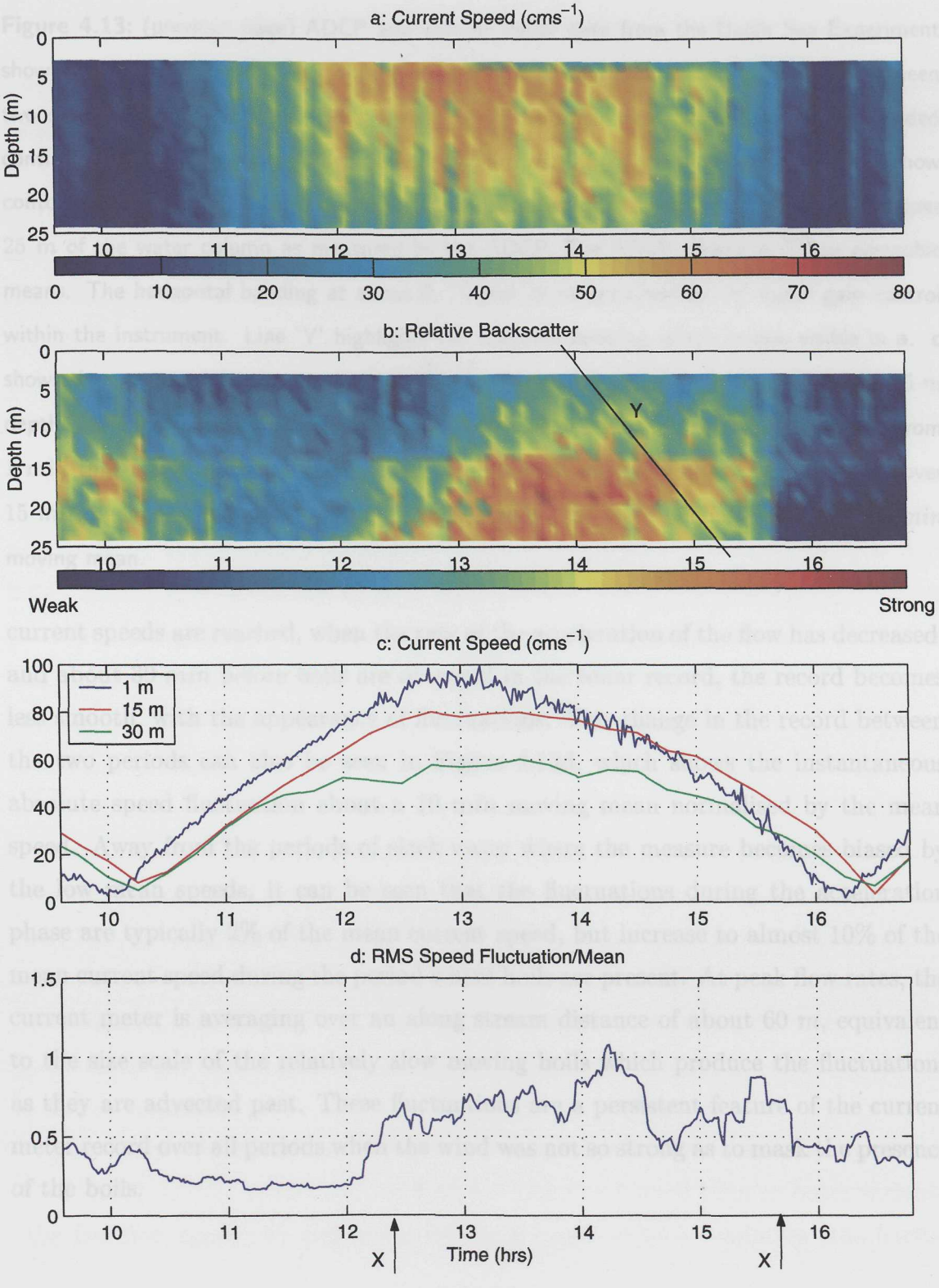
a: Current Speed (cms^{-1})
Depth (m)
0
5
10
15
20
25
10
11
12
13
14
15
16
0
10
20
30
40
50
60
70
80
b: Relative Backscatter
Depth (m)
Y
Weak
Strong
c: Current Speed (cms^{-1})
1 m
15 m
30 m
100
80
60
40
20
0
d: RMS Speed Fluctuation/Mean
1.5
1
0.5
0
X
Time (hrs)
X

Figure 4.13: (previous page) ADCP and current meter data from the North Sea Experiment showing the signatures of boils. The period shown is a tidal quarter cycle - the time between two consecutive slack waters. Boils are visible in the sonar data, which was being recorded continuously, in the time period between the two arrows, 'X' (on the x-axis of **d**). **a** and **b** show contoured time-series of speed and relative acoustic backscatter respectively from the upper 25 m of the water column as measured by the ADCP. The ADCP recorded 5 min ensemble means. The horizontal banding at about 8, 12 and 19 m is caused by the signal gain control within the instrument. Line 'Y' highlights the diagonal banding which is also visible in **a**. **c** shows the current speeds as measured by three current meters, one at 1 m depth, one at 15 m depth and one at 30 m depth. The 1 m current meter recorded vector averages over from 1 min time intervals, while the 15 m and 30 m current meters recorded averages made over 15 min periods. **d** shows the absolute instantaneous 1 m speed fluctuation about a 10 min moving mean.

current speeds are reached, when the rate of the acceleration of the flow has decreased, and about 30 min before boils are observed in the sonar record, the record becomes less smooth, with the appearance of fluctuations. This change in the record between the two periods can also be seen in Figure 4.13d, which shows the instantaneous absolute speed fluctuation about a 10 min moving mean normalised by the mean speed. Away from the periods of slack water where the measure becomes biased by the low mean speeds, it can be seen that the fluctuations during the acceleration phase are typically 2% of the mean current speed, but increase to almost 10% of the mean current speed during the period where boils are present. At peak flow rates, the current meter is averaging over an along stream distance of about 60 m, equivalent to the size scale of the relatively slow moving boils which produce the fluctuations as they are advected past. These fluctuations are a persistent feature of the current meter record over all periods when the wind was not so strong as to mask the presence of the boils.

4.4 Intermittency and scaling

The appearance of the boils in the sonar images and their signature in the near-surface current meter records lags the increasing tidal flow by $100 - 150$ min, an observation which is consistent with other sonar data [Graham and Hall, 1997], observations of suspended sediment concentration [Jago and Jones, 1998], and measurements and models of the kinetic energy of developing turbulence [Baumert and Radach, 1992, Schroder and Siedler, 1989]. This lag represents the time before coherent structures are produced in the strongly-sheared boundary layer near the sea bed, and for them to amalgamate, grow and permeate upwards through the water column to the surface, producing boils. In consequence, boils are only observed at the surface for about 70% of the tidal cycle.

Although the 'pulsing' within the ADCP data (described in the previous section) may indicate the existence of groups of boils, the simple statistical analysis of a 2.6 hr sonar record which follows suggests otherwise. The times at which dark hooked features, the signature of boils, were advected through the sonar beam were recorded and converted to alongstream distance using the current speed from the 1/3 depth current meter, so that in effect the measurements cover a strip 180 m in width and over 9 km in length. The mean number of boils per 200 m alongstream distance was calculated as $\overline{x} = 3.33$ with a variance $\sigma_x^2 = 3.34$ in a total of $n = 46$ bins. The index of dispersion, $I = \sigma_x^2/\overline{x}$ [Fisher, 1954], can then be calculated and tested for significance. The absolute value of d, $= \sqrt{2\chi^2} - \sqrt{2n-1} = -0.04$ (where $\chi^2 = I(n-1)$), is less than 1.96, so that agreement with a completely spacially random distribution can be accepted ($n = 46$, $P = 0.05$). This being said, the 'frozen field' approximation may be erroneous, since after a boil has passed the sonar, any subsequent boils erupting upstream of the first as part of a group may have already passed the sonar beam, and so not be recorded.

The characteristics of the surface eddies observed in the laboratory by Kumar et al. [1998], such as separation and size, are found to depend both on outer variables (the free-flow speed, U, and water depth, H) and on inner variables (the friction

velocity at the bed, and the kinematic viscosity, ν). The diameter of the laboratory eddies decreases with increasing Reynolds number, $Re = UH/\nu$, being about $3H$ at $Re = 8.8 \times 10^3$, and greater than the size, about H, of the eddies marked by sediment in the North Sea. The laboratory Reynolds number is, however, relatively small, ranging from 4.0×10^3 to 8.8×10^3, whereas Re is about 4.5×10^7 in the North Sea. Whilst the relatively smaller size of the sediment patches may be accounted for by the sinking of sediment (probably faster than 5×10^{-3} $m\ s^{-1}$, the settling speed of particulates in the region [Jago and Jones, 1998]), the observation that the laboratory scaling depends on inner variables suggests that the differences in scale may be simply a consequence of the difference in Re. The mean periodicity of boils at a point on the water surface, $\overline{T} = (NH)^{-1} = 236$ s, is consistent with the mean periodicity of bursts observed in the laboratory (see Section 2.2) and in a smooth-bottomed river (see Section 2.2.2), with the scaling factor, $a = U/NH^2 \approx 5$, falling within the range (3-7) of the other experiments.

4.5 Conclusions

The acoustic and visually observed features have the characteristics of the boils often seen in fast-flowing shallow rivers and narrow channels. The boils move at a speed different to that of the surface wind drift layer, leading to the formation of a region of surface convergence around the up wind-drift side of the boil. This convergence region traps bubbles, allowing the boils to be detected by the sonars. The boils are high in suspended sediment, pointing to their origin being the strongly-sheared boundary layer close to the sea bed.

The images capture the generation of tidal boils and eddies over a level sea bed, showing that they are likely to be of common occurrence in tidal shelf-seas. They also provide insight into the vertical transport of water, sediment and algae on the shelf, at the larger scales that develop following ejections in turbulent bursts from close to the sea bed. The boils impose a patchy structure in, for example, the colour of the water surface, which may bias the measured average values of the sea-surface

parameters detected by satellite or other 'remote' sensors. The images illustrate how boils disperse oil patches or plumes, a process which is developed in the next chapter. The appearance of the circles in the oil films (Figure 4.12) demonstrates that boils help to replenish surface waters, a process important in gas exchange [Thorpe, 1982, Woolf and Thorpe, 1991]. We predict that such boils will be absent at the surface of density-stratified seas, where the thermocline separates the surface and the deep water, preventing bursts and ejections generated in the benthic boundary layer from reaching the surface. The intensity of near-surface turbulence, the dispersion it causes and the rate of air-sea gas exchange in deep stratified oceanic waters may in consequence be lower in density stratified waters than in well mixed tidal seas.

Chapter 5

Dispersion by "boils" in the absence of wind

A series of simple analytical and numerical models were constructed to study the effects of boils on the dispersion of buoyant material. The analytical models allow a "back of the envelope" estimate for the lateral (across-current) dispersion to be made, while the numerical simulations provide both qualitative and quantitative predictions.

5.1 Analytical

A simple analytical model for the dispersion of buoyant material in the presence of boils is given in Nimmo Smith et al. [1999] (see Appendix C); this is reproduced and developed below.

The aerial video and CASI images presented and described in Section 4.2 demonstrate the dispersive effects of the boils on floating material. Neglecting wind, the horizontal dispersion coefficient normal to a steady tidal current over a smooth bottom is

$$K_{yT} = \beta U H \tag{5.1}$$

where β is a constant [Bowden, 1965] (see Section 2.3). A rough estimate for β can be found from these images. As an estimate, boils produce a lateral spread of floating particles over scales of order H at times corresponding to those separating the arrival of boils at a given position following the flow. If r is the number of boils produced per unit area per unit time, and T is their average 'lifetime', then the number of boils per unit area is rT. If they are advected at speed U, the number of boils passing a unit line normal to the flow in unit time is $N = rUT$. If A is the area of a single boil then the fractional area coverage of the surface by boils f, $= rTA = AN/U$ which, using the sonar data given in Section 4.1 and ignoring possible overlaps between boils, gives $f = 0.14 \pm 0.07$ (compared to observed $f \approx 0.2$). The surface area fraction covered per unit time is rA, and the average time for an area to be covered is therefore $T_m = (rA)^{-1}$, the mean time between boils affecting a given area moving with the mean flow. The dispersion coefficient is about $(H/2)^2/T_m$ (the square of the lateral displacement, $H/2$, divided by the time interval, T_m), or $ANH^2/4TU$ which, comparing with Equation 5.1 gives $\beta = ANH/4TU^2$. This is estimated to lie between 1.6×10^{-3} and 9.8×10^{-3}, using the sonar data (Section 4.1) and the probable underestimate of T based on the aerial video of the oil plume, and is slightly smaller than the value, $\beta = (1.0 \pm 0.4) \times 10^{-2}$, found in smooth bottomed laboratory channels (see Table 2.1).

This "first order" approximation can be developed by considering more carefully the displacement of the floating particles by the boils. In the model described above, the particles are displaced over a distance O(H), whereas in actual fact the mean lateral displacement of all the particles initially within the radius of any given boil will be significantly less than this. Components of this simple expansion to the model are shown in Figure 5.1.

The lateral dispersion coefficient can be redefined as

$$K_{yT} = \frac{\sigma_y^2}{2T_m} \tag{5.2}$$

where σ_y^2 is the variance of the lateral displacement of particles induced by a single boil. Now $\sigma_y^2 = E[\Delta y^2] - (E[\Delta y])^2$, where Δy is the displacement of a single particle

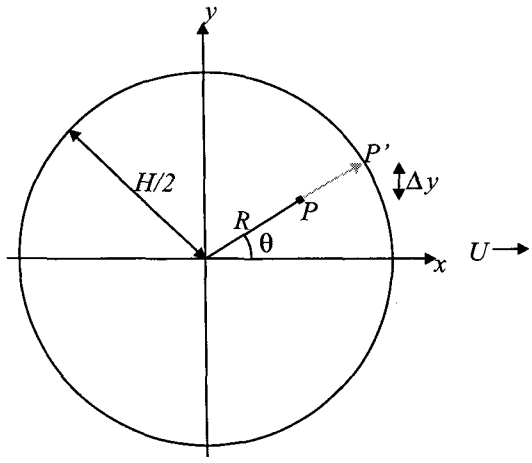

Figure 5.1: Simple model for the dispersion of buoyant particles by boils. The particles which are initially evenly distributed within the area of the boil are, in this model, all moved to a uniform distribution around its circumference when it erupts at the surface. Adopting a frame of reference with an origin at the centre of a boil of radius $H/2$ aligned with the direction of the current U, a particle, P, with initial position (R, θ) will be displaced by the radial flow to a final position, P', so that the displacement lateral to the mean flow is Δy.

lateral to the mean flow and E is the expectation. Since the boil is symmetrical, $E[\Delta y] = 0$, so $\sigma_y^2 = E[\Delta y^2]$.

The displacement of a single particle lateral to the mean flow, Δy, is given by $\Delta y = (H/2 - R)\sin\theta$, and so

$$\Delta y^2 = (H/2 - R)^2 \sin^2\theta. \tag{5.3}$$

Given that a boil has appeared, the probability, Pr, of the particle being between R and $R + dR$ from its centre is

$$Pr = \frac{2\pi R\, dR}{\pi(H/2)^2} = \frac{8R\, dR}{H^2}. \tag{5.4}$$

Therefore, averaging Equation 5.3 over all values of θ and inserting and evaluating Equation 5.4 for all values of R, it follows that

$$\sigma_y^2 = E[\Delta y^2] = \frac{1}{2\pi}\int_0^{2\pi}\int_0^{H/2} (H/2 - R)^2 \sin^2\theta\, \frac{8R\, dR}{H^2}\, d\theta \tag{5.5}$$

and so

$$\sigma_y^2 = \frac{4}{H^2}\int_0^{H/2}(H/2 - R)^2 R\, dR = \frac{H^2}{48} \tag{5.6}$$

Thus,

$$K_{yT} = \frac{\sigma_y^2}{2T_m} = \frac{ANH^2}{96TU} \tag{5.7}$$

so that β, $= K_{yT}/UH = ANH/96TU^2$, now ranges from 6.7×10^{-5} to 4.1×10^{-4}. Although these values are about two orders of magnitude less than the previous model estimates and the laboratory measurements, they are just less than, but still overlap, the range of the measurements from the well-mixed, southern North Sea, 3.7×10^{-4} to 3.0×10^{-3} (see Table 2.2). The differences between these model estimates, the laboratory measurements and the North Sea releases can be accounted for by the scaling of the boils with Re as discussed in Section 4.4.

Both these models consider only the dispersion produced as a direct result of the eruption of a circular boil and do not take into account the dispersion produced by any relative drift between the boils and the undisturbed particles or that produced by the eddies which evolve after the initial eruption of a boil at the surface. This may account for the relatively low values (relative to the North Sea measurements) calculated in the second version of the model. To further investigate the dispersion produced by boils, a series of numerical models were constructed, and these are described in the following section.

5.2 Numerical

Two forms of a simple numerical model were constructed to simulate the dispersion of either an evenly distributed area or a continuous plume of buoyant particles in the presence of boils. These are described in Sections 5.2.1 and 5.2.2 respectively. For the models to provide useful quantitative information, it was first necessary to find a relationship between the boil statistics measurable from the sonar and aerial data (f, A and T) and the number of boils produced per unit area per unit time (r). Initially

a simple numerical model was constructed in which boils of a specified area, A, and lifetime, T, were introduced into a fixed area, XY, at a given rate, rXY. Boils are generated centered at random locations within the area and appear and disappear instantaneously, so that the total number of boils within the model domain remains constant at $rTXY$. The mean total fractional area coverage by boils was calculated over a period of $10T$ for different values of rAT and is shown in Figure 5.2a along with curves of the fractional area coverage by the overlaps between boils, f_o, and the fractional area coverage by only one to only five boils, f_1 to f_5.

Since the boils are generated at a constant rate but - it is assumed - at random locations, it is possible to consider this relationship using a Poisson distribution [Crawshaw and Chambers, 1990]. Since rAT is the mean total area of boils per unit area, and if F is the random variable 'the total area of boils per unit area', then F follows the Poisson distribution, $F \sim \text{Po}(rAT)$. The fractional area covered by n boils is then

$$f_n = e^{-rAT}\frac{(rAT)^n}{n!}. \tag{5.8}$$

Therefore, the fractional area not covered by boils is $f_{zero} = e^{-rAT}$, and so the total fractional area covered by boils is

$$f = 1 - f_{zero} = 1 - e^{-rAT}, \tag{5.9}$$

$f_1 = rATe^{-rAT}$, $f_o = 1-(f_{zero}+f_1) = 1-(1+rAT)e^{-rAT}$, $f_2 = (rAT)^2/2 \cdot e^{-rAT}$, etc. Curves of f, f_o and f_1 to f_5 plotted against rAT are shown in Figure 5.2b. It can be seen that there is almost no difference between the analytical and numerical solutions. Taking values of f, T and $A = \pi(D/2)^2$ from the sonar data, $r = -\ln(1-f)/AT = 2.71 \times 10^{-7} m^{-2}s^{-1}$ and $N = rUT = 1.0 \times 10^{-4} m^{-1}s^{-1}$ which compares well to $N = 9.4 \pm 3.3 \times 10^{-5} m^{-1}s^{-1}$ measured from the sonar data. Using the same data, $f_o = 0.02$, showing that only about 10% of the area actually covered by boils is affected by overlaps between boils.

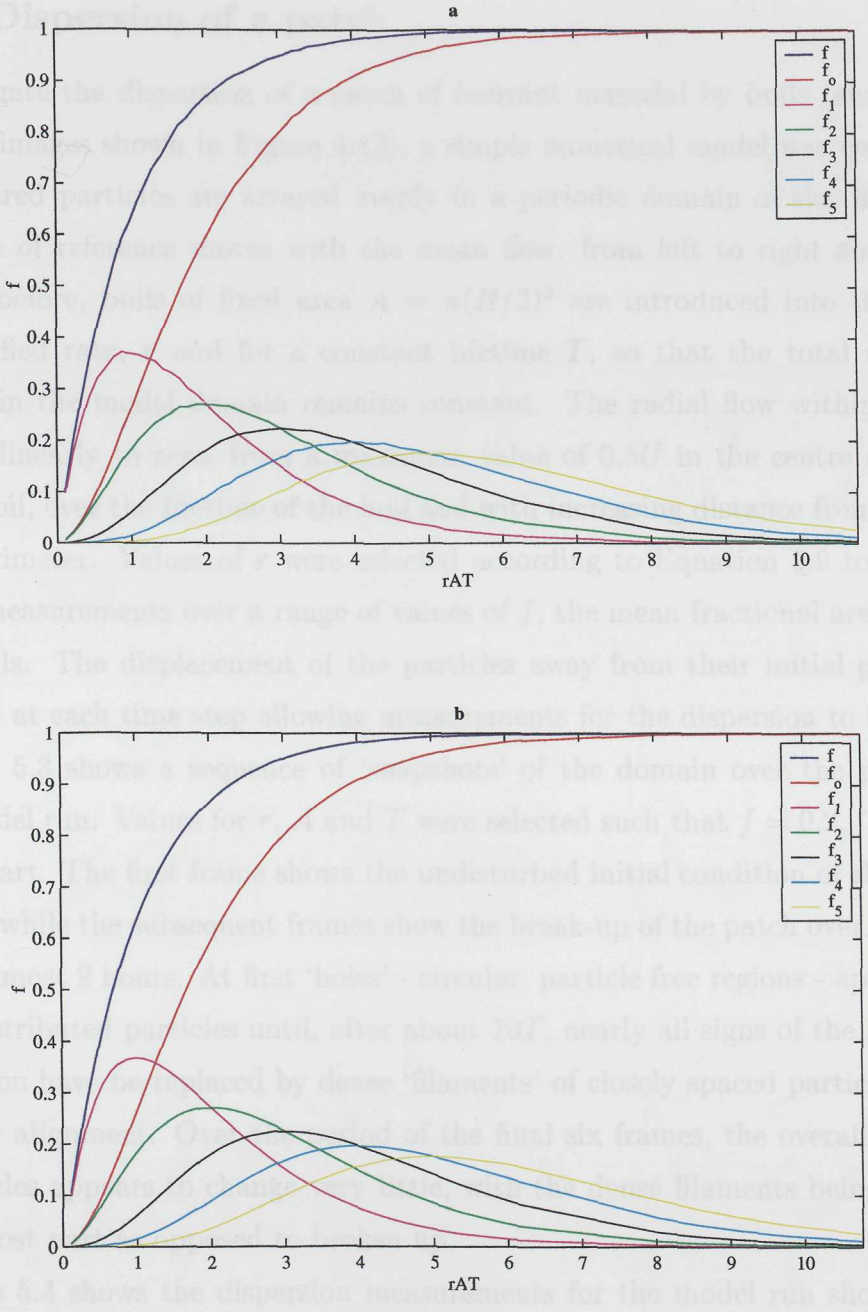

Figure 5.2: Numerical and analytical relationships between f, r, A and T. **a** Shows the relationship between different fractional area coverages and rAT, calculated numerically. The blue line shows the total fractional area coverage by boils, f, the red line shows the fractional area coverage by overlaps between boils, while the magenta, green, black, pale blue and yellow lines show the fractional area coverage by only one, two, ..., five boils respectively. **b** Lines are as for **a**, but calculated analytically.

5.2.1 Dispersion of a patch

To investigate the dispersion of a patch of buoyant material by boils (analogous to the CASI images shown in Figure 4.12), a simple numerical model was constructed. Four hundred particles are arrayed evenly in a periodic domain of size $4H$ square. The frame of reference moves with the mean flow, from left to right along the x-axis. As before, boils of fixed area $A = \pi(H/2)^2$ are introduced into the domain at a specified rate, r and for a constant lifetime T, so that the total number of boils within the model domain remains constant. The radial flow within the boils decreases linearly to zero, from a maximum value of $0.5U$ in the centre of a newly erupted boil, over the lifetime of the boil and with increasing distance from its centre to the perimeter. Values of r were selected according to Equation 5.9 to provide a series of measurements over a range of values of f, the mean fractional area coverage of the boils. The displacement of the particles away from their initial positions is calculated at each time step allowing measurements for the dispersion to be made.

Figure 5.3 shows a sequence of 'snapshots' of the domain over the period of a single model run. Values for r, A and T were selected such that $f = 0.2$. The frames are $2T$ apart. The first frame shows the undisturbed initial condition of the patch of particles, while the subsequent frames show the break-up of the patch over a period of $22T$, or almost 2 hours. At first 'holes' - circular, particle free regions - appear in the evenly distributed particles until, after about $10T$, nearly all signs of the initial even distribution have be replaced by dense 'filaments' of closely spaced particles with no particular alignment. Over the period of the final six frames, the overall pattern of the particles appears to change very little, with the dense filaments being displaced for the most part as opposed to broken up.

Figure 5.4 shows the dispersion measurements for the model run shown in Figure 5.3. It can be seen from Figure 5.4a that the mean non-dimensional displacement of the particles in both the x and y directions remain close to zero over the entire period, showing that there is no systematic bias in the model. The variance of the mean displacement is plotted against dispersion time in Figure 5.4b, showing that for

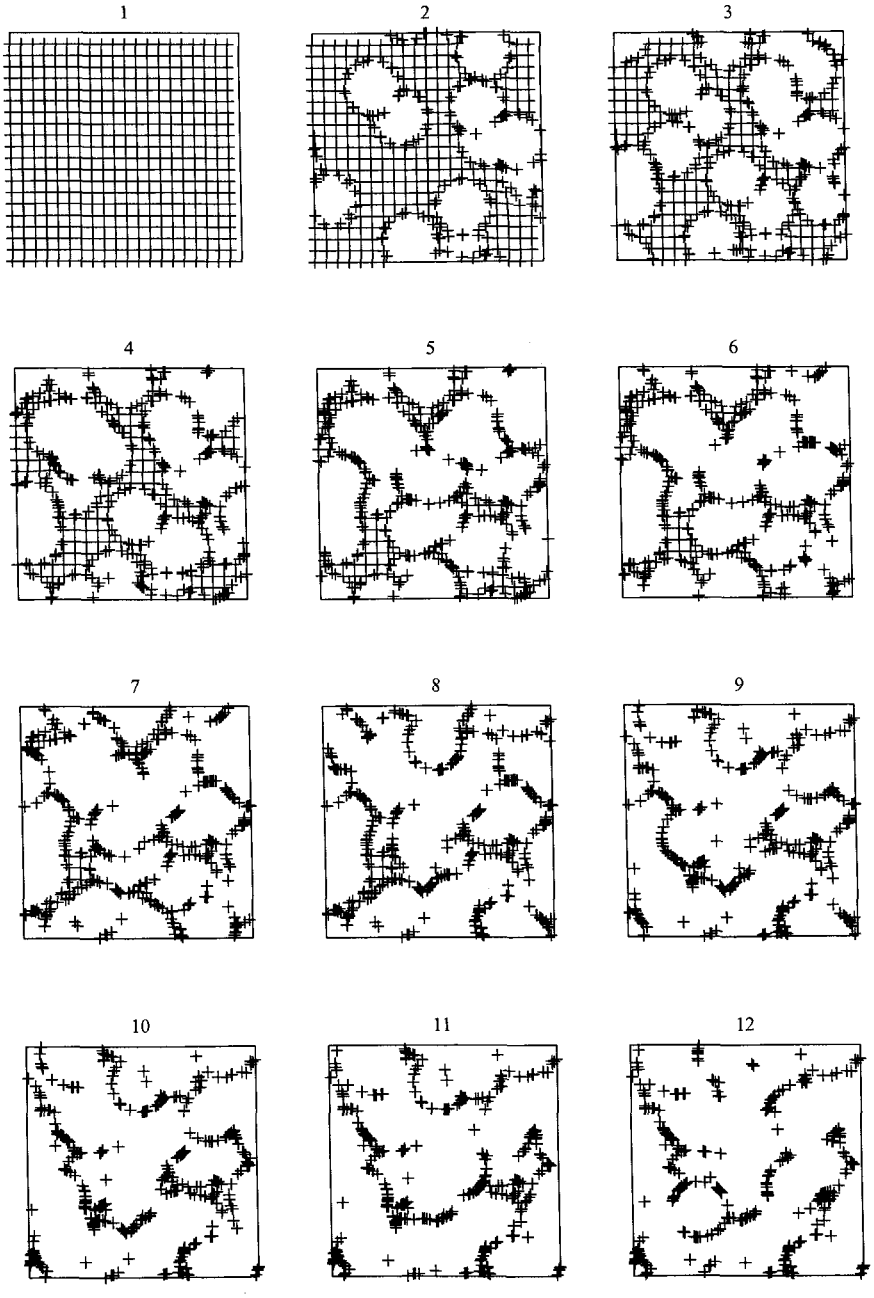

Figure 5.3: Dispersion of a patch of particles by boils in a periodic domain. The domain is $4H$ square and the interval between frames is $2T$. There is no relative motion between the undisturbed particles and the boils, and the radial flow within the boils decreases linearly with increasing radial distance and over the boil lifetime. Values of r, A and T were selected so that $f = 0.2$. The crosses represent particles initially arranged uniformly on the grid in Frame 1.

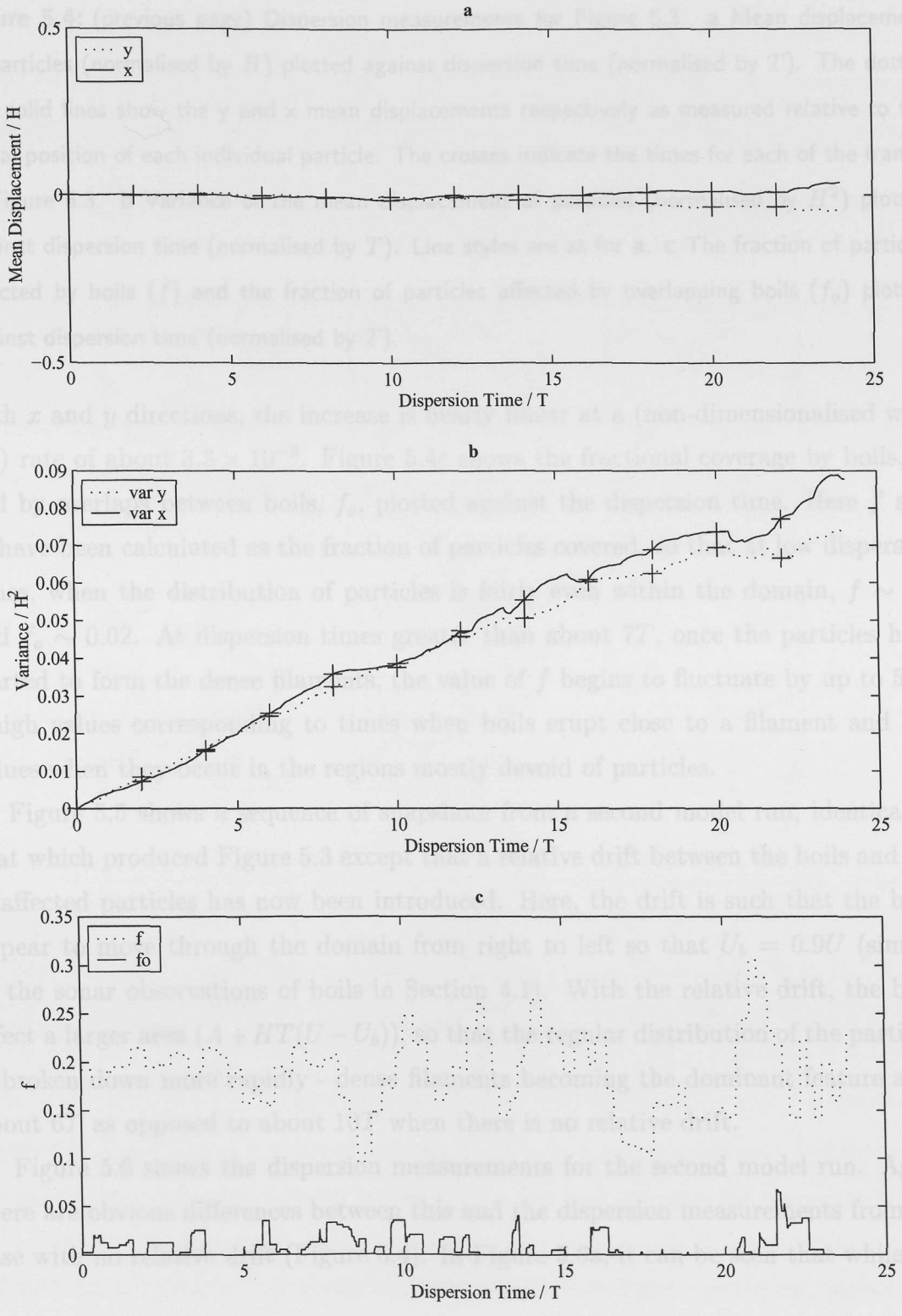
a
y
x
Mean Displacement / H
Dispersion Time / T
b
var y
var x
Variance / H²
Dispersion Time / T
c
f
fo
f
Dispersion Time / T

Figure 5.4: (previous page) Dispersion measurements for Figure 5.3. **a** Mean displacement of particles (normalised by H) plotted against dispersion time (normalised by T). The dotted and solid lines show the y and x mean displacements respectively as measured relative to the initial position of each individual particle. The crosses indicate the times for each of the frames in Figure 5.3. **b** Variance of the mean displacement of particles (normalised by H^2) plotted against dispersion time (normalised by T). Line styles are as for **a**. **c** The fraction of particles affected by boils (f) and the fraction of particles affected by overlapping boils (f_o) plotted against dispersion time (normalised by T).

both x and y directions, the increase is nearly linear at a (non-dimensionalised with H^2) rate of about 3.3×10^{-3}. Figure 5.4c shows the fractional coverage by boils, f, and by overlaps between boils, f_o, plotted against the dispersion time. Here f and f_o have been calculated as the fraction of particles covered, so that at low dispersion times, when the distribution of particles is fairly even within the domain, $f \sim 0.2$ and $f_o \sim 0.02$. At dispersion times greater than about $7T$, once the particles have started to form the dense filaments, the value of f begins to fluctuate by up to 50% - high values corresponding to times when boils erupt close to a filament and low values when they occur in the regions mostly devoid of particles.

Figure 5.5 shows a sequence of snapshots from a second model run, identical to that which produced Figure 5.3 except that a relative drift between the boils and the unaffected particles has now been introduced. Here, the drift is such that the boils appear to move through the domain from right to left so that $U_b = 0.9U$ (similar to the sonar observations of boils in Section 4.1). With the relative drift, the boils affect a larger area ($A + HT(U - U_b)$), so that the regular distribution of the particles is broken down more rapidly - dense filaments becoming the dominant feature after about $6T$ as opposed to about $10T$ when there is no relative drift.

Figure 5.6 shows the dispersion measurements for the second model run. Again there are obvious differences between this and the dispersion measurements from the case with no relative drift (Figure 5.4). In Figure 5.6a, it can be seen that while the

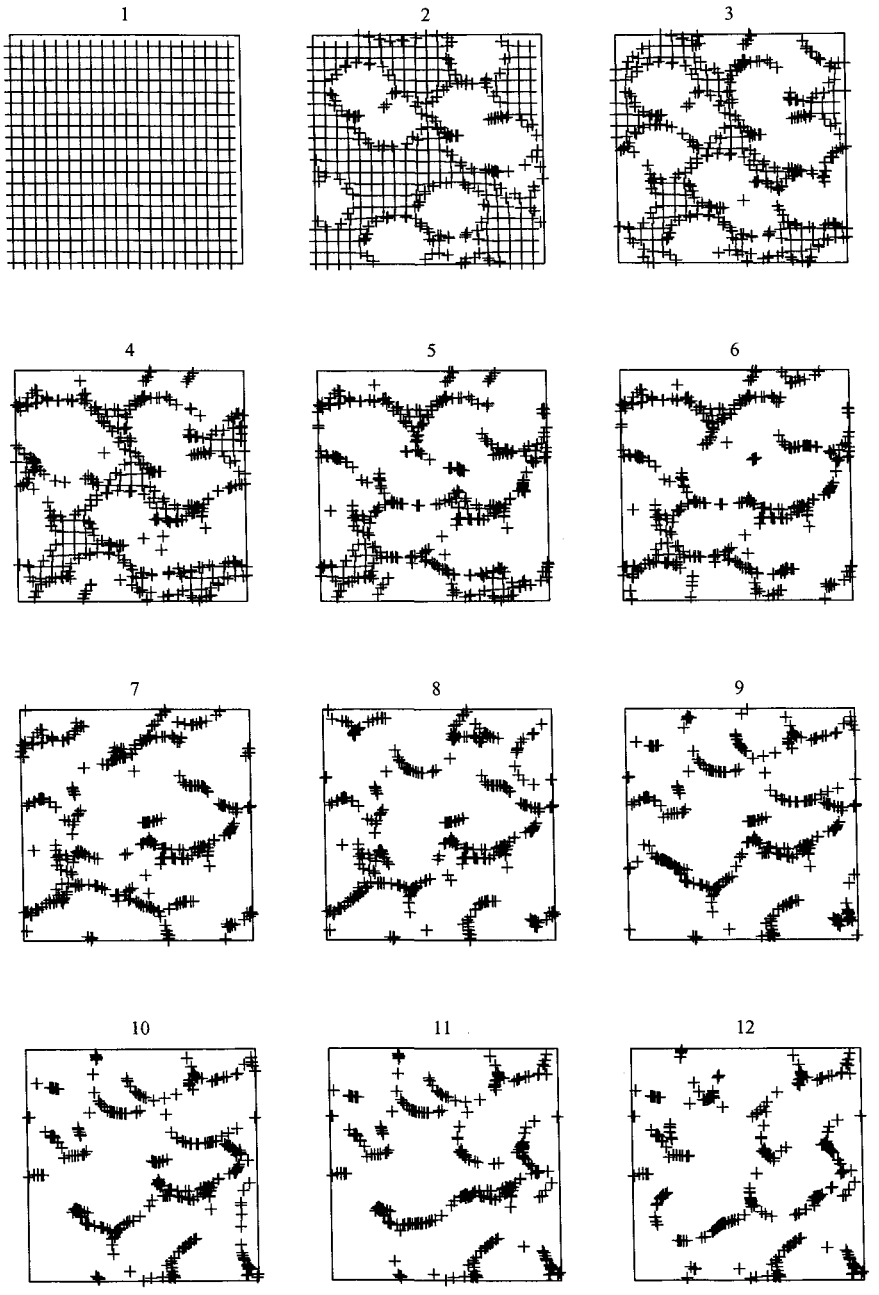

Figure 5.5: Dispersion of a patch of particles by boils in a periodic domain. The domain is $4H$ square and the interval between frames is $2T$. The boils are advected from right to left at $U_{brel} = 0.1U$ relative to the undisturbed particles (so that $U_b = 0.9U$), and the radial flow within the boils decreases linearly with increasing radial distance and over the boil lifetime.

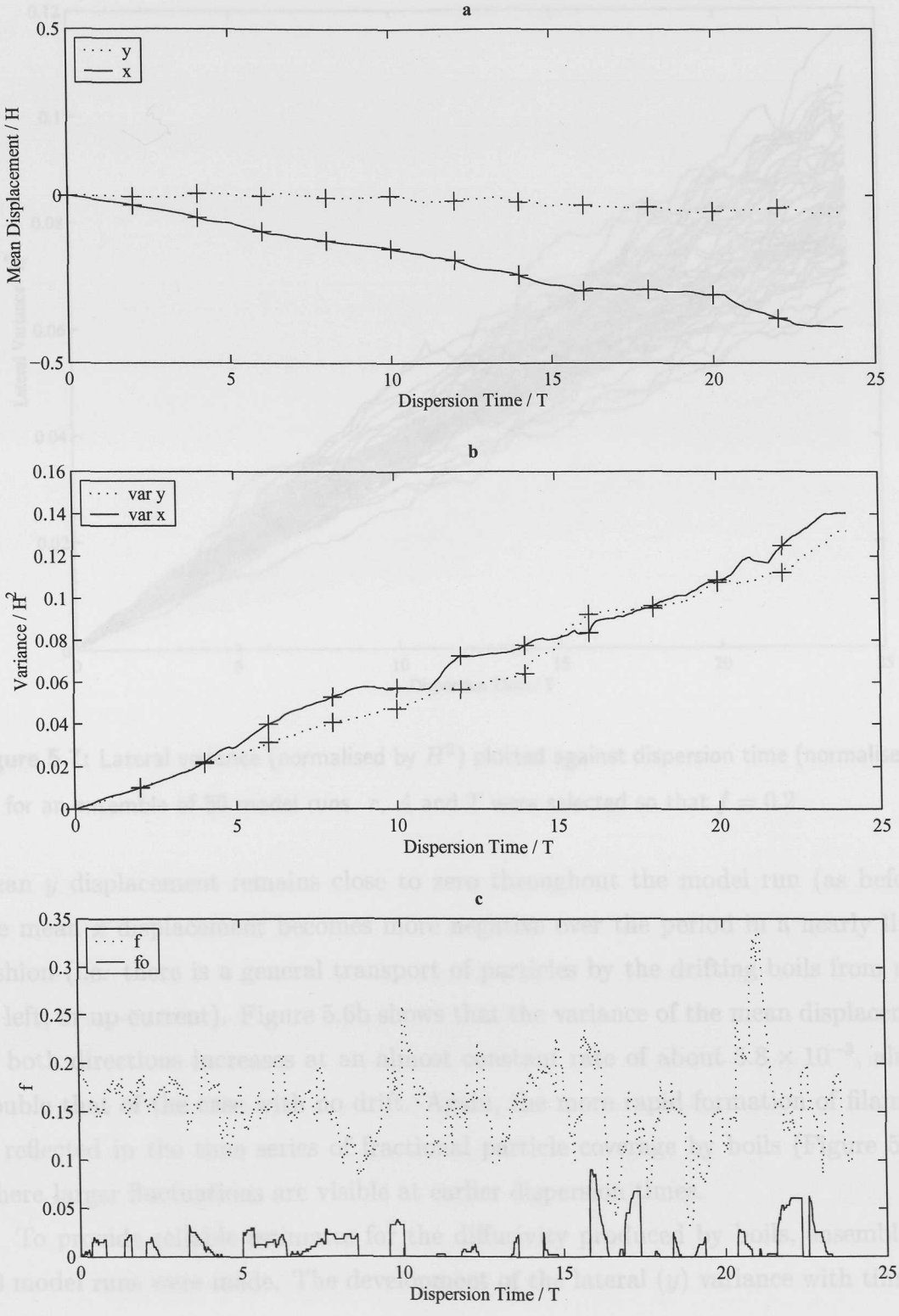

Figure 5.6: Dispersion measurements for Figure 5.5. Description is as for Figure 5.4.

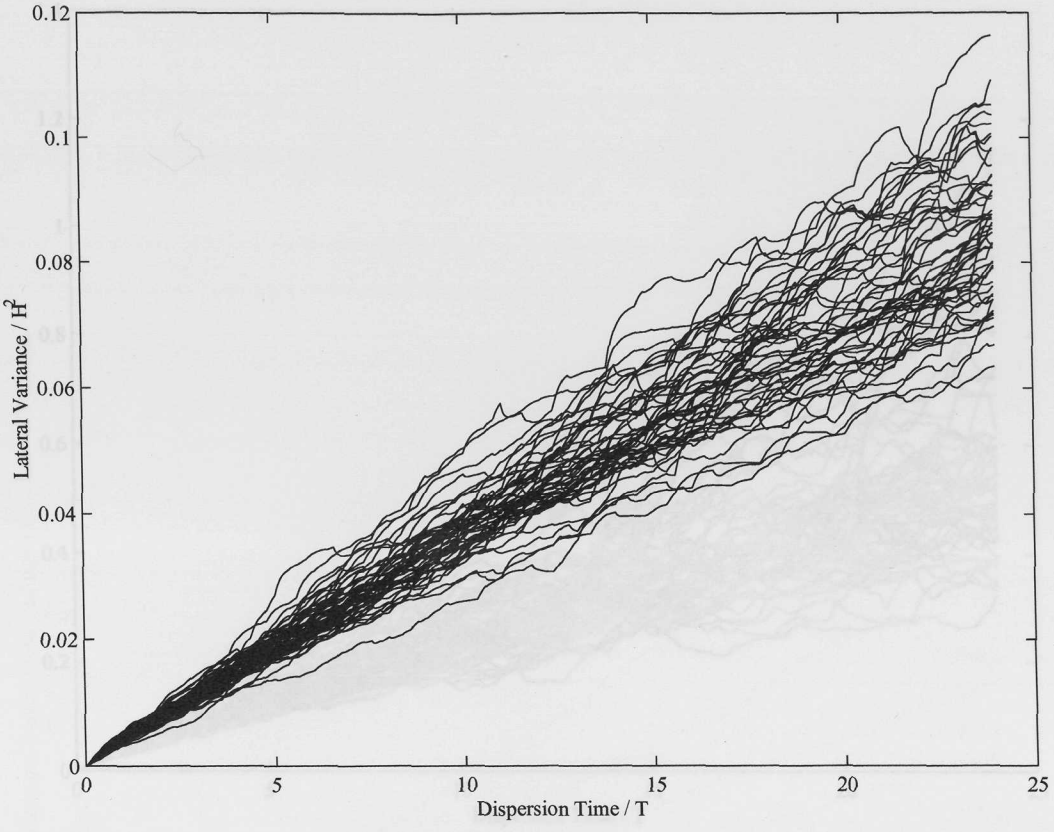

Figure 5.7: Lateral variance (normalised by H^2) plotted against dispersion time (normalised by T) for an ensemble of 50 model runs. r, A and T were selected so that $f = 0.2$

mean y displacement remains close to zero throughout the model run (as before), the mean x displacement becomes more negative over the period in a nearly linear fashion (i.e. there is a general transport of particles by the drifting boils from right to left, or up-current). Figure 5.6b shows that the variance of the mean displacement in both directions increases at an almost constant rate of about 5.8×10^{-3}, almost double that of the case with no drift. Again, the more rapid formation of filaments is reflected in the time series of fractional particle coverage by boils (Figure 5.6c), where larger fluctuations are visible at earlier dispersion times.

To provide reliable estimates for the diffusivity produced by boils, ensembles of 50 model runs were made. The development of the lateral (y) variance with time for

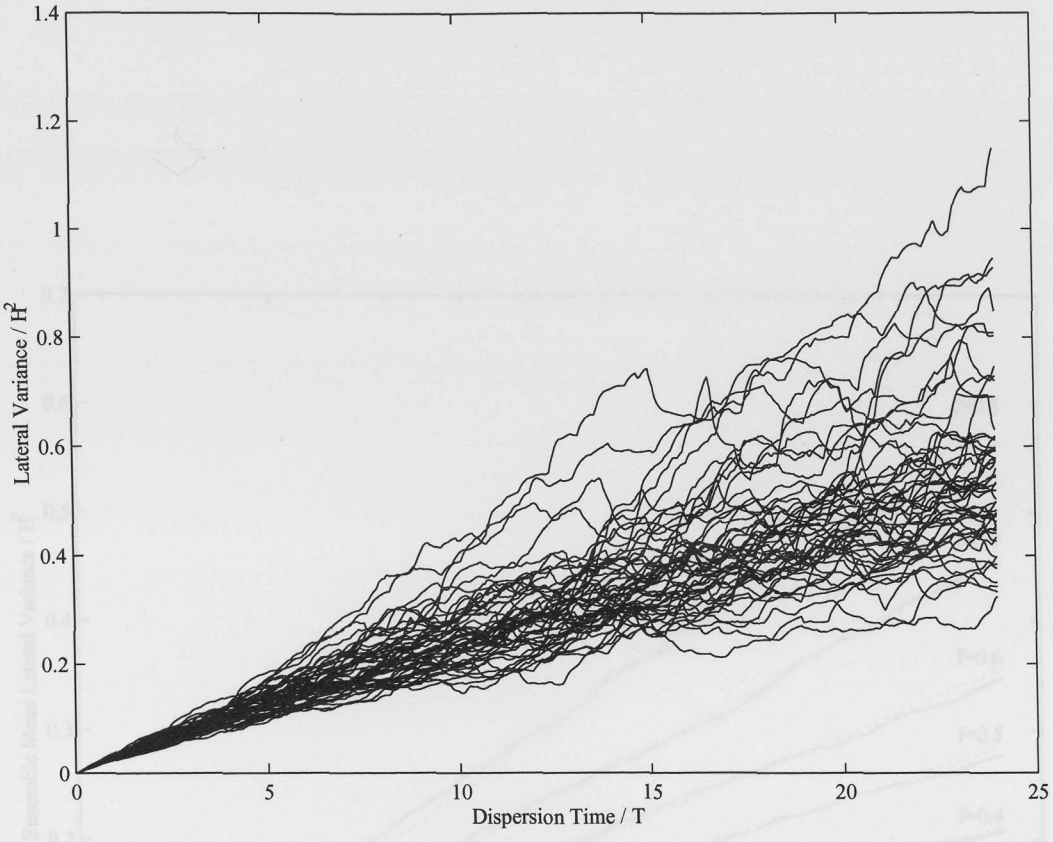

Figure 5.8: Lateral variance (normalised by H^2) plotted against dispersion time (normalised by T) for an ensemble of 50 model runs. r, A and T were selected so that $f = 0.8$

two such ensembles are shown in Figures 5.7 and 5.8 for $f = 0.2$ and 0.8 respectively and $U_b = U$. In both cases there are differences between individual runs within the ensembles which increase with increasing dispersion time. There is more scatter within the ensemble with the higher value of f.

The ensemble mean lateral variance is plotted against dispersion time over a range of values of f (set by varying r) in Figure 5.9. It can be seen that the ensemble means increase linearly with dispersion time. Regression lines were then fitted to each ensemble mean (dotted lines in Figure 5.9) from which the lateral diffusivity, K_y, and the non-dimensional diffusion coefficient, $\mathbf{K_y} \equiv \beta$, were then calculated. $\mathbf{K_y}$ is plotted against rAT in Figure 5.10.

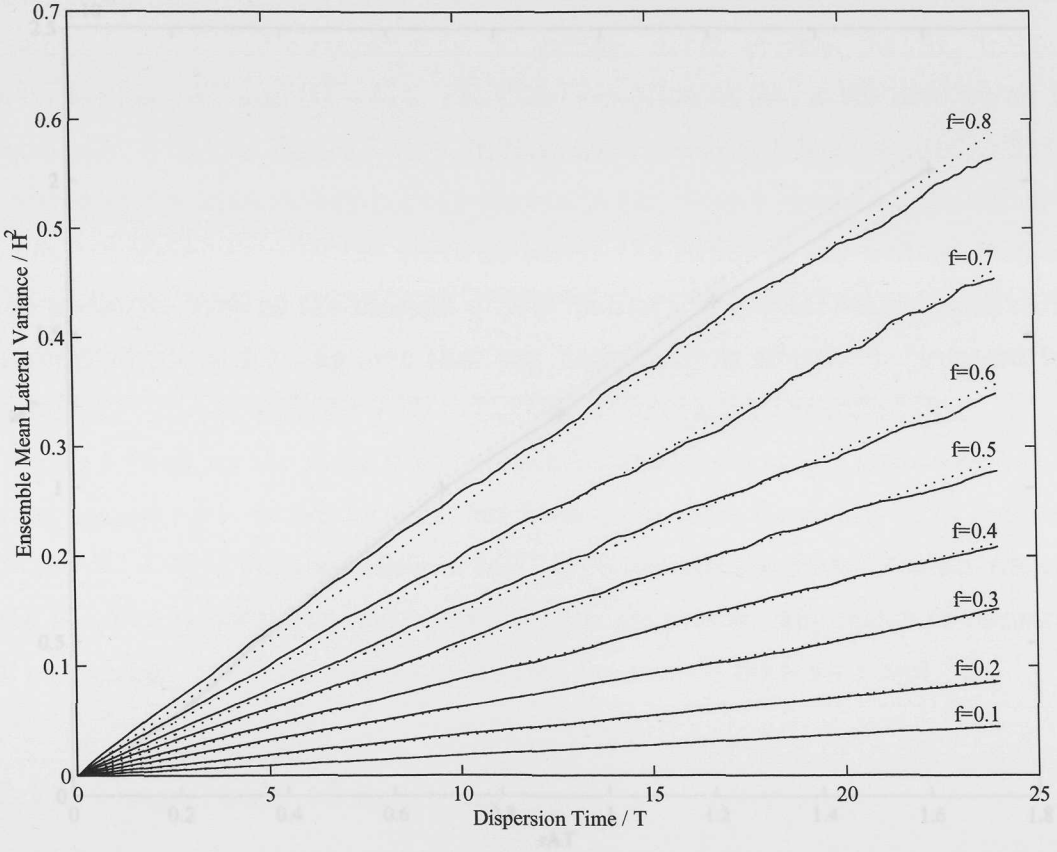

Figure 5.9: Ensemble mean lateral variance (normalised by H^2) plotted against dispersion time (normalised by T) for $f = 0.1, 0.2, \ldots, 0.8$ and $U_b = U$.

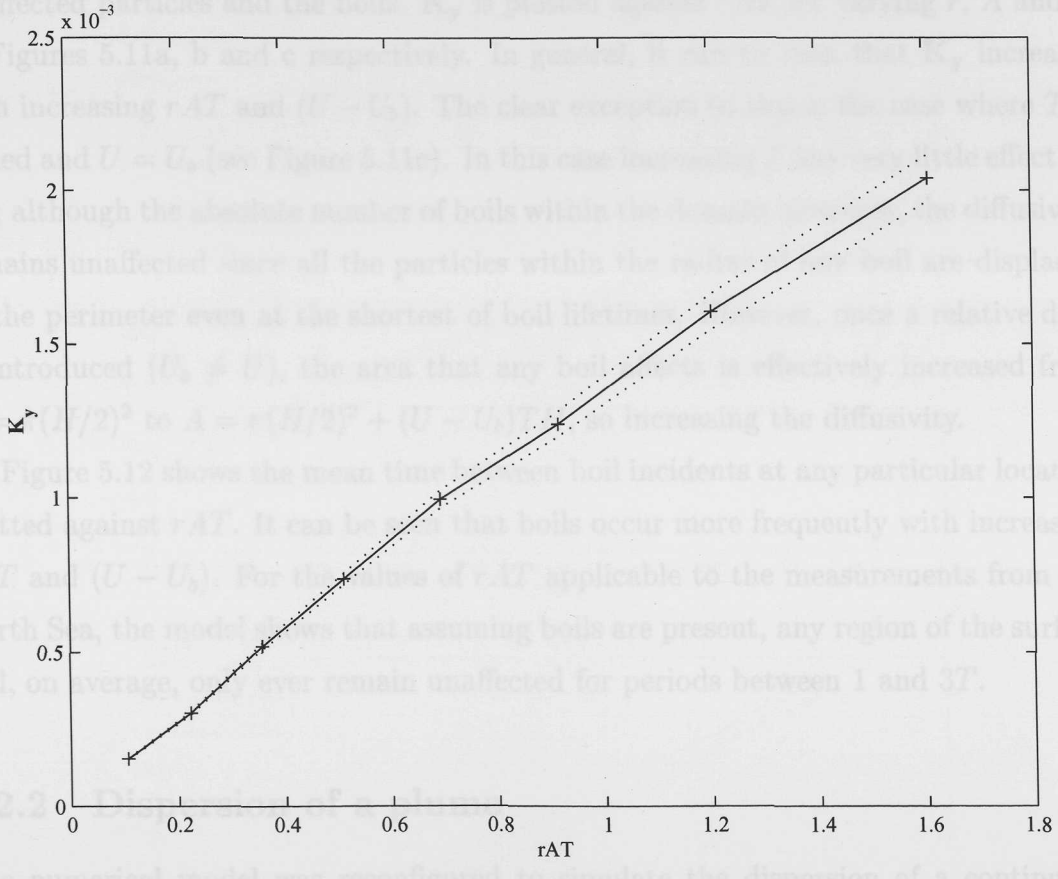

Figure 5.10: Non-dimensional lateral diffusivity (β) plotted against rAT. The dotted lines show the standard-error about the ensemble mean value.

It can be seen that there is a clear relationship between $\mathbf{K_y}$ and rAT. The relationship is approximately linear such that $\mathbf{K_y} \simeq 1.3 \times 10^{-3} rAT$ and so $\mathbf{K_y} \simeq -1.3 \times 10^{-3} \ln(1-f)$.

A further 27 ensembles of 50 model runs each were made to investigate the effects of changing each of r, A and T, and of increasing the relative drift between the unaffected particles and the boils. $\mathbf{K_y}$ is plotted against rAT for varying r, A and T in Figures 5.11a, b and c respectively. In general, it can be seen that $\mathbf{K_y}$ increases with increasing rAT and $(U - U_b)$. The clear exception to this is the case where T is varied and $U = U_b$ (see Figure 5.11c). In this case increasing T has very little effect on $\mathbf{K_y}$; although the absolute number of boils within the domain increases, the diffusivity remains unaffected since all the particles within the radius of any boil are displaced to the perimeter even at the shortest of boil lifetimes. However, once a relative drift is introduced ($U_b \neq U$), the area that any boil affects is effectively increased from $A = \pi(H/2)^2$ to $A = \pi(H/2)^2 + (U - U_b)TH$, so increasing the diffusivity.

Figure 5.12 shows the mean time between boil incidents at any particular location plotted against rAT. It can be seen that boils occur more frequently with increasing rAT and $(U - U_b)$. For the values of rAT applicable to the measurements from the North Sea, the model shows that assuming boils are present, any region of the surface will, on average, only ever remain unaffected for periods between 1 and $3T$.

5.2.2 Dispersion of a plume

The numerical model was reconfigured to simulate the dispersion of a continuous plume of buoyant material, similar to the diesel oil in the aerial video images shown in Section 4.2. 500 particles are released at a constant rate from a fixed source into a steady flow, forming a plume. Boils are generated within the model domain as before.

Figure 5.13 shows a sequence of snapshots of the plume of particles. The first frame is shortly after the first particles in the plume are released, while the second shows the full extent of the plume, measuring $10H$ in streamwise length, as yet undisturbed

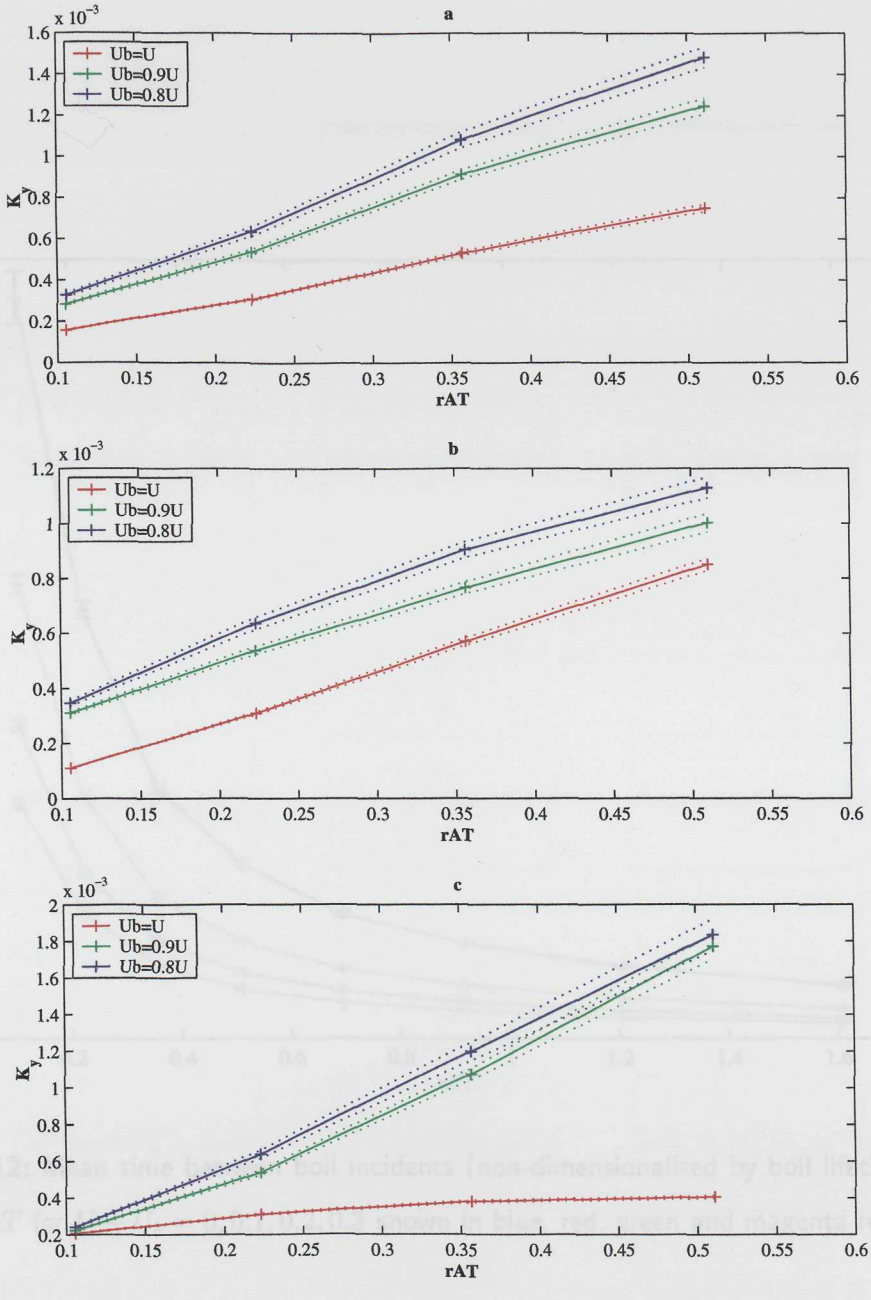

Figure 5.11: $\mathbf{K_y} = K_y/UH$ vs. rAT for different rAT variations. Red, green and blue lines are for $U_b = U$, $0.9U$ and $0.8U$ respectively. **a**, **b** and **c** are for values calculated by varying r, A and T respectively while keeping the other two constant.

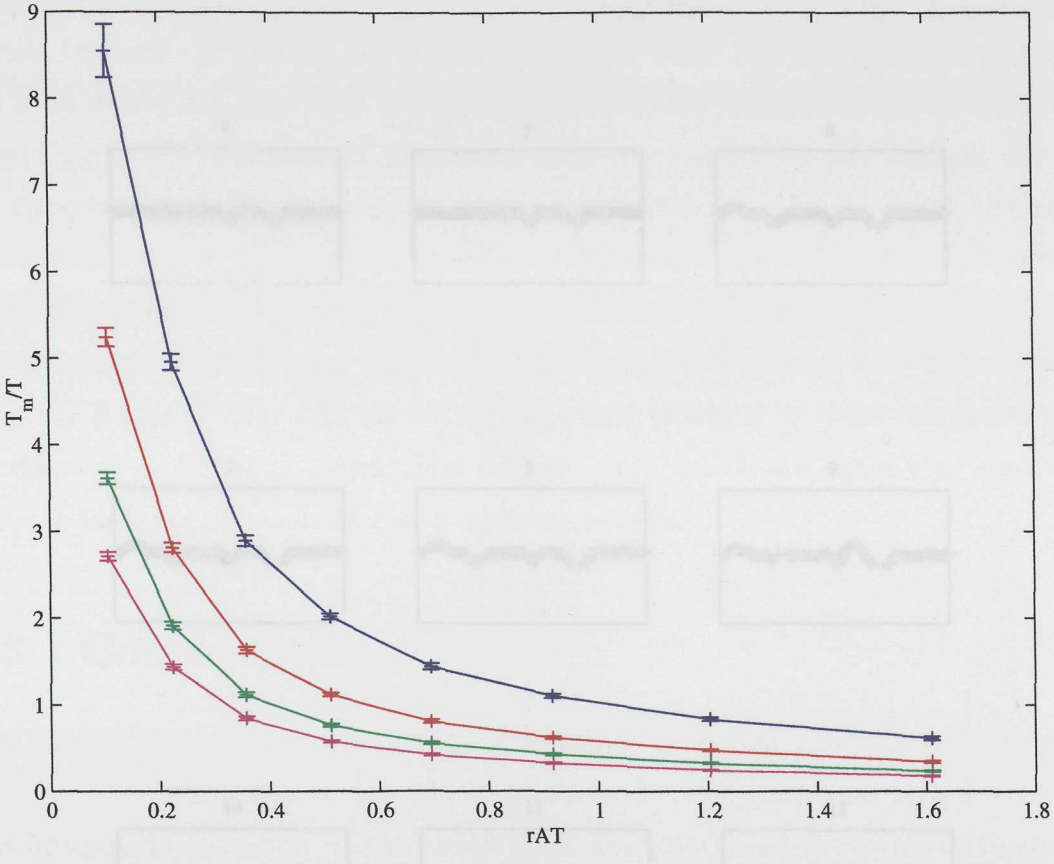

Figure 5.12: Mean time between boil incidents (non-dimensionalised by boil lifetime) plotted against rAT for $U - U_b = 0, 0.1, 0.2, 0.3$ shown in blue, red, green and magenta respectively.

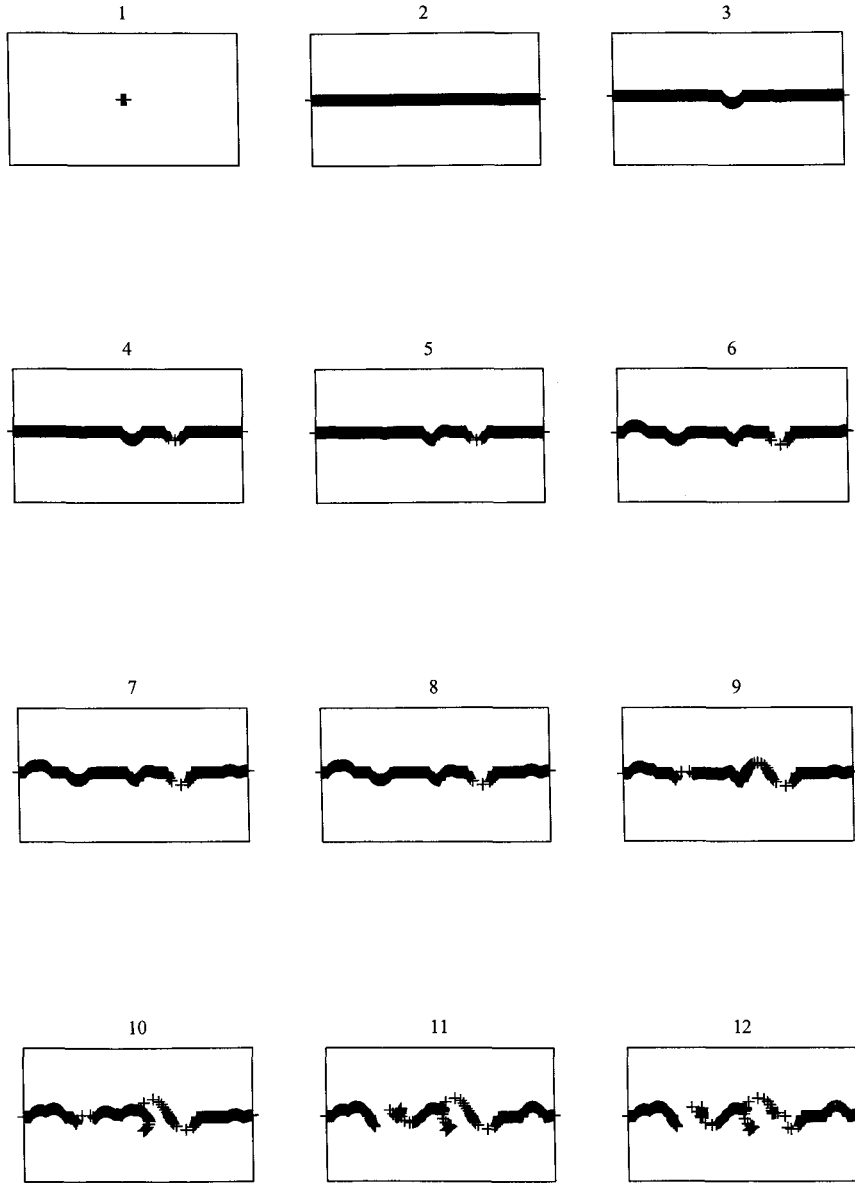

Figure 5.13: Dispersion of a plume of particles. The interval between frames is T. There is no relative motion between the undisturbed particles and the boils. Values of r, A and T were selected so that $f = 0.2$. The frame of reference moves from left to right with the mean flow, and measures $10H$ in the streamwise direction.

by boils. Over the subsequent $7T$, boils begin to break up the plume, dispersing particles normal to the direction of general advection. In the final three frames, it can be seen that boils are now erupting within regions previously affected by boils, further dispersing and breaking up the plume.

The across-current displacement of each particle was recorded, and from this the diffusivity was calculated as before. It was found that there was no significant difference between calculating the diffusivity directly from the time that the particles had been dispersing, and from using their displacement distance down-stream of the release point as a measure of dispersion time - analogous to the method used in the dye-plume release measurements from the North Sea. Again, ensembles of 50 model runs each were made over a series of different values of r, A and T and for different relative drifts between the boils and the undisturbed particles. The mean non-dimensional diffusivities, $\mathbf{K_y}$, are plotted against the relevant rAT values in Figure 5.14. It can be seen that the values are nearly identical to those calculated from the dispersion of a patch of particles (Figure 5.11), which are again very similar to those actually measured from the dye-plume releases.

5.3 Conclusions

The analytical models and numerical simulations described above provide good estimates of the dispersion of buoyant material by bottom-generated turbulence. The first-order and subsequent, more conservative, analytical models provide estimates for the non-dimensional lateral diffusivity which cover the range of values as measured in the southern North Sea.

A relationship is found between the production rate of boils at the water surface, and quantities measurable within the sonar and aerial video observations, allowing the construction of numerical simulations. These simulations show qualitatively the patterns produced within a patch or plume of buoyant particles by the action of erupting boils. The particles are accumulated into dense filaments surrounding regions devoid of them. This accumulation occurs more rapidly when there is a relative drift

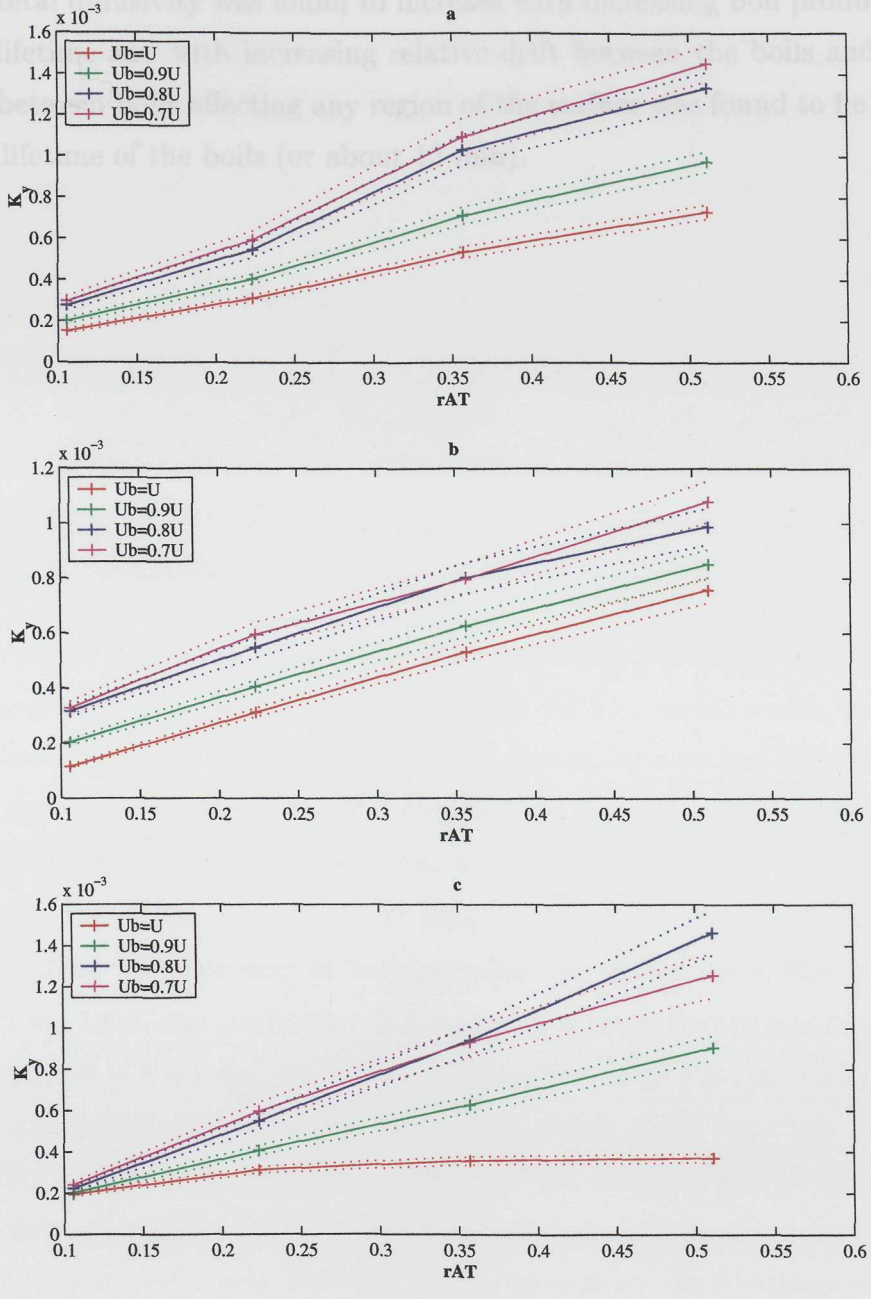

Figure 5.14: $\mathbf{K_y}$ vs. rAT varying r, A or T in **a**, **b** and **c** respectively. Dotted lines show the standard error of the ensemble mean value.

between the particles and the boils.

The lateral diffusivity was found to increase with increasing boil production rate, area and lifetime and with increasing relative drift between the boils and particles. The time between boils affecting any region of the surface was found to be about two times the lifetime of the boils (or about 13 min).

Chapter 6

Discussion and conclusions

6.1 Discussion

There is evidence that there are other processes to which the simple models of dispersion by Langmuir circulation may be applicable. At very small scales, wind aligned streaks - linear bands of accumulated material (foam, oil or other flotsam) - are observed at the water surface. Streaks observed at the water surface in laboratory observations by Melville et al. [1998] may be formed by coherent structures within the airflow above the water surface - as found in the numerical simulations of Lombadi et al. [1996]. The existence of 'low-speed streaks' within the airflow [for example Klewicki et al., 1995, and see Section 2.2] may also account for the small scale streaks observed to form in the foam left behind breaking waves by Thorpe et al. [1999]. It is possible that amalgamations of these streaks are visible as the fine-scale wind-aligned bands within the radius of the boils recorded by the sonars (Figure 4.7). At a larger scale, another process which may produce long streaks is introduced in Appendix A. Here, comparisons are made between recent laboratory observations of persistent vortices formed offshore of the surf zone on gently shelving beaches, and near-shore sonar observations. The sonar images show linear regions of accumulated bubbles, with lengths up to about 300 m, aligned with the shoreline. These regions would

act in a similar fashion to Langmuir circulation in the dispersion of buoyant material, by producing linear accumulations of material. However, it is clear that more observations are required to give a better understanding of these features and the environmental conditions under which they form. In addition, controlled dispersion experiments would allow estimates to be made of the importance of these processes in relation to other near-shore processes (for example rip-currents).

The observations of the boils are of great importance, not only because they show that turbulence generated by a current flow over a flat sea bed produces clearly definable structures at the sea surface which affect dispersion but also because they allow studies of dispersion to take a more mechanistic approach. This is important for estimating the local patterns and peak concentrations of any floating material. The simple models introduced in Chapter 5 give a first indication of this. A comparison between the numerical simulation of the dispersion of floating particles and aerial images of boils and oil is shown in Figure 6.1. From this it can be seen that even these simple simulations produce patterns which closely resemble those of oil released in the environment, with the formation of filaments of high concentrations of floating material in-between regions with relatively low concentrations. In addition, the break-up of a concentrated patch of particles in the simulation by an erupting boil is very similar in appearance to the break-up of the oil (arrowed), with material, previously accumulated by the actions of boils, being spread out radially around a newly erupting boil.

It is possible that further information may be available from the CASI images, since they not only show the fractional coverage of the water surface by the oil, but also give information as to its thickness. Therefore a more detailed quantitative study would provide information on, for example, the mean size scales of the concentrated filaments which could then be compared more directly with the numerical simulations, and in turn related to the physical and chemical properties of the oil. This information could then be used in the assessment of how best to 'combat' an oil slick, whether by mechanical recovery or by the use of chemical dispersants, and to estimate the potential threat the slick may pose to wildlife. Localised accumulations and filaments

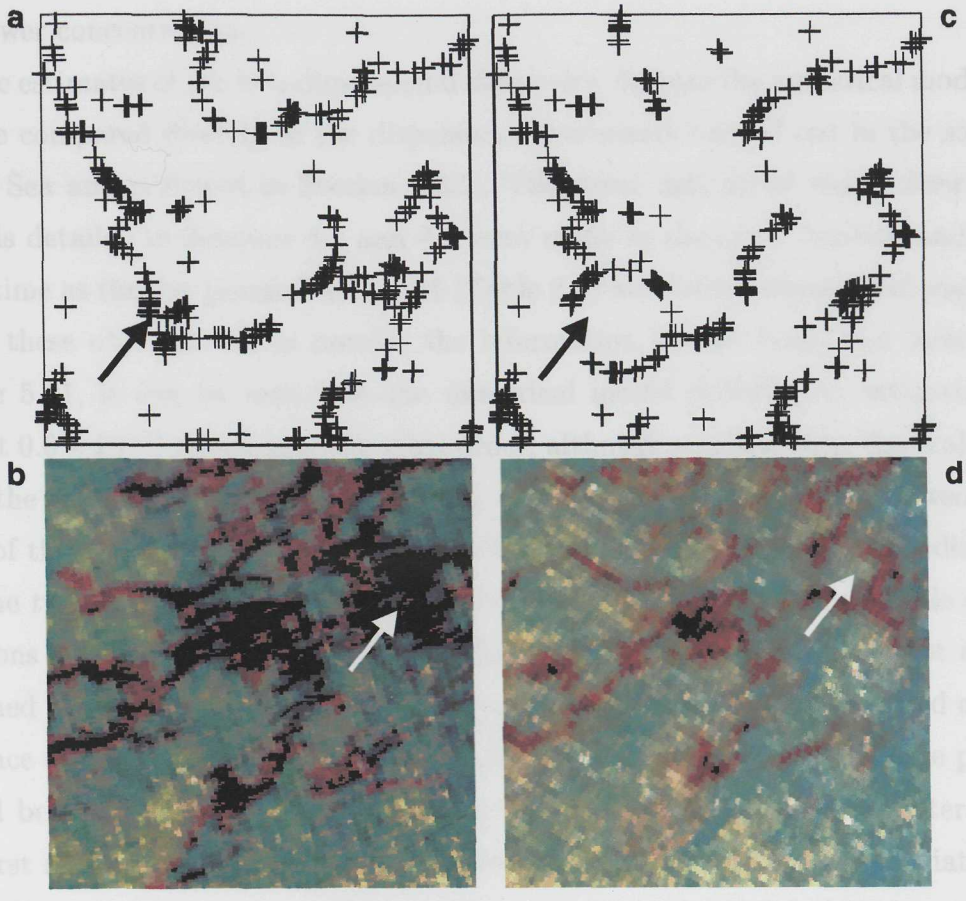

Figure 6.1: Comparison of model output (**a** and **c**) with CASI images (**b** and **d**). All the images are to the same scale and show an area $5H$ square where H is the diameter of the boils. The time between the two frames from the model simulation is T, the 'lifetime' of the boils, while the time between the two CASI images is about 5 min ($\sim 0.7T$). The arrow in each image points to the appearance of circular region within the particles (for the model simulations) or the oil (shown in red to black for the CASI images) in the time interval between the frames.

of oil, as produced by the boils (or indeed by Langmuir circulation), while being more toxic to individuals within a population (seabirds, for example) who may come into direct contact, may be less harmful to the population as a whole, since fewer individuals will come into contact than if the oil were spread over a wider area, albeit

at a lower concentration.

The estimates of the non-dimensional diffusivity, β, from the numerical models can also be compared directly to the dispersion experiments carried out in the southern North Sea and reviewed in Section 2.3.2. The sonar and aerial video observations of boils detailed in Sections 4.1 and 4.2 were made in the same location and at the same time as the dye plume Number 15 (Table 2.2) was being released and measured. Using these observations to provide the information for the boils, and referring to Figure 5.11, it can be seen that the numerical model provides an estimate for β (about 0.6×10^{-3}) which is of the same order, although smaller, than that calculated from the dye plume (about 1.48×10^{-3}). The differences need to be viewed in the light of the scatter within the dye concentration measurements previously discussed.

The two analytical models described in Section 5.1 included only simple approximations for the dispersive action of boils on floating particles. The first of these assumed that all particles within the perimeter of a boil would be displaced a lateral distance equal to the radius of the boil while the second, assumed that the particles would be spread radially, to form an even distribution about the perimeter. Thus, the first model probably provides an overestimate for the diffusivity associated with the boils, and the second an underestimate. However, the aerial video images of the initial eruption and evolution of boils in a plume of oil (Figures 4.9 and 4.10) provide some more detailed information on how floating material is dispersed. It can be seen that after the initial eruption and radial spreading of the boil, the combination of the differential flow between the boil and surrounding water and the formation of the pair of eddies acts to accumulate material at the upstream edge and to draw it in filaments around the perimeter. At the downstream edge, the pattern is less clear, with material initially spread out radially and accumulated at the perimeter of the erupting boil returning to the mean flow. Figure 6.2 shows how three particles with different initial locations (A_0, B_0 and C_0) relative to the centre of an erupting boil may be dispersed. It can be seen that initially, all three are spread out radially to the perimeter of the boil (Figure 6.2a). After the eddies form within the boil (Figure 6.2b), the particle pushed directly to the upstream edge remains trapped in the

convergence there (C_1), the particle pushed to the downstream edge (B_1) remains in position, unaffected by the circulation within the boil, until acted on either by the eruption of a new boil (see Figure 4.9E), or by the formation of Langmuir circulation (see below). At first, the particle with its initial position at A_0 is also pushed out radially to the perimeter of the boil to A_1 (with a lateral displacement of Δy_1), however it is then carried around the perimeter to A_2 by the circulation of the eddies, so increasing its lateral displacement (Δy_2). Therefore the diffusivity - or value for β - associated with the boils should fall between the two ranges of estimates given (Section 5.1, Pages 78 and 80), i.e. in the approximate range 1×10^{-4} to 1×10^{-3}. This is the same as the range of values measured in the southern North Sea (Table 2.2).

As discussed in Section 4.4, the scaling of the boils and eddies with Reynolds number remains unclear, with the features observed in the laboratory having relatively larger size scales (about $3H$) to those observed in the North Sea (about H). This has implications in the use of the value of β as measured in laboratory experiments, which is possibly greater than that expected in the presence of the relatively smaller boils in the environment. This effects the relative importance of Langmuir circulation and tidally generated turbulence as calculated in Section 3.3, such that the Langmuir circulation may be dominant in the dispersion of material at slightly lower ratios of wind to current speed. Also affected is the comparison made between the rough estimate of β from the observations of boils (see Section 5.1, Page 78). Here, a reduced value for the experimental β would fall directly within the range estimated from the North Sea observations.

The presence of boils in tidally well-mixed shallow seas appears to account for observations of relatively short cell durations in Langmuir circulation there. The aerial video images of a plume of oil being broken up by boils, shown in Figure 4.8, also indicates the existence of Langmuir circulation. Although the patterns of oil at the surface are dominated by the eruption of the boils, it can be seen that the fine scales bands, in-between the regions under the direct influence of a boil, are generally aligned with the wind direction. This shows that the two processes may co-exist, and that the instantaneous dispersion of material over scales of about H is controlled

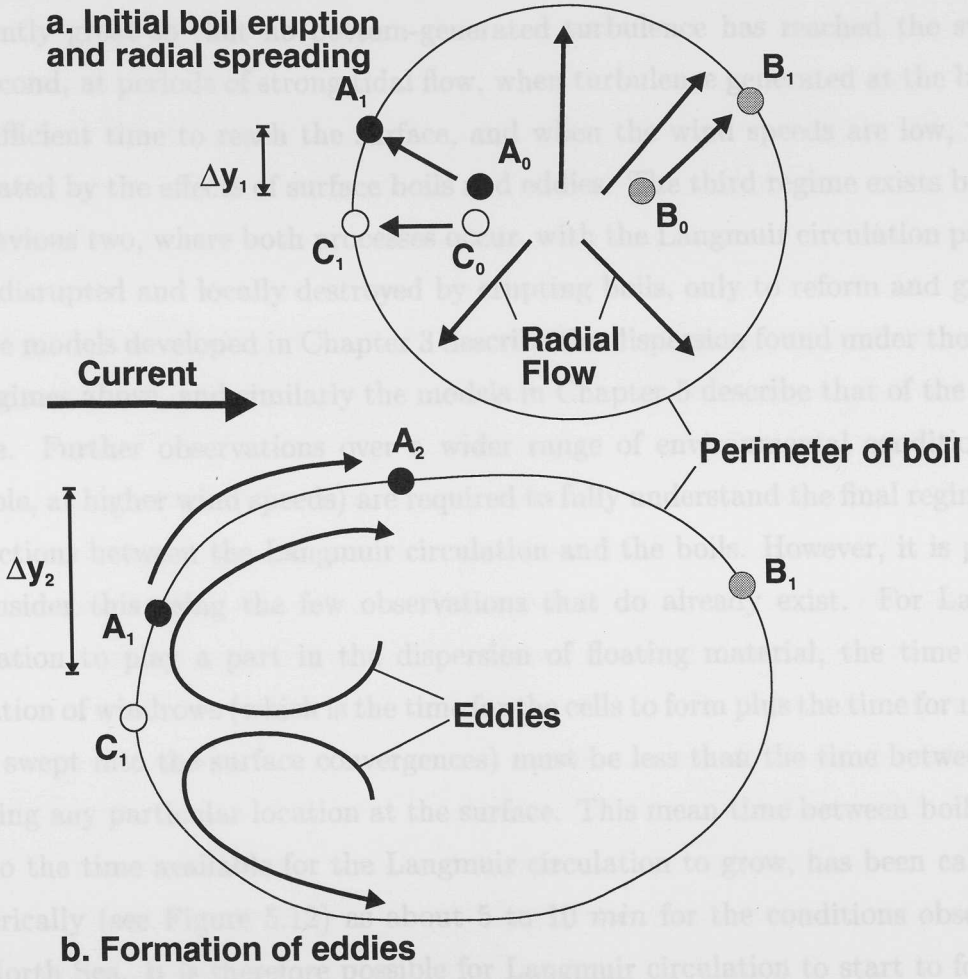

Figure 6.2: Dispersion of particles by a boil (see text for description).

by whichever process is dominant at that specific location and time. It is possible to classify three distinct regimes for the dispersion of floating material in shallow, well mixed seas. The first, that dominated by Langmuir circulation, occurs when the wind is sufficiently strong for the formation of the cells, and the tidal current is weak (at slack water, or during the early acceleration of the current) or the water depth sufficiently great so that no bottom-generated turbulence has reached the surface. The second, at periods of strong tidal flow, when turbulence generated at the bed has had sufficient time to reach the surface, and when the wind speeds are low, will be dominated by the effects of surface boils and eddies. The third regime exists between the previous two, where both processes occur, with the Langmuir circulation patterns being disrupted and locally destroyed by erupting boils, only to reform and grow.

The models developed in Chapter 3 describe the dispersion found under the first of the regimes above, and similarly the models in Chapter 5 describe that of the second regime. Further observations over a wider range of environmental conditions (for example, at higher wind speeds) are required to fully understand the final regime - the interactions between the Langmuir circulation and the boils. However, it is possible to consider this using the few observations that do already exist. For Langmuir circulation to play a part in the dispersion of floating material, the time for the formation of windrows (which is the time for the cells to form plus the time for material to be swept into the surface convergences) must be less than the time between boils affecting any particular location at the surface. This mean time between boil events, and so the time available for the Langmuir circulation to grow, has been calculated numerically (see Figure 5.12) as about 5 to 10 *min* for the conditions observed in the North Sea. It is therefore possible for Langmuir circulation to start to form and give a wind-aligned orientation to the streaks of oil, although it is probably unable to reach a fully developed state ($L = H$). This is also consistent with the observations of Thorpe et al. [1994] from this region of the persistence of windrows to be about $2 - 5$ *min*, especially when the time for material to reach the windrows and make them visible (proportional to L/u) is added to this.

Throughout this discussion, it has been clear that further observations of these

processes are required. Of particular importance are the forms of dispersion at high wind speeds, periods of extreme weather being when accidental releases of oil are most likely (for example the tanker *Braer* was wrecked during a period of storm-force winds). Side-scan sonar is a robust tool for the study of near-surface processes, and further experiments combining its use with modern Acoustic Doppler instruments and aerial observations would provide the data that is required. Very recently, optical techniques developed in the laboratory to measure the instantaneous flow structure over the area of a two-dimensional plane have been used successfully in coastal seas [Doron et al., in press]. These have the potential to study the development of turbulent structures, generated near to the sea bed, as they grow, move up through the water column and finally reach the surface. Measurements are possible over scales ranging from less than 1 mm to greater than 1 m, which, when combined with the acoustic methods, would provide a detailed picture of the entire water column in shallow tidal seas.

Numerical models will also be useful to further our understanding of these processes. Low Reynolds number studies [e.g. Tsai, 1998] have successfully shown the development of boils and eddies at the surface of sheared flows, while Large Eddy Simulations have been used to study Langmuir circulation in deep-water situations [Colbo and Li, 1999, Skyllingstad and Denbo, 1995]. To be useful, future studies will be required to resolve the small scales needed to allow the formation of the sub-surface structures which lead to the boils and eddies at the surface within a domain that is large enough for these structures to develop fully and then interact with other processes, Langmuir circulation for example. At present, this may be beyond the capabilities of current computer systems.

6.2 Conclusions

The results presented in the previous chapters both further our understanding of mixing processes at the sea surface and quantify the effects they have on the dispersion of floating material. The main findings are summarised below.

- The analytical model developed in Chapter 3 shows that Langmuir circulation contributes significantly to the lateral dispersion of buoyant material soon after it is released when: (a) the wind is sufficiently strong in comparison to the tidal current, (b) the angle, α, between the wind and current is between 30^o and 120^o, and (c) the Langmuir cells are sufficiently stable. The direction of the wind in relation to the current is important in controlling the lateral diffusivity.

- Langmuir circulation plays a dominant role in the lateral dispersion of a plume of floating material when the wind speed is over approximately 10 times the current speed and the angle between wind and current is greater than 30^o.

- Observations of the nature of bottom-generated turbulence at the sea surface and its effect on floating material (oil) are shown in Chapter 4. The dominant structures are boils, circular regions of upwelling water, with high concentrations of sediment and length scales similar to the water depth, which evolve into pairs of counter-rotating eddies. These boils and eddies are seen to disperse floating material, pushing it radially outwards to their perimeters.

- A study is made of the dispersion of floating material by these boils in Chapter 5. Analytical studies and numerical calculations show that the presence of boils alone can account for the dispersion of plumes of material measured in shallow tidal seas.

- These studies have also shown that the patterns of floating particles observed both in the numerical simulations and the aerial images bear a close resemblance to one another.

It is anticipated that the parameterisations for the dispersion of material by Langmuir circulation and bottom-generated structures developed here will have applications in numerical simulations of oil spills as well as other contaminants, such as effluent from dump sites and outfalls.

Appendix A

A note on dispersive processes in shallow water just beyond the surf zone

Close to the shoreline, many other factors will influence the dispersion of material, such as the tidal flow around topography, circulation patterns related to regions of freshwater influence and variations in the wind forcing caused by the proximity of the land. Most of these processes are outwith the scope of this study, principally giving additional variability to the coherent patterns of dispersion described in the previous chapters.

However, recent laboratory observations have revealed the presence of a near-shore coherent process which may produce a pattern of dispersion to which the simple models developed in Chapter 3 may be applicable. Some near-shore side-scan sonar measurements show evidence of the existence of the process 'in the field'. The observations of this process - "the offshore vortex train" - are presented briefly in the following sections.

A.1 Laboratory observations of the offshore vortex train

Wave breaking against a shoreline usually results in the formation of a near-shore circulation pattern which is made up of longshore and cross-shore currents. The cross-shore currents are either the spatially localised and short-lived rip-currents or more prolonged drift-currents. These latter currents consist of the onshore mass transport of water towards the shore (Stokes' Drift) and the so-called "undertow", which returns the water offshore. Experiments carried out by Bagnold [1947], later confirmed in an analytical study by Longuet-Higgins [1953], show that the on-shore drift current is found near to the bed and the off-shore return flow is close to the surface, at about the height of the wave troughs.

In a series of laboratory experiments, Matsunaga et al. [1989, 1994] observed that a row of vortices forms offshore of the surf zone as waves approach a sloping beach, which they termed "the offshore vortex train". The experiments were carried out in a narrow wave tank: 12 m long, 0.4 m deep, 0.15 m wide and equipped with a sloping planar bed. They observed that a single layer of large (order wave height) eddies were formed, slowly rotating about a horizontal axis parallel to the shoreline (for example Figure A.1). The eddies rotate in the opposite direction to the orbital wave motion and were observed to migrate slowly offshore, at a velocity less than that of the undertow. After moving into water of greater depth, they decayed quickly. Adjacent vortices were observed to combine, so increasing the spacing between neighbours. Li and Dalrymple [1998] repeated the experiments in a larger wave tank (35 m long, 0.6 m deep and 0.6 m wide). They observed similar features to the earlier experiments but also a second layer of vortices, smaller, closer to the surface and rotating in the opposite direction to the main vortices, but again moving slowly offshore.

Matsunaga et al. [1989, 1994] investigated the conditions under which the offshore vortex train was observed to form. They found that the vortices formed irrespective of breaker type (plunging or spilling) when $H_0/L_0 \lesssim 4.2 \times 10^{-2}$, where H_0 and L_0

Figure A.1: Photograph of the offshore vortex train from Matsunaga et al. [1994]. The photograph is a side view of the wave tank with the waves propagating from right to left. The breaking point was 1.68 m shoreward (to the left) of the left-hand vertical bar. The vertical bars are 0.5 m apart, the mean water depth is about 13 cm and the slope of the bed is about 1.5^o. Water soluble aniline blue dye was used to visualise the flows.

are the deep-water wave height and wave length respectively. The combined results from their experiments are shown in Figure A.2, with the angle of incline of the beach given by θ, and the open symbols showing when the offshore vortices formed. H and L are the local wave height and wave length respectively, while h is the still water depth. Line (a) shows the upper limit of wave steepness, the breaking point, line (b) is where $H_0/L_0 = 4.2 \times 10^{-2}$, and line (c) marks both the offshore limit and the lower threshold of wave steepness for the formation of the vortices.

The laboratory experiments of Li and Dalrymple [1998] showed that the vortices migrate offshore at a velocity which was about 0.5% of the surface wave phase speed, whilst the time for a complete rotation of an individual eddy was about 10 times the surface wave period. Matsunaga et al. [1989, 1994] found empirical relationships for the between-vortex spacing, l and the offshore migration velocity, u:

$$l/h = 1.2 \times 10^{-2} (\tan\theta)^{-1/3} (H/L)^{-1}, \tag{A.1}$$

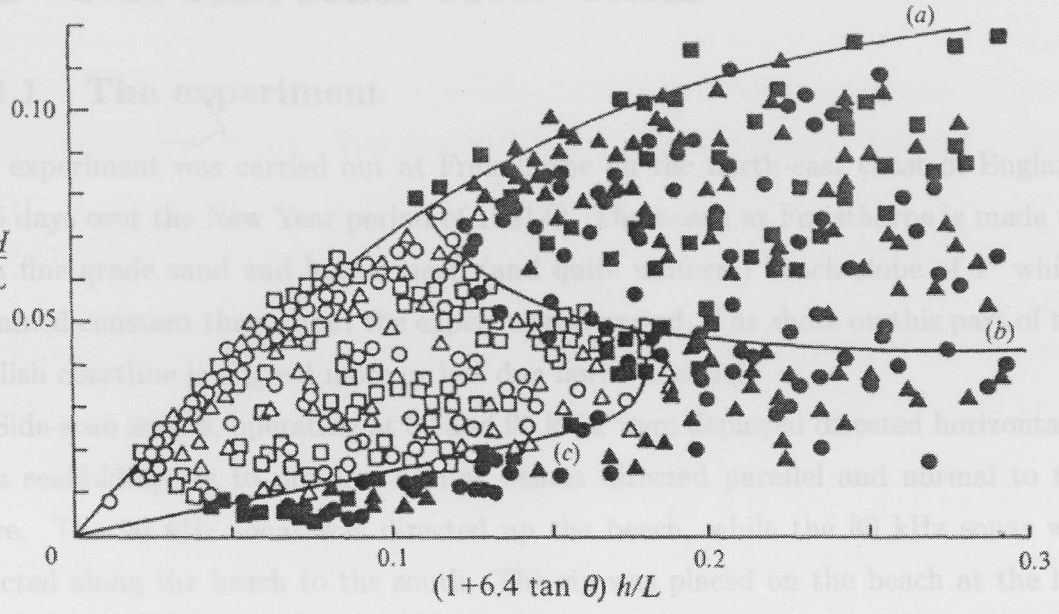

Figure A.2: Formation regions of offshore vortices from Matsunaga et al. [1994]: open symbols, formation of offshore vortex; solid symbols, non-formation. Squares: $\theta = 1.56^o$; Circles: 2.44^o; Triangles: 4.65^o. Lines (a) and (b) indicate the limit of wave steepness and $H_0/L_0 = 4.2 \times 10^{-2}$, respectively. Line (c) is the offshore border of vortex formation.

and

$$u/U_{max} = 3.6 \times 10^1 (\tan\theta)^{2/3} (h/L) \tag{A.2}$$

where U_{max} is the maximum offshore velocity of the undertow.

Matsunaga et al. [1989, 1994] postulated that the offshore vortex train occurs owing to a shear instability between the onshore and offshore drift currents. This conclusion was confirmed by the analytical and numerical studies of Li and Dalrymple [1998]. The latter authors found that the instabilities formed in the regions of maximum shear in the current profile, and that either one or two layers of vortices would form depending upon the mean velocity profile. The offshore limit of the vortex train occurs where the mean current profile becomes linear, preventing the growth of any perturbations which might lead to the formation of vortices.

A.2 Side-scan sonar observations

A.2.1 The experiment

The experiment was carried out at Fraisthorpe on the north-east coast of England for 5 days over the New Year period of 1991/2. The beach at Fraisthorpe is made up from fine grade sand and had a mean (and quite uniform) beach slope of 1^o which remained constant throughout the experimental period. The shore on this part of the English coastline is aligned more or less due north to south.

Side-scan sonars, operating at 80 and 90 kHz, were deployed directed horizontally on a scaffolding rig to produce narrow beams directed parallel and normal to the shore. The 90 kHz sonar was directed up the beach, while the 80 kHz sonar was directed along the beach to the south. The rig was placed on the beach at the low tide mark, to be covered to a depth of about 3.2 m by the M2 dominated tide. Data was recorded over almost seven consecutive tidal cycles. A more detailed account of the experimental set-up is given by Thorpe and Hall [1993].

Wind speeds ranged from 2 $m\ s^{-1}$ to 15 $m\ s^{-1}$, gusting to 19 $m\ s^{-1}$. Winds were initially from the south until they backed to the south-west during the second day, where they remained for the rest of the experiment. Wave heights and periods were estimated visually and range from 0.15 m to 0.9 m in height with periods of 3.7 to 5.8 s.

A.2.2 The observations

Various features were observed within the sonar data. Individual waves and wave groups and small-scale wind-aligned Langmuir circulation were all observed. The so-called "acoustic-wall" [Thorpe and Hall, 1993] was also visible throughout the experiment. This is a narrow region of strong acoustic backscatter at the outer edge of the surf-zone, present because of the high concentrations of suspended sediment and bubbles stirred up and produced by the waves as they break, and beyond which it is not possible for sound to penetrate. The acoustic wall is clearly visible as the

continuous dark band at a range of between $80 - 100\ m$ in the sonograph of the sonar pointing up the beach shown in Figure A.3a. It can be seen that it occasionally abruptly moves closer to the sonar (for example at 'A'), this because a wave, or group of waves, breaks in deeper water (i.e. closer to the sonar) than previously. Further features of the wall are investigated by Thorpe and Hall [1993]. Closer to the sonar, it can be seen that there are very few strong acoustic targets, this because the wind speed was low (about $4.5\ m\ s^{-1}$) and directed offshore - giving a short fetch - leading to a scarcity of bubble-producing breaking waves. Also, there is a lack of any coherent circulation patterns (for example Langmuir circulation) which might have led to the accumulation of any bubbles that may have been present.

In striking comparison are the obvious linear bands of high acoustic backscatter seen in the record from the up-beach sonar as shown in Figure A.3b (for example at 'B'), which were visible for three of the seven tidal cycles. The mean up-beach spacing of the bands is $14 \pm 4\ m$, and they were found to persist for in excess of $17\ min$ which equates to an along-shore length of over $300\ m$ (in an along-shore current of about $0.31\ m\ s^{-1}$). The bands *appear* to migrate onshore at a velocity of about $0.08\ m\ s^{-1}$. Making the assumption that the bands are linear features with no motion in the up-beach direction, their orientation is found to be about 14^o to the right of the direction of the shoreline. For this period they are also about 38^o to the left of the wind direction and about 19^o to the left of the orientation of the wave crests close to the sonar rig. The small-scale bands (Figure A.3b, 'C') have an orientation which is about 16^o to the left of the wind direction. These orientations are summarised in Figure A.4.

There remains some uncertainty in the orientation of the bands relative to the shoreline. As stated, it is assumed that the bands do not have any motion in the up-beach direction. However, if the bands were being advected onshore by the rising tide, their orientation would have to be closer to parallel to the shoreline to give the same orientation as observed in the sonographs. Similarly, if the bands were slowly migrating offshore, their orientation would actually be closer to that of the crests of the incident surface gravity waves.

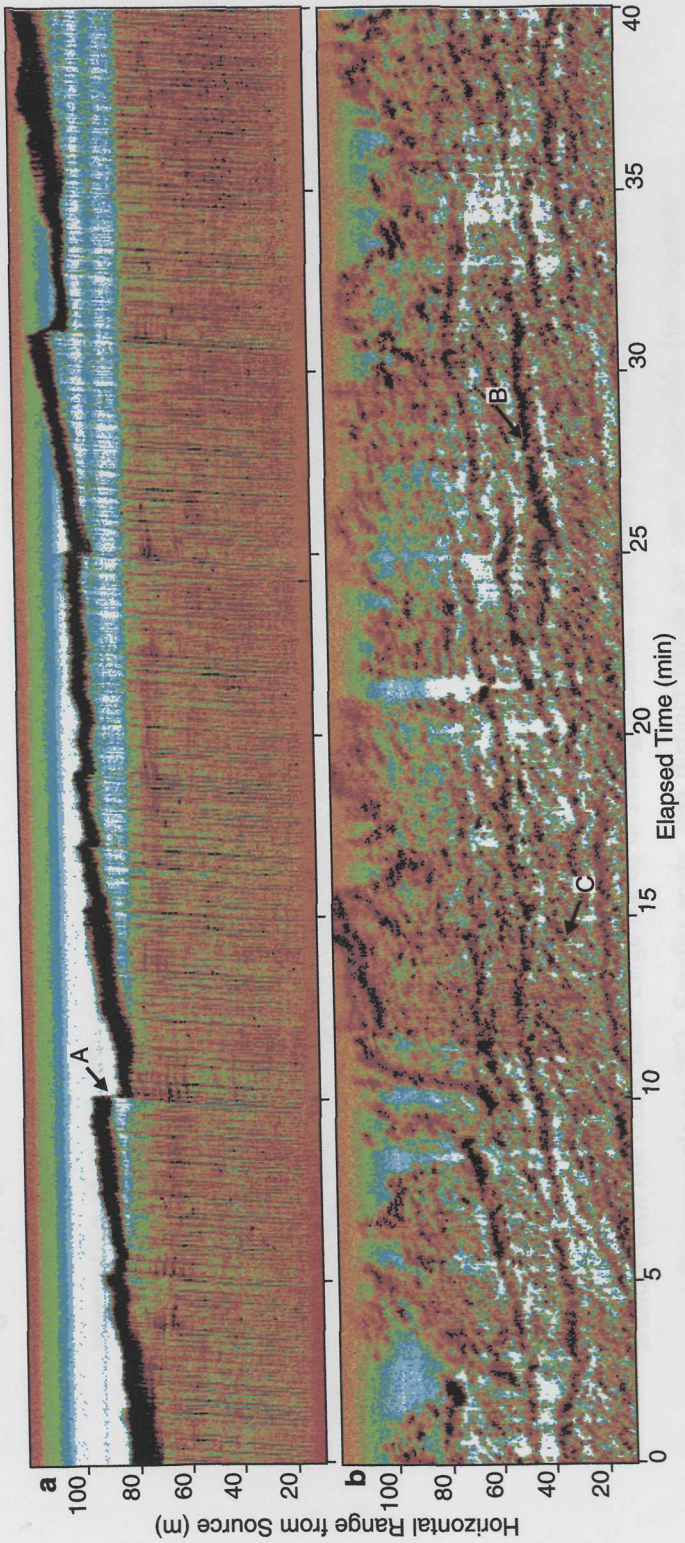
a
b
A
B
C
Horizontal Range from Source (m)
Elapsed Time (min)
0
5
10
15
20
25
30
35
40
20
40
60
80
100

Figure A.3: (previous page) Sonographs from the sonar directed up the beach. The shoreline is at a range greater than $100\ m$. Each one shows a $40\ min$ period, and has been corrected for the attenuation of sound with range. Dark colours represent regions of high acoustic backscatter. **a** The along-shore current is about $12\ cm\ s^{-1}$ to the south, the wind is about $4.5\ m\ s^{-1}$ from about 240^o. The thin vertical bands are reflections from surface gravity waves, of period about $5\ s$ and height of about $0.3\ m$. The "acoustic wall" is clearly visible as the narrow region of high acoustic backscatter, slowly moving inshore with the rising tide, away from the sonar. Occasionally, the range to the acoustic wall decreases sharply (for example at 'A') when a wave breaks further offshore than before. The surf zone lies beyond this wall. **b** The along-shore current is about $31\ cm\ s^{-1}$ to the north, the wind is about $15\ m\ s^{-1}$ from about 220^o. The surface gravity waves are of about $5\ s$ period and $0.8\ m$ height. The acoustic wall is broken and indistinct, although it is visible at an elapsed time of about $15\ min$, again moving slowly onshore with the rising tide. Large bands of strong acoustic backscatter are visible closer to the sonar (for example at 'B'). Smaller scale, less distinct bands are also discernable (for example at 'C')

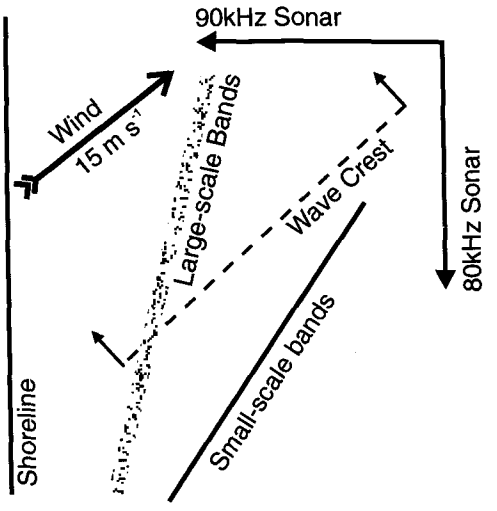

Figure A.4: Sketch of the orientations of the features seen in Figure A.3b.

The small-scale bands are most probably produced by the accumulation of bubbles in the convergences found between neighbouring wind-aligned Langmuir cells and as such are comparable to the banded structures seen in Figure 4.4. They have an up-beach separation of about 9 m, so that the spacing between neighbouring windrows is about 4.6 m. They have a maximum along-shore length of about 40 m.

The large-scale scale banding are again most probably regions of accumulated bubbles trapped within the 'retention zones' of larger scale vortices [Stommel, 1949]. Taking the orientation of the bands into account, the spacing between the bands is about 13 m, slightly less than the wavelength, about 15 m (measured from the sonar images), of the surface gravity waves close to the sonar rig.

Figure A.5 shows further examples of the large-scale bands. Here the images, from two separate tidal periods, have been scaled and displayed according to the alongshore current, so that they both show the same alongshore distance (400 m) and the alignment of the bands relative to the direction of the shore is correct. In both cases, it can be seen that the bands are more well defined in the region closer to the shore, and become less distinct close to the sonar rig (towards the bottom of the images).

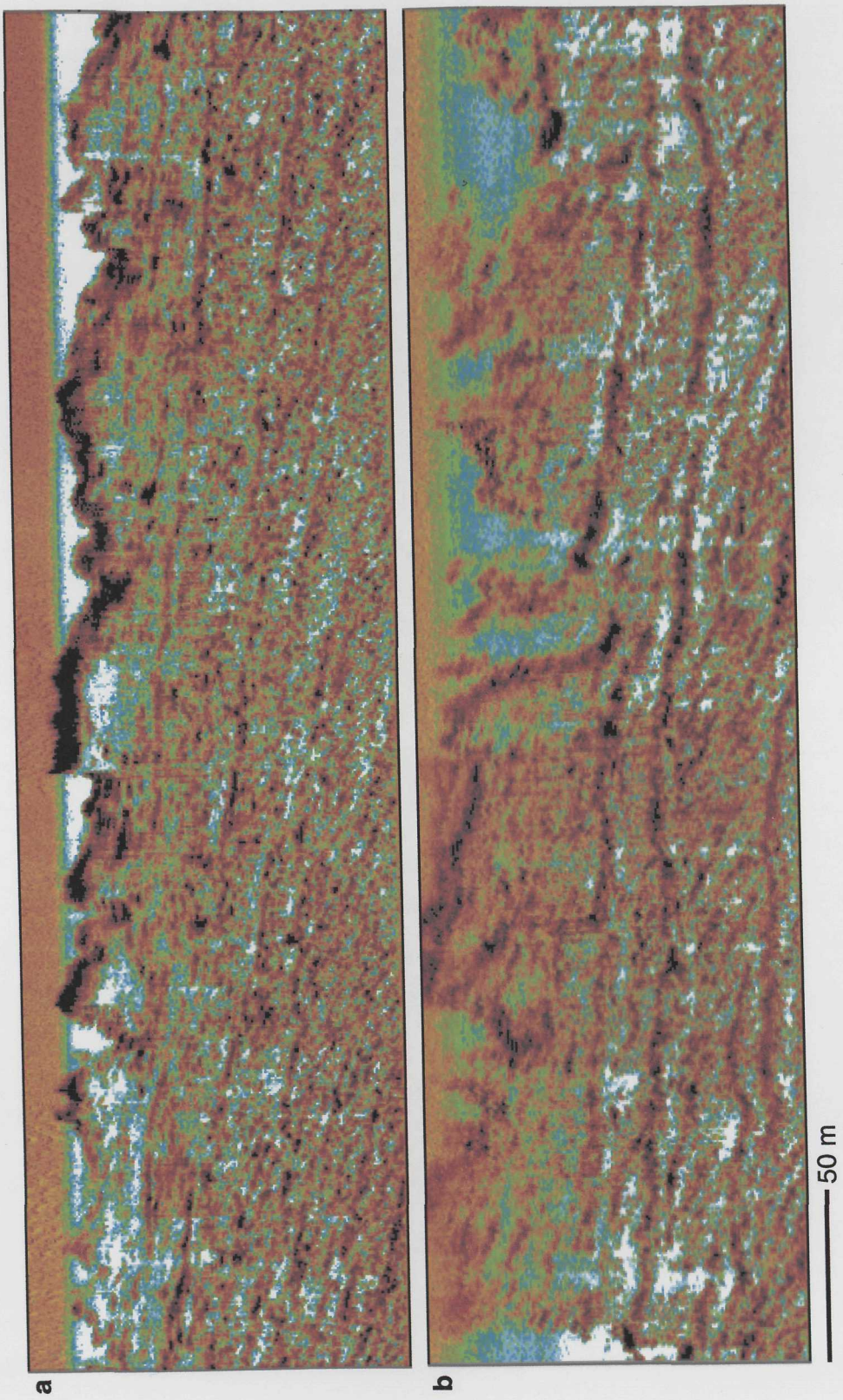
a
b
50 m

Figure A.5: (previous page) Sonographs from the sonar directed up the beach showing the large scale bands. Each image is from a different tidal period and has been scaled according to the alongshore current, so that they represent the same alongshore distance. The x and y axes are to the same scale. The bottom edge of the images is at a distance of $10\ m$ from the sonar rig, and the near-shore acoustic wall is visible near the top. The images have been presented so that the alongshore current is from left to right, and so the bands are shown in approximately their correct orientations relative to the shoreline.

A.2.3 Interpretation

It is proposed that the bands, or regions of accumulated bubbles, are formed by the existence of the offshore vortex train as discussed in Section A.1. Figure A.6 shows the approximate regions (calculated for a water depth, h, of 2 m) of vortex formation where the sonar observations lie in comparison to those of Matsunaga et al. [1994]. Regions marked 'D' and 'E' correspond to the sonographs shown in Figure A.5b and A.5a respectively. Region 'F' corresponds to the sonograph shown in Figure A.3a, and 'G' to a similar, but separate, period where no large-scale bands were evident, although the smaller bands produced by Langmuir circulation were in existence. It can be seen that the region marking the time when the bands were most obvious ('D') lies almost centrally within the region that the offshore vortex train was observed to form in the laboratory. The region, 'E', corresponding to less distinct bands seen in Figure A.5a is close to the limit of vortex formation where the mean current profile becomes linear and insusceptible to perturbations. Region 'F' (Figure A.3) falls well outside of this limit, whilst region 'G' is below the threshold wave steepness required for vortex formation.

The difference between the horizontal spacing of the vortices in the laboratory (about $2h$) and in the sonar observations (about $6h$) remains unexplained. It may be that this difference is because the laboratory observations were all carried out with the waves approaching normal to the shore. More observations, both in the laboratory and from beaches will clarify this.

A.3 Conclusions

While it is clear that further beach observations are necessary - both in different locations with varying beach slope and under a range of environmental conditions - there is evidence in the existing data of the presence of a coherent process, different to the small scale and relatively short lived Langmuir circulation, which leads to the formation of the persistent large-scale bands. It has been proposed that the bands

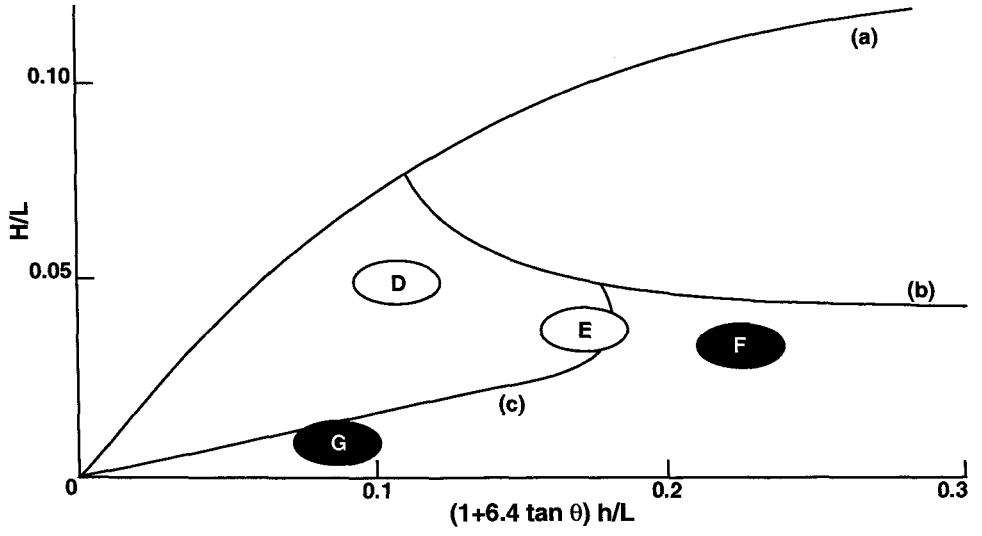

Figure A.6: Approximate formation regions of the large-scale bands from the beach experiment. Open regions ('D' and 'E') indicate the formation of the bands and solid regions ('F' and 'G') are examples from periods when no bands were evident. Lines (a) to (c) are as for Figure A.2.

mark accumulations of bubbles trapped within an offshore vortex train. A cartoon of the arrangement is shown in Figure A.7. The bands have an orientation which lies between the direction of the shoreline and the incident surface gravity waves.

Whatever the forcing mechanism, the fact that bubbles are observed to accumulate, indicates that this process is important in the dispersion of buoyant material in the near-shore region. If a plume of material was released into this flow structure, from an outfall for example, it would be possible to use the simple model described in Section 3.2 to estimate the rate of its dispersion relative to the direction of the mean alongshore current.

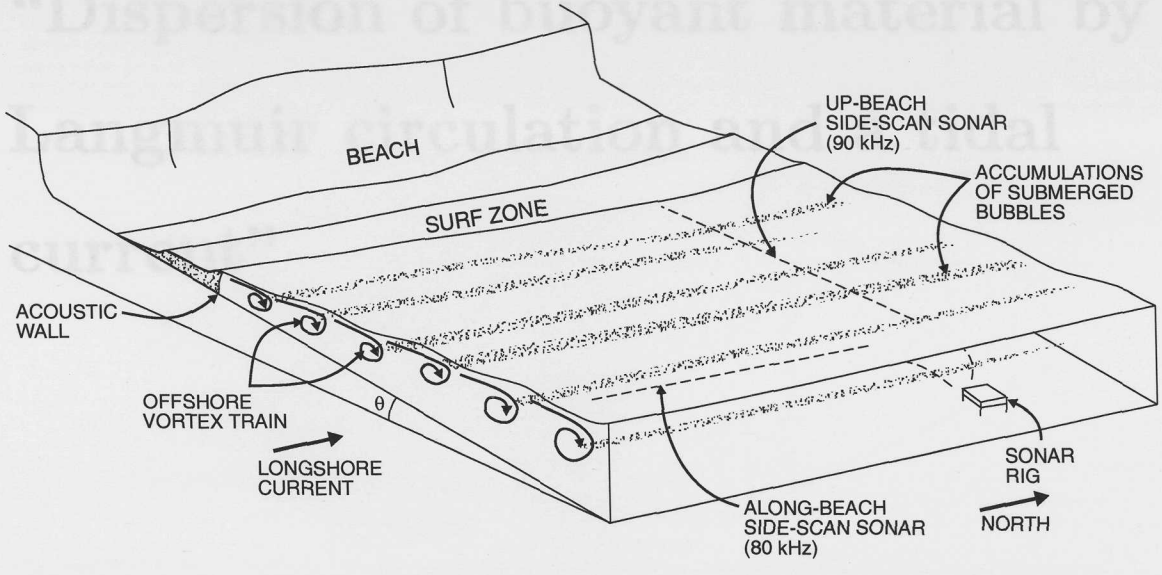

Figure A.7: Sketch of the equipment orientation and the offshore vortex train which produced the large-scale banding during the beach experiment.

Appendix B

"Dispersion of buoyant material by Langmuir circulation and a tidal current"

Dispersion of Buoyant Material by Langmuir Circulation and a Tidal Current

W.A.M.Nimmo Smith and S.A.Thorpe
School of Ocean and Earth Science, Southampton Oceanography Centre,
European Way, Southampton SO14 3ZH, UK.

Marine Pollution Bulletin, **38**, 824-829.

An analytical model is developed which quantifies and describes the dispersion of buoyant material caused by wind and wave generated Langmuir circulation in a tidal flow. It is found that the angle between the orientation of the Langmuir bands, taken to be in the wind direction, and the current controls the lateral (across-current) dispersion. Largest values of the dispersion occur when the wind and current are almost perpendicular and the wind is strong relative to the current. The lateral diffusivity caused by Langmuir circulation is compared with that produced by a current alone, and it is shown that the dispersive effects of Langmuir circulation will usually dominate when the wind speed exceeds about 50 times the current.

Langmuir Circulation and Dispersion

On windy days it is often possible to observe long streaks of foam, oil or other debris, floating at the surface of large bodies of water. These streaks are produced by the wind-driven process of Langmuir circulation. It is now generally accepted that Langmuir circulation is driven by a vortex force produced by a combination of waves and drift currents (Leibovich, 1983) which leads to the observed pattern of horizontal, parallel, helical vortices of alternating sign with axes aligned within 30° of the wind direction (Fig 1). At the sea surface, these vortices produce alternate regions of convergence, with associated downwelling, and divergence, associated with the upwelling of water. Buoyant material, foam, oil or other flotsam, is swept across-wind towards the regions of convergence leading to the formation of windrows. In shallow seas, the spacing between adjacent windrows is typically 5 - 30 m, while the vortices may extend to depths of 5 - 15 m. In the open ocean,

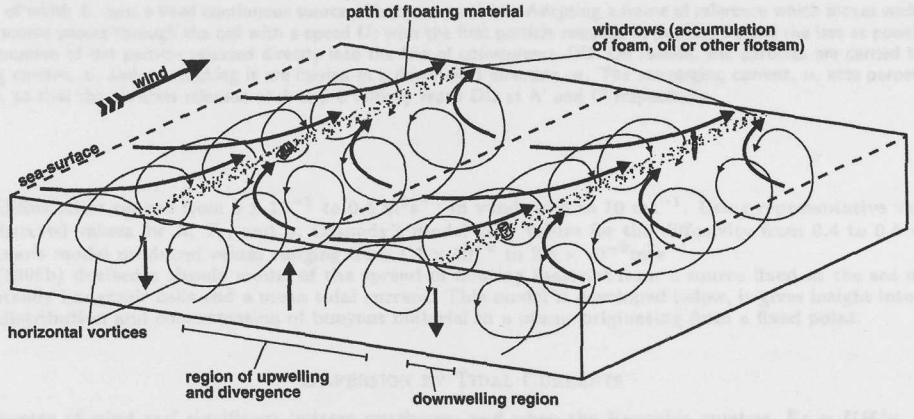

Figure 1 Schematic diagram of Langmuir circulation and its effect on floating material.

Faller and Woodcock (1964) found that there was a significant correlation between the mean crosswind separation of the windrows, L, and the windspeed, W, taking it to be $L = (4.8\text{s}) \times W$, while Graham and Hall (1997) found the relation to be $L = (0.68\text{s}) \times W + 1.2\text{m}$, using measurements taken in a shallow sea. Filatov et al. (1981) found that the convergence currents, u, within the Langmuir cells were typically 3% of the windspeed. The down-wind flow of the surface water in the windrows, v, is greater than between them (e.g. Katz et al., 1965; Kenney, 1977; Langmuir, 1938) and has been observed to be about equal to u (Leibovich, 1983). Observations of Langmuir circulation in the North Sea by Graham and Hall (1997) show the ratio of windrow spacing to the water depth to be between 0.3 and 0.5. These values are typical of fetch limited, shallow seas where cells may not be fully developed, so the values for the ratio are less than those reported by Leibovich (1983) of between 0.66 and 1.66.

On reaching the windrows the material remains trapped until such a time as the local circulation breaks up, perhaps when adjacent cells merge together. Studies by Csanady (1973), Faller and Auer (1988) and Thorpe (1992) have focused on this mechanism for the dispersion of material relative to the wind direction. Csanady (1973) identified the time, T_*, that Langmuir cells exist before breaking down as being critical in determining the across-wind diffusivity. This across-wind diffusivity was simply defined as $K = L^2/T_*$. Faller and Auer (1988) produced a more complex model which included the effects of the windrows meandering, finding that $K = 0.5(u/k^3T_c)^{1/2}$, where T_c is the characteristic timescale for the Langmuir circulation, estimated as $L/0.03\ \text{ms}^{-1}$, u is the speed of convergent motion, and k is the wavenumber of the cells, $k = 2\pi/L$. Based on an analytical model of cell interaction and break-up, Thorpe (1992) predicted that $T_* = cL/u$ where c is a constant. Observed values of T_* are about 10 - 30 min.

Thorpe et al. (1994) approximated the lateral diffusivity, relative to the mean tracer flow, using a numerical simulation of the motion of particles released into a "frozen field" of windrows defined by side-scan sonar data taken in the southern

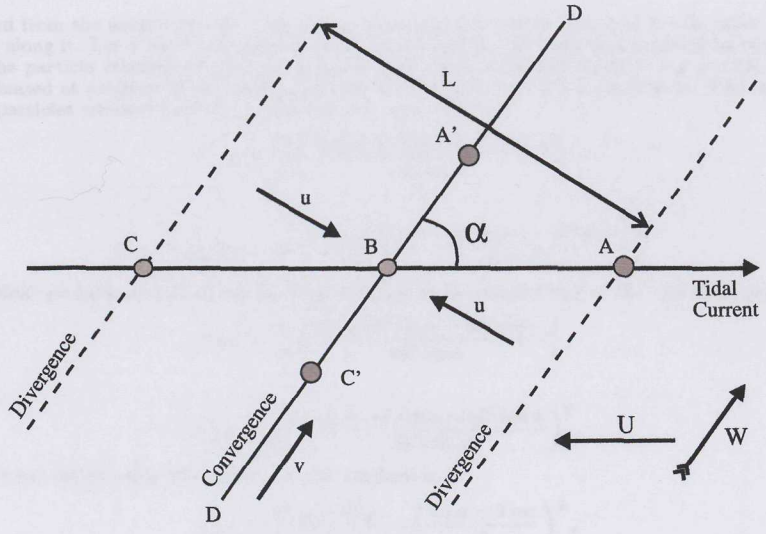

Figure 2 Components of the simple model of a windrow. The longitudinal axis of the Langmuir cell, the region between two neighbouring divergences, is aligned parallel to the wind, W, which is at an angle, α, to the left of the mean current. This mean current advects a stable Langmuir cell, of width L, past a fixed continuous source of buoyant particles. Adopting a frame of reference which moves with the Langmuir cell, the fixed source passes through the cell with a speed U, with the first particle released at position A, and the last at position C. Position B marks the location of the particle released directly into the line of convergence DD. On release, the particles are carried towards DD by the converging current, u, and on reaching it are carried in a down-wind direction, v. The converging current, u, acts perpendicular to the wind direction, so that the particles released at A and C initially reach DD at A' and C' respectively.

North Sea. Diffusivities ranged from 5×10^{-3} to 0.5 m^2s^{-1} in winds of 5 to 10 ms^{-1}. Using representative values for wind speed and observed values for L, T_*, and u, Csanady's model gave values for the diffusivity from 0.4 to 0.5 m^2s^{-1}, while Faller and Auer's model produced values ranging from 1.7×10^{-2} to $2.6 \times 10^{-2} m^2s^{-1}$.

Thorpe (1995b) devised a simple model of the spread of floating material from a source fixed at the sea surface in the presence of steady Langmuir cells and a mean tidal current. This model is developed below, it gives insight into observations of the local distribution and concentration of buoyant material in a plume originating from a fixed point.

Dispersion by Tidal Currents

In the absence of wind and significant bottom roughness, and when the Reynolds number, $Re = UH/\nu$, is very large, dispersion is characterised by a dimensionally correct combination of two dimensional quantities, the tidal current U and water depth H, and is independent of kinematic viscosity, ν. Bowden (1965) parameterised the horizontal diffusion coefficient in the presence of tidal currents by using the expression, $K_T = \beta UH$, where β is a constant. Experimental values of β for the lateral (across-current) diffusivity, K_{yT}, calculated from dye releases during periods of low wind speed range from 1×10^{-3} (Morales et al., 1997) to 0.19 (Bowles et al., 1958). Fischer (1973) reports laboratory experiments on the lateral dispersion of buoyant particles, from which a mean value of $\beta = 0.025 \pm 0.013$ is found. These measurements were however taken at only moderate Reynolds numbers ($Re = 1.6 \times 10^4$ to 1.8×10^5). No obvious scaling of β with Reynolds number is found. From experiments in the English Channel at $Re = 1.4 \times 10^7$, Bowles et al. (1958) report similar values of β for floating particles in low winds, ranging from 4×10^{-3} to 1.15×10^{-2}.

The model

The objective is to develop an analytical model to quantify and describe how Langmuir circulation produces dispersion in a steady tidal current, U. Components of the model are shown in Fig 2. Buoyant particles are released continuously from a fixed source into a Langmuir cell as it is advected past by a mean current. The Langmuir cell of width L, here defined as the region between two neighbouring divergent regions, is aligned with the wind, W, at an angle, α, to the direction of the current. In a frame of reference moving with the mean current, the source of buoyant particles moves through the cell with a speed U. The first particle to be released is at A, the last at C, and that released directly into the convergence line, DD, is at B. On release the particles are supposed to converge towards DD at speed u, perpendicular to the wind direction, and on reaching it move downwind at a speed v. The time, T_D, for all the particles released from the source between A and C to reach DD as it is advected past is given by

$$T_D = \frac{L(2u + U \sin\alpha)}{2uU \sin\alpha} \tag{1}$$

The particles released from the source into the cell as it is advected past between A and B will, after reaching DD, have a uniform distribution along it. Let x be the distance from B of particles on DD after being carried by the converging currents for the time T_D. The particle released at position A has a final position on DD equal to $x_A = L(2v + U\cos\alpha)/2U\sin\alpha$, while the particle released at position B has a final position of $x_B = vL(u + U\sin\alpha)/2uU\sin\alpha$. The mean final position on DD of the group of particles released between A and B is $(x_A + x_B)/2$ or

$$\overline{x}_{AB} = \frac{L}{4}\left(\frac{3uv + vU\sin\alpha + uU\cos\alpha}{uU\sin\alpha}\right) \tag{2}$$

and its variance is

$$\sigma^2_{AB} = \frac{1}{12}(x_A - x_B)^2 = \frac{L^2}{48}\left(\frac{vu + uU\cos\alpha - vU\sin\alpha}{uU\sin\alpha}\right)^2 \tag{3}$$

Similarly the mean final position on DD of the particles released as the second half of the cell (BC) passes the source is

$$\overline{x}_{BC} = \frac{L}{4}\left(\frac{uv + vU\sin\alpha - uU\cos\alpha}{uU\sin\alpha}\right), \tag{4}$$

and its variance is

$$\sigma^2_{BC} = \frac{L^2}{48}\left(\frac{uv + vU\sin\alpha + uU\cos\alpha}{uU\sin\alpha}\right)^2. \tag{5}$$

The variance of the total distribution of particles in the windrow is

$$\sigma^2_{AC} = \frac{\sigma^2_{AB} + \sigma^2_{BC}}{2} + \left(\frac{\overline{x}_{AB} - \overline{x}_{BC}}{2}\right)^2, \tag{6}$$

and the across-current variance is $\sigma^2_y = \sigma^2_{AC}\sin^2\alpha$, so, using (2), (3), (4), (5) and (6),

$$\sigma^2_y = \frac{L^2}{48}\left(\frac{4u^2v^2 + 8u^2vU\cos\alpha + 4u^2U^2\cos^2\alpha + v^2U^2\sin^2\alpha}{u^2U^2}\right). \tag{7}$$

The lateral (across-current) diffusivity produced by the Langmuir circulation, defined as $K_{yLc} = \sigma^2_y/2T_D$, is

$$K_{yLc} = \frac{L\sin\alpha}{48(2u + U\sin\alpha)}\left(\frac{4v^2u^2 + 8vuU\cos\alpha + 4u^2U^2\cos^2\alpha + v^2U^2\sin^2\alpha}{uU}\right). \tag{8}$$

Non-dimensionalising with respect to variables, W and L, determined by the wind forcing, so that $\mathbf{U} = U/W$, $\mathbf{u} = u/W$, $\mathbf{v} = v/W$ and $\mathbf{K_{yLc}} = K_{yLc}/LW$, gives

$$\mathbf{K_{yLc}} = \frac{(4\mathbf{v}^2\mathbf{u}^2 + 8\mathbf{v}\mathbf{u}^2\mathbf{U}\cos\alpha + 4\mathbf{u}^2\mathbf{U}^2\cos^2\alpha + \mathbf{v}^2\mathbf{U}^2\sin^2\alpha)\sin\alpha}{48\mathbf{u}\mathbf{U}(2\mathbf{u} + \mathbf{U}\sin\alpha)}. \tag{9}$$

If $\mathbf{u}$ and $\mathbf{v}$ are constants (i.e. u and v are constant fractions of the wind speed, W) then it follows that $\mathbf{K_{yLc}} = f(\mathbf{U}, \alpha)$.

This model of the dispersion is valid only when all the particles released into the Langmuir cell have sufficient time to reach DD before it breaks up or when $T_D \leq T_*$, where T_* is the typical lifetime of the Langmuir cell. L scales with W (L = (4.8 s) × W, Faller and Woodcock, 1964) and $\mathbf{u} = \mathbf{v} = 0.03$. Values of c are selected so that T_* falls within the range reported by Thorpe (1992) from observations so that $T_* = 10$ min, $c = 3.75$ to $T_* = 30$ min, $c = 11.25$. Contours of $\mathbf{K_{yLc}}$ plotted against $\mathbf{U}^{-1} = W/U$ and α are shown in Fig 3, along with lines of $T_D = T_*$ for three different values of c. The ratio of the lateral dispersion caused by Langmuir circulation to that produced by the tidal current alone is given by $K_{yLc}/K_{yT} = (LW/\beta UH)\mathbf{K_{yLc}}$. A value of 0.4 is taken for L/H, the middle of the range taken from the observations by Graham and Hall (1997), while a value of 0.025 is used for β (Fischer, 1973), possibly an overestimate (see above). Figure 4 shows contours of K_{yLc}/K_{yT} plotted against $\mathbf{U}^{-1}$ and α.

Discussion

The region of validity of Fig 3 ranges from $1 \leq W/U \leq 100$ (e.g. from $W = U = 1$ ms^{-1}, or $\mathbf{U} = 1$, to $W = 10$ ms^{-1}, $U = 0.1$ ms^{-1}, $\mathbf{U} = 0.01$). When the wind is very strong relative to the tidal current, $\mathbf{U}^{-1} \gg 1$, the highest lateral diffusivities are when the wind and current are close to perpendicular. However, when the ratio of wind to tide is close to unity, the maximum values for the lateral diffusivity are when the wind is at about 30° to the current. The non-dimensional values for the lateral diffusivity for $\mathbf{U}^{-1} = 20$ (e.g. $W = 10$ ms^{-1}, $U = 0.5$ ms^{-1}) of between 0.5 and 1.5, and assuming $L = 20$ m, give values of between 0.1 and 0.3 m^{2}s^{-1}, close to those reported in previous studies, though here the diffusivity is measured relative to the tidal current. The asymmetric distribution of $\mathbf{K_{yLc}}$ about $\alpha = 90°$ is caused by the differences in the final distributions of the particles in the windrow. For $\alpha < 90°$, the particles released into the first half of the cell (between A and B) will move towards the convergence line, DD, downwind of the particles released in the second half of the cell (between B and C), while for values of $\alpha > 90°$, the particles released in the first half of the cell will converge onto DD upwind of those released into the second half. This leads to a comparatively smaller final distribution of particles along DD when $\alpha > 90°$ though in the same amount of time, giving the significantly lower values for the lateral diffusivity. Dispersion for α and $-\alpha$ is identical.

Figure 4 shows the importance of Langmuir circulation in the lateral dispersion of buoyant material relative to that caused by a tidal current alone. When $\mathbf{U}^{-1} > 40$ (e.g. $W = 10$ ms^{-1} and $U = 0.25$ ms^{-1}), Langmuir circulation plays a more than equal role in the lateral dispersion of buoyant material. As $\mathbf{U}^{-1}$ approaches and passes a value of 10^2 ($W = 10$ ms^{-1}, $U = 0.1$ ms^{-1}) and at angles between the wind and current greater than 30°, the effects of Langmuir circulation become increasingly

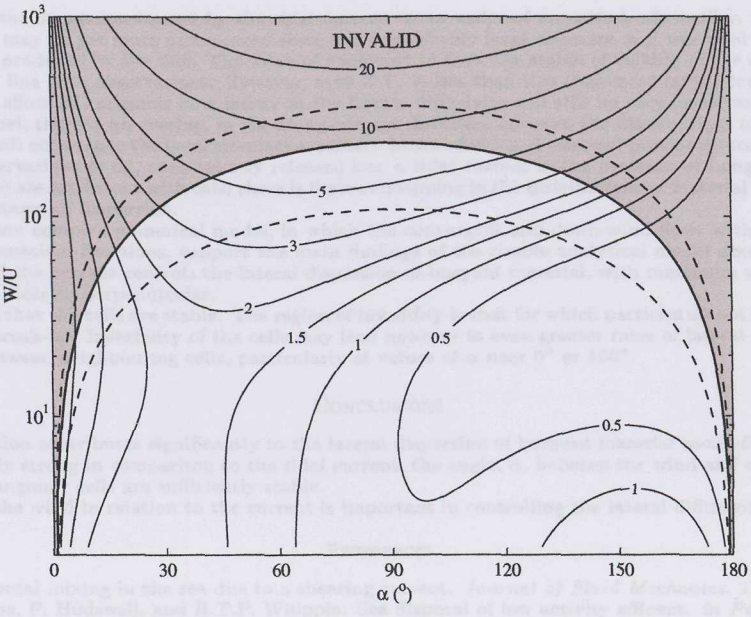

Figure 3 Contours of $\mathbf{K_{yLc}}(\times 10^{-3})$ plotted against $\mathbf{U}^{-1} = W/U$ and α. The thick solid line and the two dashed lines indicate the maximum values of W/U for which the model is valid ($T_D = T_*$). The value of $c = 7.5$ ($T_* = 20$ min) has been used for the solid line, which gives the lower bound to the invalid shaded region, while the lower and upper dashed lines use values of $c = 3.75$ and $c = 11.25$ respectively, to provide a measure of uncertainty.

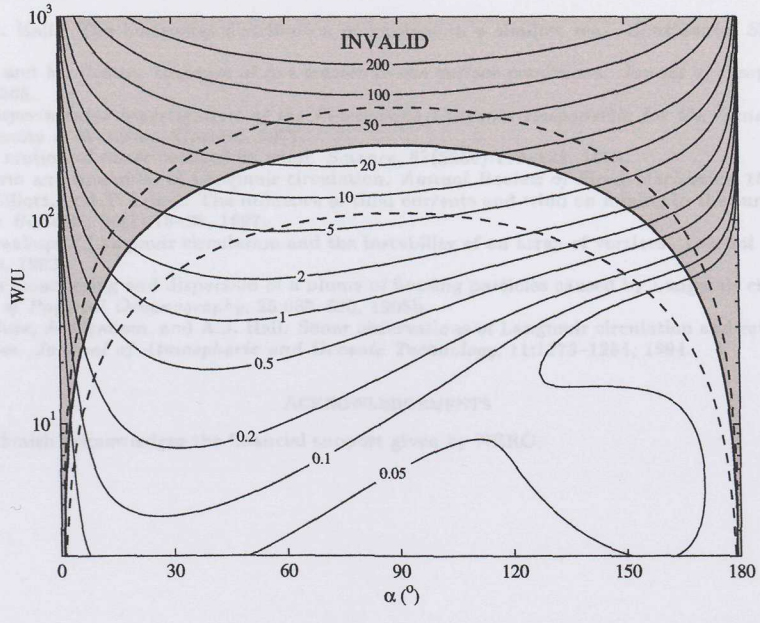

Figure 4 Contours of K_{yLc}/K_{yT} plotted against $\mathbf{U}^{-1} = W/U$ and α. The thick solid line and the two dashed lines are as for Fig 3.

dominant, exceeding the dispersion caused by the tidal current by an order of magnitude. In reality, the dominance of the Langmuir circulation may be yet more pronounced since a conservatively large estimate of β was used in the calculation for the lateral dispersion produced by the tide. The value of c selected to limit the region of validity of the model gives a realistic value for T_* and is in line with observations. However, even if T_* is less than this (indicated by the lower of the two dashed lines and below), the effect of Langmuir circulation on the lateral diffusivity will still be very important.

In this simple model, there is no overlap, in the along-current direction, between the distributions of particles in adjacent windrows. Overlaps will occur once the local circulation pattern breaks down and material previously trapped in the windrows is redistributed. Observations of oil, continuously released into a tidal current in the presence of Langmuir circulation (e.g. Fig. 4, Thorpe, 1995b) are consistent with this; there is little overlapping in the distributions of material in adjacent windrows, at least in the early stages of dispersion.

Results from a more complex numerical model, in which the convergent and down-wind flows within the Langmuir cells are represented by sinusoidal functions, support the main findings of the simple analytical model described here; the angle between the wind and the current controls the lateral dispersion of buoyant material, with maximum values found when the wind and current are close to perpendicular.

It is assumed here that the cells are stable. The region of invalidity is that for which particles do not reach the convergence line before the cells break-up. Instability of the cells may lead however to even greater rates of lateral dispersion as buoyant material is passed between neighbouring cells, particularly at values of α near 0^o or 180^o.

Conclusions

Langmuir circulation contributes significantly to the lateral dispersion of buoyant material soon after it is released when the wind is sufficiently strong in comparison to the tidal current, the angle, α, between the wind and current is between 30^o and 120^o, and the Langmuir cells are sufficiently stable.

The direction of the wind in relation to the current is important in controlling the lateral diffusivity.

References

K.F. Bowden. Horizontal mixing in the sea due to a shearing current. *Journal of Fluid Mechanics*, 21(2):83–95, 1965.

P. Bowles, R.H. Burns, F. Hudswell, and R.T.P. Whipple. Sea disposal of low activity effluent. *in Peaceful uses of atomic energy, UN Geneva. Proc. 2nd Int. Conf*, 18:376–389, 1958.

G.T. Csanady. Turbulent diffusion and beach deposition of floating pollutants. *Advances in Geophysics*, 18A:371–381, 1973.

A.J. Faller and S.J. Auer. The roles of Langmuir circulations in the dispersion of surface tracers. *Journal of Physical Oceanography*, 18:1108–1123, 1988.

A.J. Faller and A.H. Woodcock. The spacing of windrows of Sargassum. *Journal of Marine Research*, 22(1):22–29, 1964.

N.N. Filatov, S.V. Rjanzhin, and I.V. Zaycev. Investigation of turbulence and Langmuir circulation in Lake Ladoga. *Journal of Great Lakes Research*, 7(1):1–6, 1981.

H.B. Fischer. Longitudinal dispersion and turbulent mixing in open-channel flow. *Annual Review of Fluid Mechanics*, 5: 59–78, 1973.

A. Graham and A.J. Hall. The horizontal distribution of bubbles in a shallow sea. *Continental Shelf Research*, 17(9): 1051–1082, 1997.

B. Katz, R. Gerard, and M. Costin. Reponse of dye tracers to sea surface conditions. *Jounal of Geophysical Research*, 70 (22):5505–5513, 1965.

B.C. Kenney. *An Experimental Investigation of the Fluctuating Currents Responsible for the Generation of Windrows.* PhD thesis, University of Waterloo, Ontario, 1977.

I Langmuir. Surface motion of water induced by wind. *Science*, 87(2250):119–123, 1938.

S. Leibovich. The form and dynamics of Langmuir circulation. *Annual Review of Fluid Mechanics*, 15:391–427, 1983.

R.A. Morales, A.J. Elliott, and T. Lunel. The influence of tidal currents and wind on mixing in the surface layers of the sea. *Marine Pollution Bulletin*, 34(1):15–25, 1997.

S.A. Thorpe. The breakup of Langmuir circulation and the instability of an array of vortices. *Journal of Physical Oceanography*, 22:350–360, 1992.

S.A. Thorpe. On the meandering and dispersion of a plume of floating particles caused by Langmuir circulation and a mean current. *Journal of Physical Oceanography*, 25:685–690, 1995b.

S.A. Thorpe, M.S. Cure, A. Graham, and A.J. Hall. Sonar observations of Langmuir circulation and estimation of dispersion of floating particles. *Journal of Atmospheric and Oceanic Technology*, 11:1273–1294, 1994.

Acknowledgements

W.A.M. Nimmo Smith acknowledges the financial support given by NERC.

Appendix C

"Surface effects of bottom-generated turbulence in a shallow tidal sea"

Surface effects of bottom-generated turbulence in a shallow tidal sea

W.A.M.Nimmo Smith, S.A.Thorpe and A.Graham
School of Ocean and Earth Science, Southampton Oceanography Centre,
European Way, Southampton SO14 3ZH, UK.

Nature, **400**, 251-254 (15 July 1999).

Turbulence in shelf seas strongly affects the spread of pollution (e.g. oil spills[1]), as well as the distribution of sediment[2] and phytoplankton blooms[3]. Turbulence is known to be generated intermittently close to the seabed[4] but little is known of its evolution through the water column, or to what extent it affects the surface. Here we present observations of the surface effects of bottom-generated turbulence in a tidally-influenced and well-mixed region of the North Sea, as derived from acoustic and visual images. Although the sea bed in the area is flat, we find that at any one time 20-30% of the water surface is affected by boils – circular regions of local upwelling – of diameter 0.9±0.2 times the water depth. The signature of individual boils persists for at least 7 minutes and, in accordance with laboratory[5,6] and numerical[7] studies, shows the appearance of eddies. The boils contribute to the replacement of surface waters from depth in unstratified waters, and may therefore enhance the fluxes of gases between atmosphere and ocean.

There are no reported observations of the surface signature of boils in well mixed, open sea. It is, however, clear from dynamical measurements made using current meters that tidal flows generate turbulence through the action of shear stress at the sea bed in much the same manner as in laboratory channels[4,8]. Fluid is intermittently ejected away from the bottom in turbulent bursts that may reach vertical speeds of 25% of the forcing current[4]. Numerical[7] and laboratory[5,6] studies show that the upward moving water produces a boil as it impinges on the water surface.

Upward-pointing side-scan sonar has been used to observe a wide variety of processes in the upper ocean[9–13]. In experiments designed to study the processes leading to dispersion of an oil plume in the tidally well mixed – and consequently unstratified[14] – southern North Sea, a two-beam side-scan sonar system was mounted on a frame set on the seabed at a depth of 45 m. The sonars operate at 80 kHz and 90 kHz, are set at 90° apart in the horizontal, and produce vertical fan-like beams with axes aligned upwards, 20° from the horizontal[15]. The site is 56 km from the shore and the local sea bed is flat, with no sand banks or other notable bed forms. The principal acoustic scatterers are bubbles, of typical diameter 20-200 μm, produced in clouds by wind waves as they break[16]. The clouds are detectable to ranges of ~150 m along the sea surface from the sonar, bubbles accumulating in regions of surface convergence and downwelling[17,18]. Oil reduces wave breaking and acoustic scatter from the sea surface[12]. Acoustic observations were made, however, at least 0.5 km from the oil plume, and in a variety of wind speeds from near calm to 14 m s^{-1} and in tidal currents reaching 1 m s^{-1}.

In low tidal flows and winds exceeding ~4 m s^{-1}, the dominant features observed in the sonograph images of the sea surface are the well-known[11,13,15,18] linear bands of bubble clouds aligned close to the wind direction in the convergence zones created between neighbouring Langmuir cells. In stronger tidal currents, however, the linear bands were found to be replaced by crescent-shaped features (Fig. 1a). They have a mean diameter of 42±10 m (± implies one standard deviation) or (0.93±0.22)H, where H is the water depth. The crescents are almost semicircular and are advected with the current. The mean number of features with centres passing through unit length of the sonar beam in unit time is N = (9.4±3.3)×10^{-5} m^{-1} s^{-1}. The sonar beam pointing into the current shows the features to be drifting down-current through the beam at speeds of 0.89±0.09 m s^{-1}. Such speeds are greater than that of the tidal current at 33 m depth (0.75±0.02 m s^{-1}) but less than that at 17 m depth (0.98±0.03 m s^{-1}); they are also less than the speeds of isolated bubble clouds (1.29±0.08 m s^{-1}) seen in the sonar image, which are characteristic of the wind drift and tidal current in the upper 1 m of the water column[9,13,16].

Video images of the oil plume and of the surrounding water surface up to 2 km downstream of a fixed, steady source were obtained at 5-min intervals by an overflying aircraft, 1 hr before the sonograph shown in Fig. 1a was obtained. Figure 1b is a composite image of frames grabbed from the video. It shows the plume, which has become filamentary, and, in particular, the appearance of local regions where the oil is abruptly dispersed normal to the direction in which it is being advected (for example, within the dashed box). Oil accumulates in a convergence zone at the upstream edge of these roughly circular regions, and spreads to either side (see also Fig. 2a). The mean diameter of these regions is 47±14 m or (1.04±0.31)H, and they cover a proportion, p ≈ 0.2, of the water surface. Features tracked in the oil plume through a sequence of video images decay or are engulfed in new, but similar, features in a time τ = 410±140 s, a lower bound because of the limited time-span of the images. Figure 1b also shows patches of discoloured water of lighter shading than their surroundings (for example, arrowed 'C'). Their mean diameter is 65±15 m or (1.44±0.33)H, and they cover p ≈ 0.3 of the water surface. The number of such features per unit area is therefore $0.3/[(\pi/4)65^2] = 9.0\times10^{-5}$ m^{-2}. The discolouration appears to result from the presence of particulate matter, probably sediment, originating from – and pointing to – a local source at the seabed. The evolution of these features is also seen in the Compact Airborne Spectrographic Imager (CASI) images of the break-up of an oil patch (Fig. 3).

The acoustic and visually observed features have the characteristics of boils often seen in fast-flowing shallow rivers and narrow channels[19,20]. Boils are produced as upwelling water interacts with, and spreads radially on, the surface[21,22]. They are often visible in low winds because of their effect in steepening short surface gravity waves[20]. In the laboratory[5,6], dye released near the bottom shows that the boils originate in intermittent ejections from the shear-stress-generated turbulent boundary layer overlying the channel bed. They occur when the upward-moving ejected water impinges on the water surface[5,6]. Eddies evolve at the edges, and downstream, of the boils[6]. This is consistent with our observations; about 44% of the sediment patches observed in the video images (covering ~0.5 km^2) are divided in two by filaments, 8.6±2.4 m in width, roughly aligned with the current (Fig. 2b), suggesting that they consist of pairs of counter-rotating eddies producing an upstream flow along the axis of the features and convergence at their upstream edge. The characteristics of the surface eddies observed in the laboratory, such as separation and size, are found to depend on both outer variables (the free-flow speed, U, and water depth, H) and on inner variables (the friction velocity at the bed and the kinematic viscosity, ν). The diameter of the laboratory eddies decreases with increasing Reynolds number, Re = UH/ν, being about 3H at Re = 8.8×10^3, and greater than the size, about H, of eddies marked by sediment in the North Sea. The laboratory Reynolds number is, however, relatively small, ranging from 4.0×10^3 to 8.8×10^3, whereas Re is about 4.5×10^7 in the North Sea. Whilst the relatively smaller size of the sediment patches may be accounted for by the sinking of sediment (probably faster than 5×10^{-3} m s^{-1},

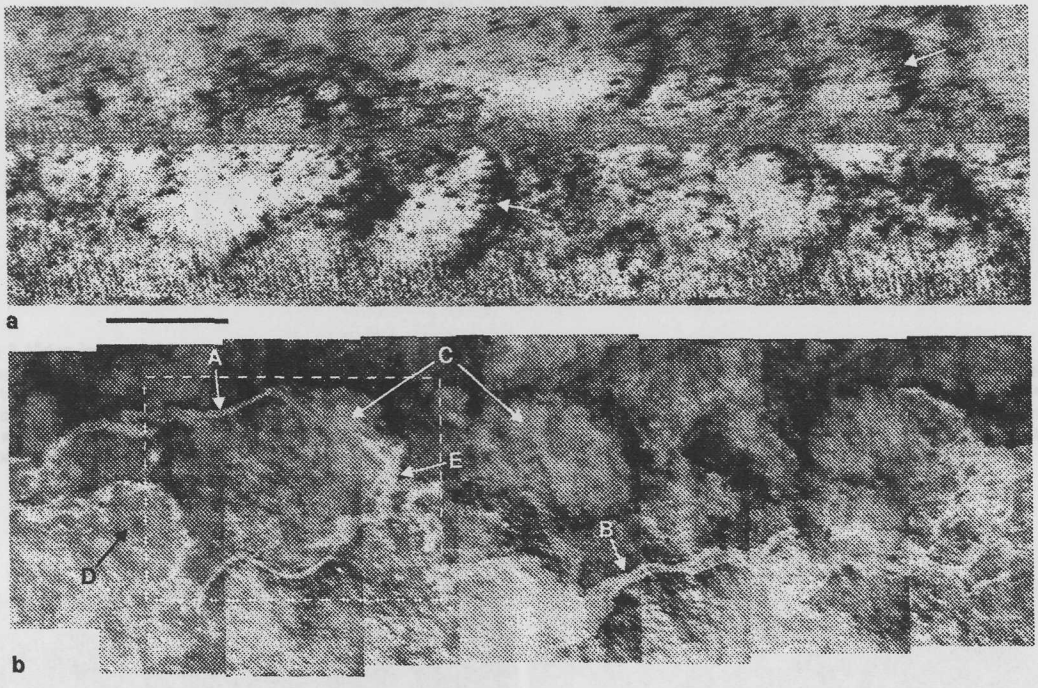

Figure 1 Sonar and video images of boils at the sea surface. The scale is the same in both images (and along both axes) and the tidal current is from right to left; scale bar, 50 m. a, Sonograph from a side-scan sonar beam directed across the tidal current showing crescent-shaped dark patterns (as, for example, shown by arrows) from which sound scattering is intense. The mean flow is 0.98±0.03 m s^{-1} at 17 m depth and 0.75±0.02 m s^{-1} at 33 m depth measured by moored vector-averaging current meters. The tidal current changed by less than 0.1 m s^{-1} hr^{-1}. The wind 10 m above the sea surface is 6.3±0.4 m s^{-1}, headed 43±10° left of the current. The image is derived over a 10-min period, 3.5 h after slack water, and as the features shown are being advected through the sonar beam, the time-scale has been accordingly converted into distance using their advective speed, 0.89 m s^{-1}, as measured by the sonar directed into the current. The band ~65 m from the lower edge results from electrical interference. The faint pattern of near-vertical bands at the lower edge results from reflections from surface waves, of period 3.4 s. b, Composite image from video of the oil plume being advected from right to left. Oil appears white or nearly white; this location, ~1.6 km from the source of the plume, the oil has a filamentary structure (for example, as shown at 'A' and 'B'). Sun-glint is affecting the image along the lower edge, and bright speckles in the centre are caused by sunlight reflecting from surface waves. Lighter blobs show patches of particulate material surrounded by darker regions of clearer water (for example, at positions 'C'). Feature 'D' and the development of the plume within the dashed box are discussed in Fig. 2 legend; oil at 'E' has dispersed laterally around a boil (that is, normal to the mean direction of plume advection).

the settling speed of particulates in the region[2]), the observation that the laboratory scaling depends on inner variables suggests that the differences in scale may be simply a consequence of the difference in Re.

The boils travel at a velocity different from the combined tidal and wind-drift surface current. As shown by the sonograph images of features found with different relative orientations between wind and tidal current (Fig. 4), in ~90% of cases the acoustic scattering is greatest on the side from which the relative wind-drift comes. The boils are therefore visible in the sonar images because the downwelling, or downdrafts[22], at their upwind boundary results in the local accumulation of bubbles[17,18] and wave steepening[20] or even breaking with bubble production, these effects enhancing the scattering of sound there. The surface expression of the boils lags the increasing tidal flow by 100-150 min, consistent with other sonar data[15], observations of suspended sediment concentration[2], and measurements and models of the kinetic energy of developing turbulence[23,24]. In consequence, boils are only observed at the surface for ~70% of the tidal cycle.

Figures 1b, 2a and 3 demonstrate the dispersive effects of the boils on floating material. Neglecting wind, the horizontal dispersion coefficient normal to a steady tidal current over a smooth bottom is $K_{yT} = \beta UH$, where β is a constant[25]. A rough estimate for β can be found from the images. Boils produce a lateral spread of floating particles over scales of order H at times corresponding to those separating the arrival of boils at a given position following the flow. If f is the number of boils produced per unit area per unit time, and τ is their average 'lifetime', then the number of boils reaching the surface per unit area is $f\tau$. If $(1-\epsilon)$ is the fraction of area in which boils overlap and they are advected at speed U, the number of separate boils with centres passing a unit line normal to the flow in unit time is $N = f\epsilon\tau U$. If A is the area of a single boil then $p = f\tau A\epsilon = AN/U = 0.14\pm0.07$ from sonar data (compared to observed $p \approx 0.2$). The surface area fraction covered per unit time is $fA\epsilon$, and the average time for an area to be covered is $T = (fA\epsilon)^{-1}$, the mean time between boils affecting a given area moving with the mean flow. The dispersion coefficient is $\sim H^2/T$, or $ANH^2/\tau U$, so that β $(=ANH/\tau U^2)$ ranges from

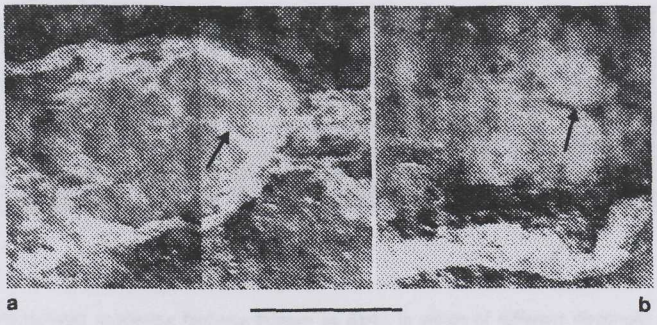

Figure 2 Video images showing details of boils. The tidal current and scales are as for Fig. 1. a, The break-up of the oil plume. This is the region within the dashed box at the left of Fig. 1b, but 5 min earlier: abrupt spreading of oil normal to the direction of its advection is evident about a roughly circular sediment patch. By the time of Fig. 1b, the plume at the lower edge of the patch has been distorted by the growth of a new boil 'D'. b, A sediment patch lying outside the oil plume (part of which is visible as a white band running across the figure at the bottom). The image shows a characteristic feature, a filament (arrowed), connecting to the upstream side. A similar feature is arrowed in the oil pattern in a.

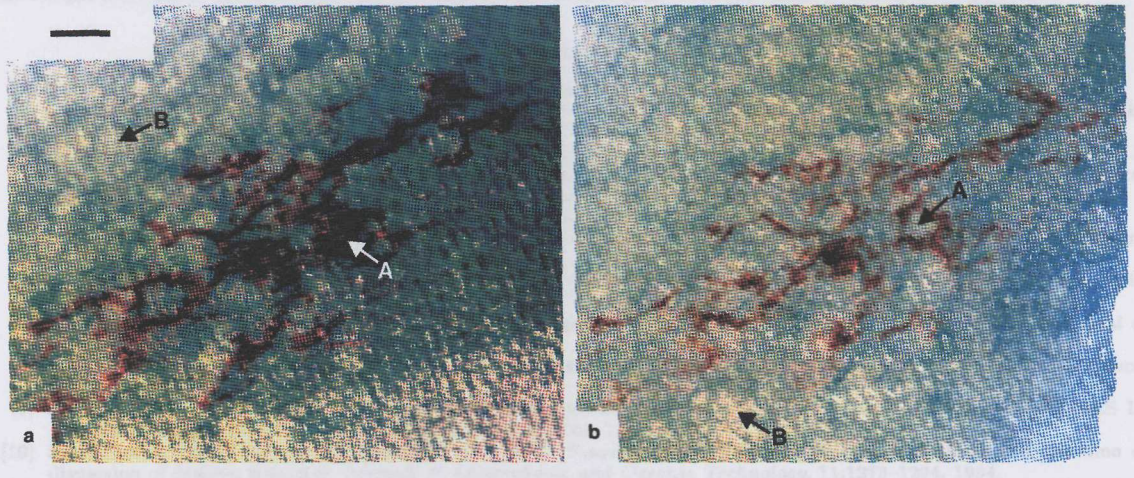

Figure 3 CASI false colour images of an oil patch (in red). The two images are of the same area of sea surface; a was taken 5 min before b. Scale bar, 100 m in both images. The oil has dispersed from a patch in the southern North Sea over a period of 4 tides (2 days) in an area of uniform depth, 45 m. The colour scale is different between the images, and a has been affected by cloud shadow. Oil thicker than 250 μm is imaged as red to black, while yellow and green result from ambient seawater and oil thinner than 5 μm. A roughly circular pale blob, of diameter 50 m, is formed within feature 'A' in the oil in the time between the two images. The yellow blobs (for example, at 'B') are clouds of particulates (see also Fig. 1b ('C') and 2b). North is to the top. The wind speed 10 above the sea is 6.3 m s^{-1} from 340°, and the current at 5 m depth is 0.99 m s^{-1} heading to 189°.

6.4×10^{-3} to 3.9×10^{-2}, using the sonar data and the probable underestimate of τ based on the oil plume. This spans the values, $\beta = (1.0\pm0.4)\times10^{-2}$, found in smooth bottomed laboratory channels[26], though the dependence on Re is uncertain.

The images capture the generation of tidal boils and eddies over a level sea bed, showing they are likely to be of common occurrence in tidal shelf-seas. They also provide insight into the vertical transport of water, sediment and algae on the shelf, at the larger scales that develop following ejections in turbulent bursts from close to the sea bed. The boils impose a patchy structure in, for example, the colour of the water surface (see Figs 1b, 2 and 3), which may bias the measured average values of sea-surface parameters detected by satellite or other 'remote' sensors. The images illustrate how boils disperse oil patches or plumes. Turbulence generated by the shear stress of tidal flow on the sea bed is evidently an important process of short-term dispersion in tidally mixed shelf seas, at least in wind speeds less than about 15U (ref.[27]), at scales smaller than the Rossby radius (when rotation becomes significant) and until bathymetry becomes important[28]; in stronger winds dispersion resulting from Langmuir circulation[10] may dominate. The appearance of the circles in the oil films (Fig. 3) demonstrates that boils help to replenish surface waters, a process important in gas exchange[16,29]. Such boils will be absent at the surface

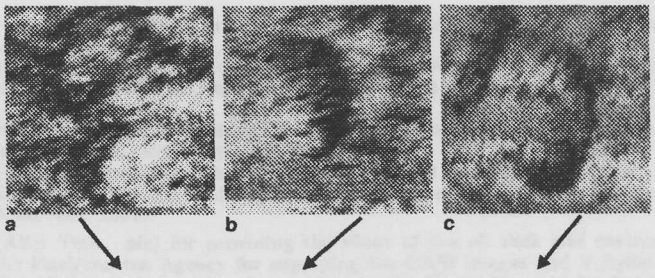

Figure 4 Sonograph images of strongly scattering features (shown as dark) in winds of different directions. The features are represented using the same frozen-field technique described in Fig. 1 legend. In each image, the tidal current is from right to left and the wind direction is shown by an arrow. Each image shows an area 60 m square. The mean current and 10-m wind speed are, respectively, a, 0.60 m s^{-1} (at 19 m depth), 3.0 m s^{-1}; b, 0.98 m s^{-1} (at 17 m depth), 6.3 m s^{-1}; c, 0.80 m s^{-1} (at 15 m depth), 7.1 m s^{-1}.

of density-stratified seas, where the thermocline separates the surface and the deep water, preventing bursts and ejections generated in the benthic boundary layer from reaching the surface. The intensity of near-surface turbulence and the rate of air-sea gas exchange in deep stratified oceanic waters may in consequence be lower than in well-mixed tidal seas.

References

[1] S.P. Murray. Turbulent diffusion of oil in the ocean. *Limnology and Oceanography*, 17:651–660, 1972.

[2] C.F. Jago and S.E. Jones. Observation and modelling of the dynamics of benthic fluff resuspended from a sandy bed in the southern North Sea. *Continental Shelf Research*, 18:1255–1282, 1998.

[3] P.B. Tett, I.R. Joint, D.A. Purdie, M. Baars, S. Oosterhuis, G. Daneri, F. Hannah, D.K. Mills, D. Plummer, A.J. Pomroy, A.W. Walne, and H.J. Witte. Biological consequences of tidal stirring gradients in the North Sea. *Philisophical Transactions of the Royal Society of London, A*, 343:493–508, 1993.

[4] A.D. Heathershaw. "Bursting" phenomena in the sea. *Nature*, 248:394–395, 1974.

[5] S. Komori, Y. Murakami, and H. Ueda. The relationship between surface-renewal and bursting motions in an open-channel flow. *Journal of Fluid Mechanics*, 203:103–123, 1989.

[6] S. Kumar, R. Gupta, and S. Banerjee. An experimental investigation of the characteristics of free-surface turbulence in channel flow. *Physics of Fluids*, 10(2):437–456, 1998.

[7] W. Tsai. A numerical study of the evolution and strucure of a turbulent shear layer under a free surface. *Journal of Fluid Mechanics*, 354:239–276, 1998.

[8] K. Kawanisi and S. Yokosi. Mean and turbulence characteristics in a tidal river. *Estuarine, Coastal and Shelf Science*, 38:447–469, 1994.

[9] S.A. Thorpe, M.J. Ulloa, D. Baldwin, and A.J. Hall. An autonomously recording inverted echo sounder: ARIES II. *Journal of Atmospheric and Oceanic Technology*, 15:1246–1360, 1998.

[10] S.A. Thorpe, M.S. Cure, A. Graham, and A.J. Hall. Sonar observations of Langmuir circulation and estimation of dispersion of floating particles. *Journal of Atmospheric and Oceanic Technology*, 11:1273–1294, 1994.

[11] D. Farmer and M. Li. Patterns of bubble clouds organized by Langmuir circulation. *Journal of Physical Oceanography*, 25:1426–1440, 1995.

[12] M.B. Belloul and S.A. Thorpe. Acoustic observation of oil slicks at sea. *Journal of Geophysical Research*, 97(C4): 5215–5220, 1992.

[13] S.A. Thorpe and A.J. Hall. The characteristics of breaking waves, bubble clouds, and near-surface currents observed using side-scan sonar. *Continental Shelf Research*, 1:353–384, 1983.

[14] J.H. Simpson. The shelf-sea fronts: Implications of their existence and behaviour. *Phil. Trans. R. Soc. Lond. A*, 302: 531–546, 1981.

[15] A. Graham and A.J. Hall. The horizontal distribution of bubbles in a shallow sea. *Continental Shelf Research*, 17(9): 1051–1082, 1997.

[16] S.A. Thorpe. On the clouds of bubbles formed by breaking wind-waves in deep water, and their role in air-sea gas transfer. *Philosophical Transactions of the Royal Society of London, A*, 304:155–210, 1982.

[17] H. Stommel. Trajectories of small bodies sinking slowly through convection cells. *Journal of Marine Research*, 8(1): 24–29, 1949.

[18] S.A. Thorpe. The effect of Langmuir circulation on the distribuion of submerged bubbles caused by breaking wind waves. *Journal of Fluid Mechanics*, 142:151–170, 1984.

[19] R.G. Jackson. Sedimentological and fluid-dynamic implications of the turbulent bursting phenomenon in geophysical flows. *Journal of Fluid Mechanics*, 77(3):531–560, 1976.

[20] M.S. Longuet-Higgins. Surface manifestations of turbulent flow. *Journal of Fluid Mechanics*, 308:15–29, 1996.

[21] J.C.R. Hunt and J.M.R. Graham. Free-stream turbulence near plane boundaries. *Journal of Fluid Mechanics*, 84: 209–235, 1978.

[22] S. Banerjee. Upwellings, downdrafts, and whirlpools: dominant structures in free surface turbulence. *Applied Mechanics Review*, 47(6-2):S166–S172, 1994.

[23] M. Schroder and G. Siedler. Turbulent momentum and salt transport in the mixing zone of the Elbe Estuary. *Estuarine, Coastal and Shelf Science*, 28:615–638, 1989.

[24] H. Baumert and G. Radach. Hysteresis of turbulent kinetic energy in nonrotational tidal flows: a model study. *Journal of Geophysical Research*, 97(C3):3669–3677, 1992.
[25] K.F. Bowden. Horizontal mixing in the sea due to a shearing current. *Journal of Fluid Mechanics*, 21(2):83–95, 1965.
[26] H.B. Fischer. Longitudinal dispersion and turbulent mixing in open-channel flow. *Annual Review of Fluid Mechanics*, 5:59–78, 1973.
[27] W.A.M. Nimmo Smith and S.A. Thorpe. Dispersion of buoyant material by Langmuir circulation and a tidal current. *Marine Pollution Bulletin*, 38:824–829, 1999.
[28] H. Ridderinkhof and J.T.F. Zimmerman. Chaotic stirring in a tidal system. *Science*, 258:1107–1111, 1992.
[29] D.K. Woolf and S.A. Thorpe. Bubbles and the air-sea exchange of gases in near-saturation conditions. *Journal of Marine Research*, 49:435–466, 1991.

We thank T.Lunnel (AEA Tech. plc) for providing the video of the oil slick and environmental data for the CASI images. We also thank the Environment Agency for supplying the CASI images and V.Byfield for calibrating them; and A.Hall for help in collecting the sonar data. The observations in the North Sea were funded by an EEC MAST contract. W.A.M.N.S. is funded by NERC. Correspondence and requests for materials should be addressed to W.A.M.N.S. (e-mail: amns@soc.soton.ac.uk)

Appendix D

Enlarged figures

100m

Z

Y

X

W

100m

Figure D.1: (fold out) Enlargement of Figure 4.6: Side-scan sonar image shown in Figure 4.4b adjusted according to the advection speed and direction of the dark hooked features, $0.89\ m\ s^{-1}$ at 74^o to the left of the sonar beam, as measured by the sonar directed into the current and a current meter at $17\ m$ depth respectively. The upper panel shows the entire $20\ min$ period shown in Figure 4.4b, while the lower panel is an enlarged view of a $6\ min$ sub-section. The tidal current is from right to left, flowing at $0.98 \pm 0.03\ m\ s^{-1}$ at $17\ m$ and $0.75 \pm 0.02\ m\ s^{-1}$ at $33\ m$. The wind at $10\ m$ is $6.3\ m\ s^{-1}$, headed 43^o left of the current. It can be seen that after the correction, the dark hooked features take the form of arcs (for example at 'W'). Reflections from surface waves, of period $3.4\ s$ and height $0.4\ m$, are visible along the lower edge of the images ('X'). Interference from a sonar sampling at twice the frequency produces the horizontal bands, 'Y'. Wind-aligned fine-scale bands are visible within the radius of the arcs (for example at 'Z').

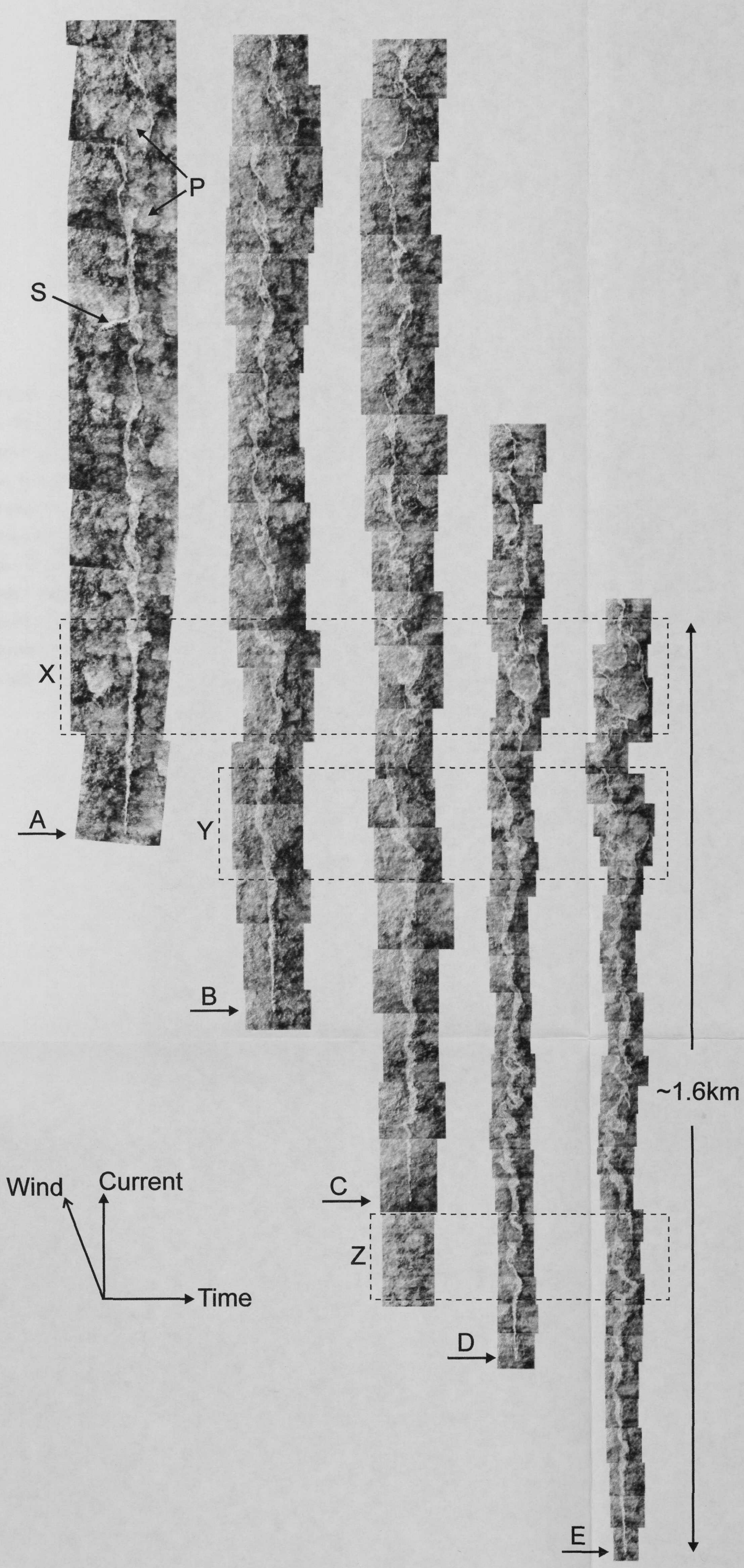
P
S
X
A
Y
B
~1.6km
Wind
Current
Time
C
Z
D
E

Figure D.2: (fold out) Enlargement of Figure 4.8: Sequence of aerial video composites of a diesel plume. Overflights of the plume were at about 5 min intervals. In each, the tidal current is from bottom to top, the wind is about 40^o to the left of the current, and the overall length is about $1.6\ km$. In each case the arrow (labeled 'A' to 'E') marks the location of the moored source of the diesel plume, which is the pale, continuous streak which runs the length of the images. The images have been offset, so as to align similar features in consecutive overflights; the offset between each is about $300\ m$, the distance the plume is advected in the time by the $\sim 1\ m\ s^{-1}$ surface current. Regions labeled 'X', 'Y' and 'Z' are shown in detail in Figures 4.9, 4.10 and 4.11 respectively. 'P' indicates patches of water with high concentrations of particulates, most probably sediment. 'S' is the $12\ m$ sampling boat used, with the aircraft's altitude, to scale the images. Sun glint is affecting the images along their left-hand edges.

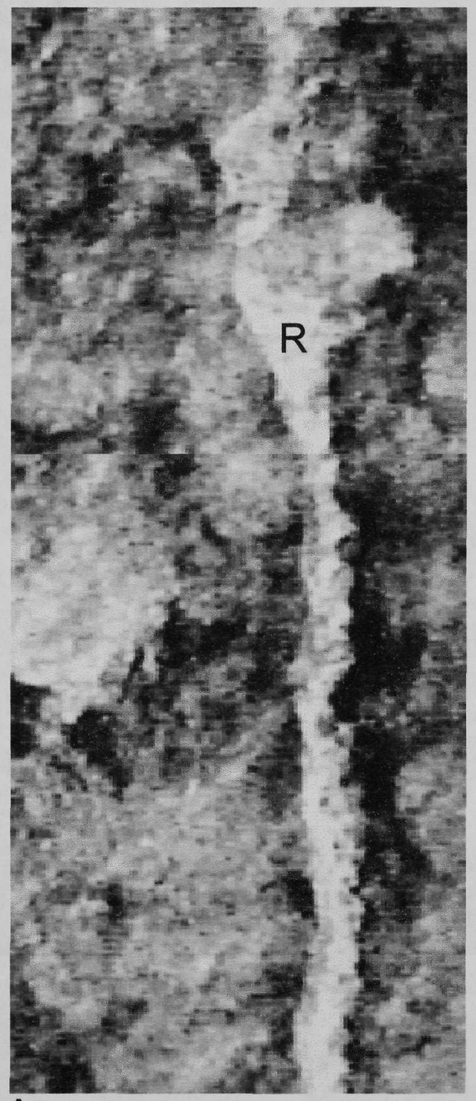

A

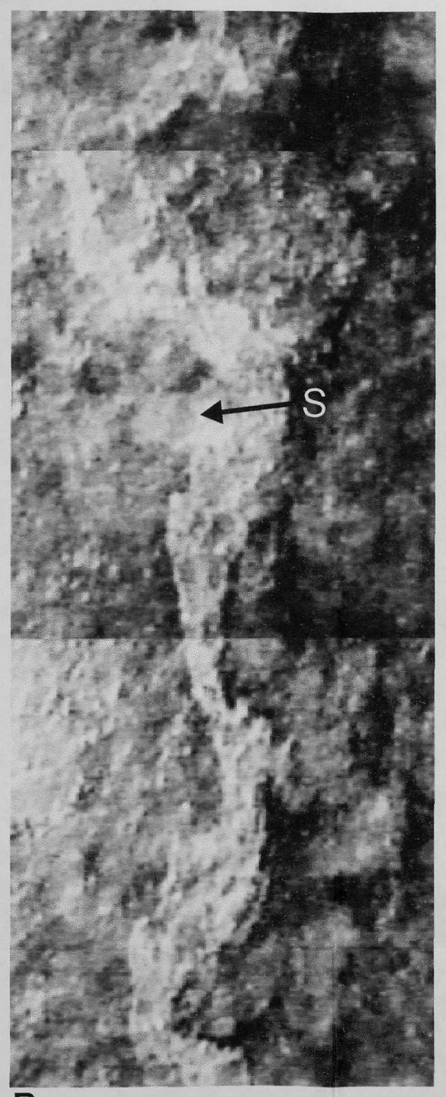

B

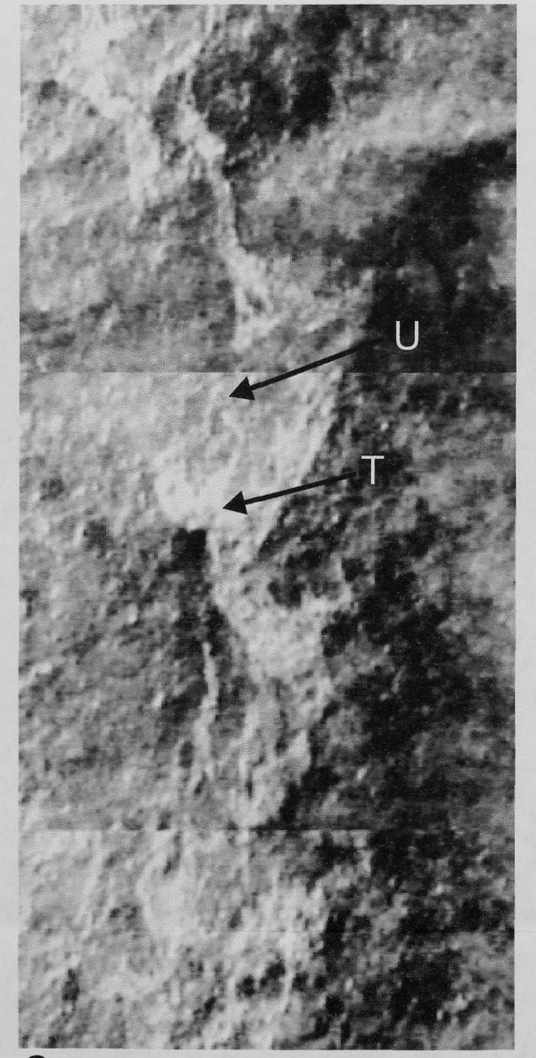

C

50m

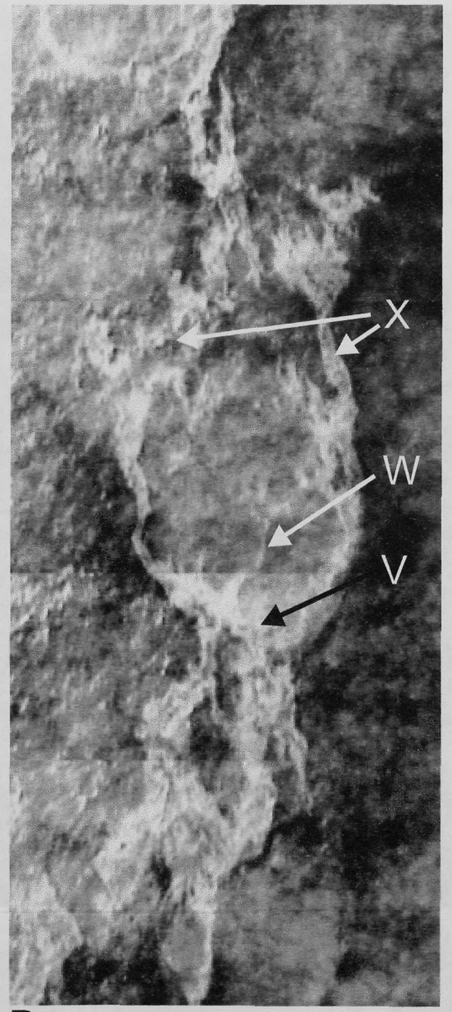

D

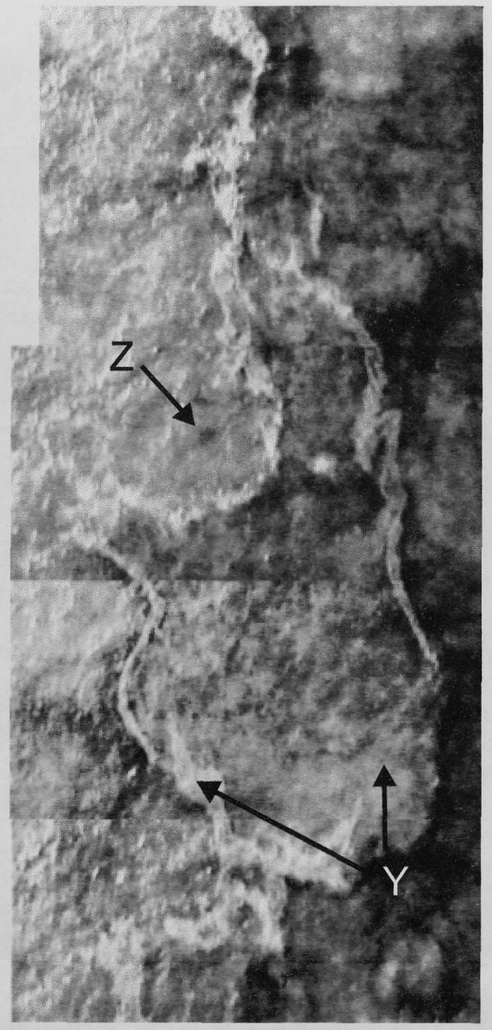

E

Figure D.3: (fold out) Enlargement of Figure 4.9: Aerial video composites showing the evolution of a boil; region labeled as 'X' in Figure 4.8. The mean current is from bottom to top, the wind is 40^o to the left of the current and the images are about $5\ min$ apart. The letters 'A' to 'E' correspond to the lettering in Figure 4.8. The undisturbed plume of diesel oil can be seen as the continuous light streak labeled 'R' in frame 'A', about $150 - 200\ m$ from the moored source. The surrounding water is dark, but interspersed with patches, or 'blobs', with lighter shading - these are regions high in particulate matter. In frame 'B' ($5\ min$ later and $\sim 300\ m$ further downstream) it can be seen that meanders have started to form within the oil plume. A boil, paler than the surrounding water because of its high sediment content, can be seen to be erupting just within the width of the plume at 'S'. A further $5\ min$ later, it can be seen that the boil, 'U', has grown in alongstream length to $\sim 25\ m$. Oil from the plume accumulates around the upstream edge of the boil, 'T', and begins to flow in filaments around the perimeter. Frame 'D' shows the fully developed boil, $\sim 10\ min$ after its initial appearance. A large accumulation of oil can again be seen at the upstream edge, 'V', a fine filament of which can be seen entering the upstream edge of the boil, 'W'. The oil passes in filaments down the sides of the boil, 'X', because of the relative drift between the slow moving boil and the faster moving surface waters. The boil measures $\sim 50\ m$ by $\sim 75\ m$ in the across and along-stream directions respectively. In the final frame, 'E', is can be seen that the boil has become less well defined and is beginning to break-up. The upstream edge becomes fragmented, 'Y', and the sediment within the boil settles out. A new, well-defined boil can be seen erupting within the perimeter of the old at 'Z'.

U

V

W

Y

Z

X

B

C

50 m

D

E

Figure D.4: (fold out) Enlargement of Figure 4.10: Aerial video composites showing the evolution of a second boil; region labeled as 'Y' in Figure 4.8. The mean current is from bottom to top, the wind is 40^o to the left of the current and the images are about $5\ min$ apart. The undisturbed plume is shown in Frame 'B', labeled 'U'. Again, after about $5\ min$, the oil plume begins to meander, and a high sediment content boil, 'V', becomes visible close by. After a further $5\ min$, the oil can be seen to accumulate around the upstream edge of the boil, 'W'. The final frame, 'E', shows the fully developed boil. The accumulation of oil at the upstream edge is visible at 'X'. It can also be seen that the high sediment within the boil is divided into two, 'Y', separated by a thin filament of water with lower sediment concentration, 'Z'.

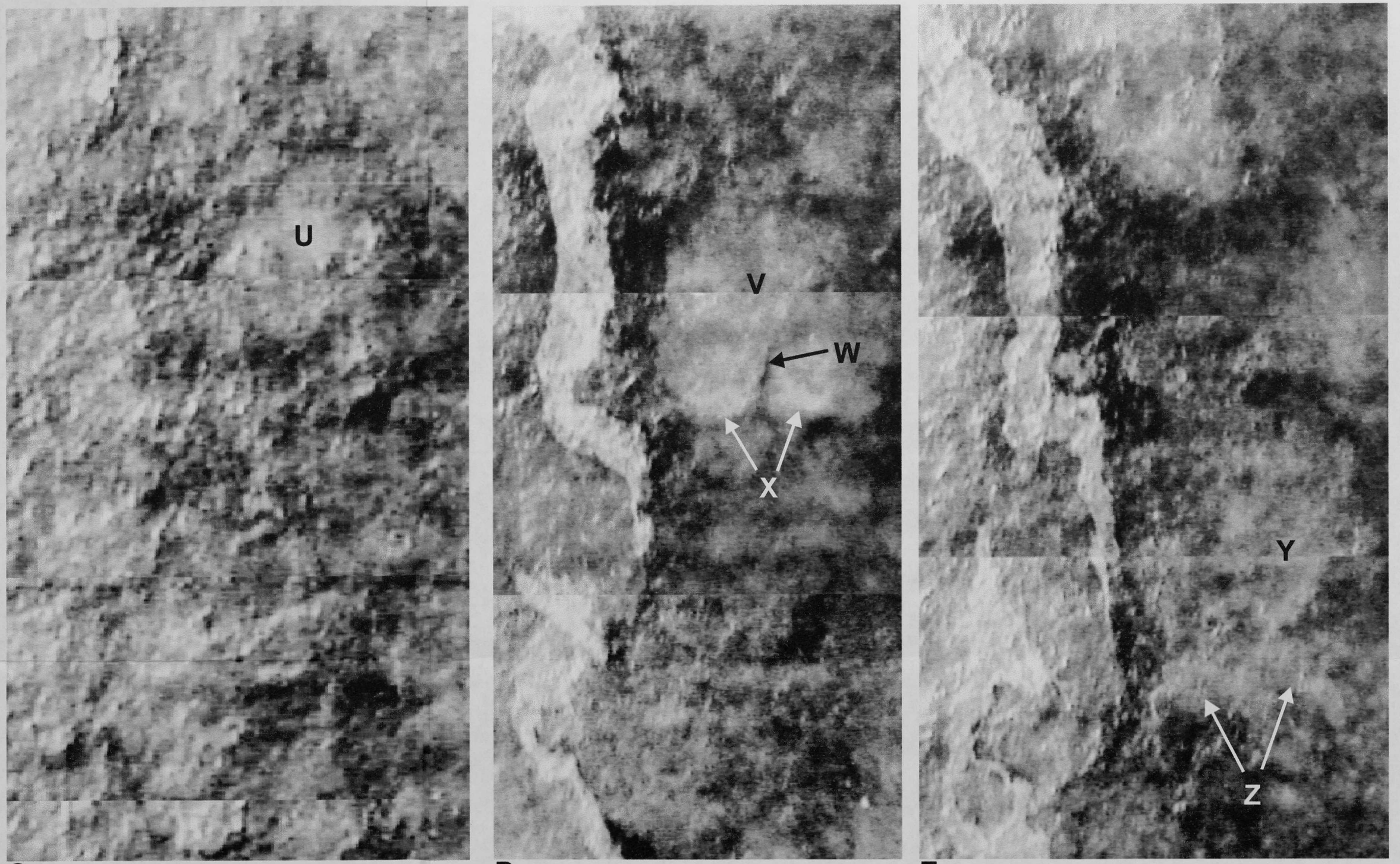
U
V
W
X
Y
Z
C
D
E
50m

Figure D.5: (fold out) Enlargement of Figure 4.11: Aerial video composites showing the evolution of a boil; region labeled as 'Z' in Figure 4.8. The mean current is from bottom to top, the wind is 40^o to the left of the current and the images are about $5\ min$ apart. The first frame, 'C', shows the initial emergence of a sediment patch, 'U', within a region of darker water with lower sediment concentration upstream of the oil release point. $5\ min$ later (Frame 'D') the structure within the sediment patch, 'V', can be seen. The patch is divided into two regions by a filament of clearer water, 'W', with well defined upstream edges, 'X'. After a further $5\ min$, it can be seen in Frame 'E' that the patch, although still in evidence, 'Y', has become diffuse as the coherence is lost and the sediment begins to settle back out. It is still just possible to distinguish the double structure to the upstream edge, 'Z'.

Bibliography

G. Assaf, R. Gerard, and A.L. Gordon. Some mechanisms of oceanic mixing revealed in aerial photographs. *Journal of Geophysical Research*, 76(27):6550–6572, 1971.

R. A. Bagnold. Sand movement by waves: Some small-scale experiments with sand of very low density. *Journal of the Institute of Civil Engineers*, 27:447–469, 1947.

H. Baumert and G. Radach. Hysteresis of turbulent kinetic energy in nonrotational tidal flows: a model study. *Journal of Geophysical Research*, 97(C3):3669–3677, 1992.

K.F. Bowden. Horizontal mixing in the sea due to a shearing current. *Journal of Fluid Mechanics*, 21(2):83–95, 1965.

K.F. Bowden and M.R. Howe. Obsevations of turbulence in a tidal current. *Journal of Fluid Mechanics*, 17:271–284, 1963.

K.F. Bowden, D.P. Krauel, and R.E. Lewis. Some features of turbulent diffusion from a continuous source at sea. *Advances in Geophysics*, 18A:315–329, 1974.

K.F. Bowden and R.E. Lewis. Dispersion in flow from a continuous source at sea. *Water Research*, 7:1705–1722, 1973.

P. Bowles, R.H. Burns, F. Hudswell, and R.T.P. Whipple. Sea disposal of low activity effluent. *in Peaceful uses of atomic energy, UN Geneva. Proc. 2nd Int. Conf*, 18: 376–389, 1958.

K. Colbo and M. Li. Parameterizing particle dispersion in langmuir circulation. *Journal of Geophysical Research*, 104 (C11):26059–26068, 1999.

J.M. Coleman. Brahmaputra River: Channel processes and sedimentation. *Sedimentary Geology*, 3:129–239, 1969.

E.R. Corino and R.S. Brodkey. A visual investigation of the wall region in turbulent flow. *Journal of Fluid Mechanics*, 37:1–30, 1969.

A.D.D. Craik. The generation of Langmuir circulations by an instability mechanism. *Journal of Fluid Mechanics*, 81(2):209–223, 1977.

J. Crawshaw and J. Chambers. *A Concise Course in A-Level Statistics.* Stanley Thornes Ltd, Cheltenham, UK, 1990.

G.T. Csanady. Turbulent diffusion and beach deposition of floating pollutants. *Advances in Geophysics*, 18A:371–381, 1973.

E.A. D'Asaro and G.T. Dairiki. Turbulence intensity measurements in a wind-driven mixed layer. *Journal of Physical Oceanography*, 27(9):2009–2022, 1997.

P. Doron, L. Bertuccioli, J. Katz, and T.R Osborn. Turbulence characteristics and dissipation estimates in the coastal ocean bottom boundary layer from PIV data. *Journal of Physical Oceanography*, in press.

A.J. Elliott. Shear diffusion and the spread of oil in the surface layers of the North Sea. *Deutsche Hydrographische Zeitschrift*, 39:113–137, 1986.

A.J. Elliott, A.G. Barr, and D. Kennan. Diffusion in Irish coastal waters. *Estuarine, Coastal and Shelf Science*, 44:15–23, 1997.

A.J. Elliott and N. Hurford. The influence of wind and wave shear on the spreading of a plume at sea. *Oil and Chemical Pollution*, 5:347–363, 1989.

F. Engelund. Dispersion of floating particles in a uniform channel flow. *Journal of the Hydraulics Division*, 4:11499–1162, 1969.

A.J. Faller and S.J. Auer. The roles of Langmuir circulations in the dispersion of surface tracers. *Journal of Physical Oceanography*, 18:1108–1123, 1988.

A.J. Faller and E.A. Caponi. Laboratory studies of wind-driven Langmuir circulations. *Journal of Geophysical Research*, 83(C7):3617–3633, 1978.

A.J. Faller and A.H. Woodcock. The spacing of windrows of *Sargassum*. *Journal of Marine Research*, 22(1):22–29, 1964.

D. Farmer and M. Li. Patterns of bubble clouds organized by Langmuir circulation. *Journal of Physical Oceanography*, 25:1426–1440, 1995.

N.N. Filatov, S.V. Rjanzhin, and I.V. Zaycev. Investigation of turbulence and Langmuir circulation in Lake Ladoga. *Journal of Great Lakes Research*, 7(1):1–6, 1981.

H.B. Fischer. Longitudinal dispersion and turbulent mixing in open-channel flow. *Annual Review of Fluid Mechanics*, 5:59–78, 1973.

H.B. Fischer, E.J. List, R.C.Y. Koh, J. Imberger, and N.H. Brooks. *Mixing in Inland and Coastal Waters*. Academic Press, New York, 1979.

R.A. Fisher. *Statistical Methods for Research Workers*. Oliver and Boyd, London, 1954.

J.R. French and N.J. Clifford. Characteristics and 'event-structure' of near-bed turbulence in a macrotidal saltmarsh channel. *Estuarine, Coastal and Shelf Science*, 34:49–69, 1992.

C.M. Gordon. Intermittent momentum transport in a geophysical boundary layer. *Nature*, 248:392–394, 1974.

A. Graham and A.J. Hall. The horizontal distribution of bubbles in a shallow sea. *Continental Shelf Research*, 17(9):1051–1082, 1997.

A.J. Grass. Structural features of turbulent flow over smooth and rough boundaries. *Journal of Fluid Mechanics*, 50:233–255, 1971.

A.H. Haidari and C.R. Smith. The generation and regeneration of single hairpin vortices. *Journal of Fluid Mechanics*, 277:135–162, 1994.

A.D. Heathershaw. "Bursting" phenomena in the sea. *Nature*, 248:394–395, 1974.

G.P. Holdaway, P.D. Thorne, D. Flatt, S.E. Jones, and D. Prandle. Comparison between ADCP and transmissometer measurements of suspended sediment concentration. *Continental Shelf Research*, 19:421–441, 1999.

R.G. Jackson. Sedimentological and fluid-dynamic implications of the turbulent bursting phenomenon in geophysical flows. *Journal of Fluid Mechanics*, 77(3):531–560, 1976.

C.F. Jago and S.E. Jones. Observation and modelling of the dynamics of benthic fluff resuspended from a sandy bed in the southern North Sea. *Continental Shelf Research*, 18:1255–1282, 1998.

B. Katz, R. Gerard, and M. Costin. Reponse of dye tracers to sea surface conditions. *Jounal of Geophysical Research*, 70(22):5505–5513, 1965.

K. Kawanisi and S. Yokosi. Mean and turbulence characteristics in a tidal river. *Estuarine, Coastal and Shelf Science*, 38:447–469, 1994.

B.C. Kenney. *An Experimental Investigation of the Fluctuating Currents Responsible for the Generation of Windrows.* PhD thesis, University of Waterloo, Ontario, 1977.

J.C. Klewicki, M.M. Metzger, E. Kelner, and E.M. Thurlow. Viscous sublayer flow visualizations at $R_\theta \cong 1\ 500\ 000$. *Physics of Fluids*, 7:857–863, 1995.

S.J. Kline, W.C. Reynolds, F.A. Schraub, and P.W. Runstadler. The structure of turbulent boundary layers. *Journal of Fluid Mechanics*, 30:741–773, 1967.

S. Komori, Y. Murakami, and H. Ueda. The relationship between surface-renewal and bursting motions in an open-channel flow. *Journal of Fluid Mechanics*, 203: 103–123, 1989.

R.A. Kostaschuk and M.A. Church. Macroturbulence generated by dunes: Fraser River, Canada. *Sedimentary Geology*, 85:25–37, 1993.

S. Kumar, R. Gupta, and S. Banerjee. An experimental investigation of the characteristics of free-surface turbulence in channel flow. *Physics of Fluids*, 10(2):437–456, 1998.

I Langmuir. Surface motion of water induced by wind. *Science*, 87(2250):119–123, 1938.

S. Leibovich. Convective instability of stably stratified water in the ocean. *Journal of Fluid Mechanics*, 82:561–581, 1977.

S. Leibovich. The form and dynamics of Langmuir circulation. *Annual Review of Fluid Mechanics*, 15:391–427, 1983.

L. Li and R. A. Dalrymple. Instabilities of the undertow. *Jounal of Fluid Mechanics*, 369:175–190, 1998.

P. Lombadi, V. De Angelis, and S. Banerjee. Direct numerical simulation of near-interface turbulence in coupled gas-liquid flow. *Physics of Fluids*, 8(6):1643–1665, 1996.

M. S. Longuet-Higgins. Mass transport in water waves. *Philosophical Transactions of the Royal Society of London A*, 245:535–581, 1953.

M.S. Longuet-Higgins. Surface manifestations of turbulent flow. *Journal of Fluid Mechanics*, 308:15–29, 1996.

N. Matsunaga, K. Takehara, and Y. Awaya. Coherent eddies induced by breakers on a sloping bed. In B.L. Edge, editor, *Proceedings 21st Coastal Engineering Conference, Spain, 1988, Volume*, pages 234–245, 1989.

N. Matsunaga, K. Takehara, and Y. Awaya. The offshore vortex train. *Journal of Fluid Mechanics*, 276:113–124, 1994.

G.H. Matthes. Macroturbulence in natural stream flow. *Tranactions of the American Geophysical Union*, 28(2):255–265, 1947.

W.K. Melville, R. Shear, and F. Veron. Laboratory measurements of the generation and evolution of Langmuir circulations. *Journal of Fluid Mechanics*, 364:31–58, 1998.

R.A. Morales, A.J. Elliott, and T. Lunel. The influence of tidal currents and wind on mixing in the surface layers of the sea. *Marine Pollution Bulletin*, 34(1):15–25, 1997.

W.A.M. Nimmo Smith and S.A. Thorpe. Dispersion of buoyant material by Langmuir circulation and a tidal current. *Marine Pollution Bulletin*, 38:824–829, 1999.

W.A.M. Nimmo Smith, S.A. Thorpe, and A. Graham. Surface effects of bottom-generated turbulence in a shallow tidal sea. *Nature*, 400:251–254, 1999.

A. Okubo. Oceanic diffusion diagrams. *Deep-Sea Research*, 18:789–802, 1971.

Y. Pan and S. Banerjee. A numerical study of free-surface turbulence in channel flow. *Physics of Fluids*, 7:1649–1664, 1995.

A.J. Pleuddemann, J.A. Smith, D.M. Farmer, R.A. Weller, W.R. Crawford, R. Pinkel, S. Vagle, and A. Gnanadesikan. Structure and variability of Langmuir circulation during the Surface Waves Processes Program. *Journal of Geophysical Research*, 101(C2):3525–3543, 1996.

R.T Pollard. Observations and theories of Langmuir circulations and their role in near surface mixing. In M. Angel, editor, *A Voyage of Discovery, G. Deacon 70th Anniversary Volume*, pages 235–251. Pergammon Press, 1977.

E.A. Prych. Effects of density differences on lateral mixing in open-channel flows. Technical Report KH-R-21, W.M. Keck Laboratory of Hydraulics and Water Resources, Division of Engineerinf and Applied Science, California Institute ofTechnology, Pasadena, California, 1970.

K.N. Rao, R. Narasima, and M.A. Badri Narayanan. The 'bursting' phenomenon in a turbulent boundary layer. *Journal of Fluid Mechanics*, 48:339–352, 1971.

L.F. Richardson and H. Stommel. Note on eddy diffusion in the sea. *Journal of Meteorology*, 5(5):238–240, 1948.

S.K. Robinson. Coherent motions in the turbulent boundary layer. *Annual Review of Fluid Mechanics*, 23:601–639, 1991.

K.M. Rood and E.J. Hickin. Suspended-sediment concentration and calibre in relation to surface-flow structure in Squamish River estuary, southwestern British Columbia. *Canadian Journal of Earth Science*, 26:2172–2176, 1989.

M. Schroder and G. Siedler. Turbulent momentum and salt transport in the mixing zone of the Elbe Estuary. *Estuarine, Coastal and Shelf Science*, 28:615–638, 1989.

J.H. Simpson. The shelf-sea fronts: Implications of their existence and behaviour. *Philosophical Transactions of the Royal Society of London, A*, 302:531–546, 1981.

E.D. Skyllingstad and D.W. Denbo. An ocean large-eddy simulation of Langmuir circulations and convection in the surface mixed layer. *Journal of Geophysical Research*, 100:8501–8522, 1995.

C.R. Smith. Coherent flow structures in smooth-wall turbulent boundary layers: Facts, mechanisms and speculation. In P.J. Ashworth, S.J. Bennett, J.L. Best, and S.J. McLelland, editors, *Coherent Flow Structures in Open Channels*, pages 1–39. Wiley, 1996.

C.R. Smith and S.P. Metzler. The characteristics of low-speed streaks in the near-wall region of a turbulent boundary layer. *Journal of Fluid Mechanics*, 129:27–54, 1983.

C.R. Smith, J.D.A. Walker, A.H. Haidari, and U. Sobrun. On the dynamics of near-wall turbulence. *Philosophical Transactions of the Royal Society of London, A*, 336: 131–175, 1991.

J. Smith, R. Pinkel, and R.A. Weller. Velocity structure in the mixed layer during MILDEX. *Journal of Physical Oceanography*, 17(4):425–439, 1987.

J.A. Smith. Observed growth of Langmuir circulation. *Journal of Geophysical Research*, 97(C4):5651–5664, 1992.

H. Stommel. Trajectories of small bodies sinking slowly through convection cells. *Journal of Marine Research*, 8(1):24–29, 1949.

S.A. Thorpe. On the clouds of bubbles formed by breaking wind-waves in deep water, and their role in air-sea gas transfer. *Philosophical Transactions of the Royal Society of London, A*, 304:155–210, 1982.

S.A. Thorpe. The effect of Langmuir circulation on the distribuion of submerged bubbles caused by breaking wind waves. *Journal of Fluid Mechanics*, 142:151–170, 1984.

S.A. Thorpe. The breakup of Langmuir circulation and the instability of an array of vortices. *Journal of Physical Oceanography*, 22:350–360, 1992.

S.A. Thorpe. On the meandering and dispersion of a plume of floating particles caused by Langmuir circulation and a mean current. *Journal of Physical Oceanography*, 25:685–690, 1995b.

S.A. Thorpe, M.S. Cure, A. Graham, and A.J. Hall. Sonar observations of Langmuir circulation and estimation of dispersion of floating particles. *Journal of Atmospheric and Oceanic Technology*, 11:1273–1294, 1994.

S.A. Thorpe, A. Graham, and A. Hall. Wave and dispersion studies in shallow water using side-scan sonar. In C. Pattiaratchi, editor, *Mixing in Estuaries and Coastal Seas, Coastal and Estuarine Studies Volume 50*, pages 110–134. 1996.

S.A. Thorpe and A.J. Hall. The characteristics of breaking waves, bubble clouds, and near-surface currents observed using side-scan sonar. *Continental Shelf Research*, 1:353–384, 1983.

S.A. Thorpe and A.J. Hall. Nearshore side-scan sonar studies. *Journal of Atmospheric and Oceanic Technology*, 10:778–783, 1993.

S.A. Thorpe, W.A.M. Nimmo Smith, A.M. Thurnherr, and N.J. Walters. Patterns in foam. *Weather*, 54:327–334, 1999.

S.A. Thorpe, M.J. Ulloa, D. Baldwin, and A.J. Hall. An autonomously recording inverted echo sounder: ARIES II. *Journal of Atmospheric and Oceanic Technology*, 15:1246–1360, 1998.

W. Tsai. Coherent vortical structure in a sheared turbulence beneath the air-sea interface. *Acta Oceanographica Taiwanica*, 35(4):369–374, 1996.

W. Tsai. A numerical study of the evolution and strucure of a turbulent shear layer under a free surface. *Journal of Fluid Mechanics*, 354:239–276, 1998.

R.A. Weller and J.F. Price. Langmuir circulation within the oceanic mixed layer. *Deep-Sea Research*, 35(7):711–747, 1988.

D.K. Woolf and S.A. Thorpe. Bubbles and the air-sea exchange of gases in near-saturation conditions. *Journal of Marine Research*, 49:435–466, 1991.

L. Zedel and D. Farmer. Organized structures in subsurface bubble clouds; Langmuir circulations in the open ocean. *Journal of Geophysical Research*, 96(C5):8889–8900, 1991.

SOUTHAMPTON UNIVERSITY LIBRARY

USER'S DECLARATION

AUTHOR: NIMMO SMITH, WILLIAM A.M. TITLE: DISPERSION OF MATERIAL BY WIND AND TIDE IN SHALLOW SEAS.

DATE: 2000

I undertake not to reproduce this thesis, or any substantial portion of it, or to quote extensively from it without first obtaining the permission, in writing, of the Librarian of the University of Southampton.

To be signed by each user of this thesis

DATE	SIGNATURE	ADDRESS